Globular Cluster Systems in Brightest Cluster Galaxies: Further Definition of the Mass-Metallicity Relation

By

Robert Cockcroft, M.Sci.

Globular Cluster Systems in Brightest Cluster Galaxies: Further Definition of the Mass-Metallicity Relation

By

Robert Cockcroft, M.Sci.

A Thesis

Submitted to the School of Graduate Studies

in Partial Fulfilment of the Requirements

for the Degree

Master of Science

McMaster University

MASTER OF SCIENCE (2008) McMaster University

(Department of Physics and Astronomy) Hamilton, Ontario

TITLE: Globular Cluster Systems in Brightest Cluster Galaxies: Further Definition of the Mass-Metallicity Relation

AUTHOR: Robert Cockcroft, M.Sci.

SUPERVISOR: Prof. William E. Harris

NUMBER OF PAGES: xii, 111

Abstract

Globular clusters (GCs) can be divided into two subpopulations when plotted on a colour-magnitude diagram: one red and metal-rich (MR), and the other blue and metal-poor (MP). For each subpopulation, any correlation between colour and luminosity can then be converted into mass-metallicity relations (MMRs).

Tracing the MMRs for fifteen GC systems (GCSs) - all around Brightest Cluster Galaxies - we see a nonzero trend for the MP subpopulation but not the MR. This trend is characterised by p in the relation $Z=M^p$. We find $p \backsim 0.35$ for the MP GCs, and a relation for the MR GCs that is consistent with zero. When we look at how this trend varies with the host galaxy luminosity, we extend previous studies (e.g., Mieske et al, 2006b) into the bright end of the host galaxy sample.

In addition to previously presented *(B-I)* photometry for eight GCSs obtained with ACS/WFC on the HST, we present seven more GCSs. Four of these are newly analysed from HST data, one is previously presented *(g-i)* photometry obtained with GMOS on Gemini South, and two are the author's newly reduced and analysed *(g-i)* photometry also obtained with GMOS on Gemini South.

Interpretation of these results is important for further understanding the formation and evolution of galaxies within the hierarchical-merging picture, and what process enables the production of two subpopulations.

Acknowledgements

Prof. Bill Harris, thank you very much for all of your efforts to train and educate me not only in the field of globular clusters, but also on astrophysics subjects in general. I have appreciated and learned much from all the very timely feedback you have given me on my endeavours. I also value your support during periods of personal difficulty for me.

Dr. Elizabeth Wehner, your continued help and advice has reassured me throughout my studies - and I am thankful that this didn't change even when you were so far away.

Prof. Christine D. Wilson and Prof. James W. Wadsley, thank you both for being on my defense committee and providing very useful comments and suggestions.

Thank you to all of the physics and astronomy department's office staff: Tina Stewart, Cheryl Johnston, Rosemary McNeice, Liz Penney, Mara Esposto and Daphne Kilgour. Every one of you has helped considerably and made these past two years run very smoothly.

Many, many thanks to my dear family - Mum (Hilary Cockcroft), Dad (Edward Cockcroft), Cal Cockcroft, Andrew Halliday, and Grandma and Grandad (Beatrice and Harold Hartley). I am here and able to do this because of your love and support.

Thank you to all of my friends who I've had the pleasure of walking and exploring the Road with - especially Lindsay and Zach Oaster, Pamela Klaassen and Emily Milner.

And finally, to my partner, Ken Yan. You already express so much faith in me with your words, and even more so with your actions. With much love, thank you.

Table of Contents

List of Figures

List of Tables

Chapter 1

INTRODUCTION: HISTORY AND BACKGROUND

In this chapter, we explore the research already undertaken on the subject of globular cluster systems (GCSs), beginning with a general overview and then looking more at the detailed substructure observed in many GCSs. This work is important to understand more about galaxy formation and evolution. One area that is contributing to developing theories is the study of GCS bimodality - including that of the blue mass-metallicity relation (MMR), which is what this thesis is primarily about. Recent work in this field is explored towards the end of this chapter.

1.1 Overview

Studies of GCSs have long been able to constrain models of galaxy formation and evolution (e.g., Eggen et al. 1962; Searle & Zinn 1978; Fall & Rees 1988; Harris 1991; Ashman & Zepf 1992; Harris & Harris 2001; Harris 2001; Brodie & Strader 2006). Multicolour photometry with *Hubble Space Telescope* (HST) and wide-field ground-based cameras have enabled us to see that the metallicity distribution function (MDF) is important for understanding these

systems. The MDF can be obtained because the broadband colours of old stars correspond closely to the overall heavy-element abundance (see section 4 of the review by Brodie & Strader 2006).

There are many similarities between systems which models must explain. One area where substructure is seen is in metallicity, where we focus our attention. Previously, studies focussed on finding correlations between the metallicity of the globular clusters (GCs) and the metallicity of the host galaxies. It was found that more massive galaxies have more metal-enriched GCs associated with them (van den Bergh, 1975; Brodie & Huchra, 1991). However, the emphasis changed when it was discovered (Zinn, 1985; Ostrov et al., 1993; Zepf & Ashman, 1993; Peng et al., 2006) that the classic, old GCSs can be divided into two subpopulations: one relatively red and the other relatively blue.

Some speculation arose that although the colours of GCSs were seen to be bimodal, this did not necessarily lead to a corresponding bimodality in metallicity (Worthey, 1994; Yoon et al., 2006). However, evidence showing that GCs in massive galaxies are mostly old (Puzia et al., 2005; Strader et al., 2005) implies that the colour bimodality should transform to metallicity bimodality (Strader et al., 2007). More specifically, Puzia et al. (2005) look at data from seven early-type galaxies (Puzia et al., 2004) and find that two-thirds of the GCs have an age >10 Gyr, one-third have an age between 5 and 10 Gyrs, and a very small number have an age <5 Gyrs. Puzia et al. (2005) also find that the metal-rich globular clusters (MR GCs), when compared to the metal-poor globular clusters (MP GCs), appear on average to be younger with a broader distribution in ages. Strader et al. (2007) also use Lick index measurements to

provide clear evidence for two metallicity subpopulations of the 47 GCs they look at in the giant Virgo elliptical galaxy NGC 4472.

In their studies of M87, Kundu & Zepf (2007) reveal bimodal *infrared* colours which they argue can only be explained by a bimodal metallicity distribution. Cantiello & Blakeslee (2007) examine the colour-metallicity relations in detail through numerical experiments. They find that the non-linearity of the colour-metallicity relations will cause a "projection bias", transforming a unimodal metallicity distribution into a more bimodal colour one. This happens across all the different UBVRIJHK band passes and for unimodal metallicity distributions with different peaks and dispersions in their study. It happens least so for the optical-to-near-IR *(V-K)* colours.

Beasley et al. (2008) find, through spectroscopic studies, that the GCS of NGC 5128 is bimodal in metallicity if not multi-modal. The Milky Way GCs show a linear relation between *(B-I)* and metallicity (see figure 7 in Harris et al. 2006). Barmby et al. (2000) find that in their catalog of photometric and spectroscopic data for M31 GCs, both colours in *(V-I)* and metallicities are bimodal.

In contrast to the numerical models by Yoon et al. (2006), Bekki et al. (2008) run both high-resolution cosmological N-body simulations and semi-analytical models. Bekki et al. explore a mass function of dark haloes in a Λ-dominated Cold Dark Matter (ΛCDM) Universe. They identify GCs within the virialized dark matter with a friends-of-friends cluster-finding algorithm, and find that more than 70% of galaxies with $M_B < -19$ have bimodal metallicity, with very clear bimodality in only half (52%), and with galaxies fainter than $M_B \backsim -17$ not showing bimodality due to a lack of red GCs. Bekki et al.

(2008) conclude that if the GC formation rate is not highly efficient in either of formation periods - where MP GCs form in the gas-rich building blocks at high-z and MR GCs form in gas-rich building blocks in galaxies that undergo violent merging - bimodality will not be present. Virtually all GCSs show bimodality, so there appears to be a discrepancy with our understanding of the origin of bimodality (as represented by the simulations and semianalytical models) and what we observe.

We note that solving problems around the age-metallicity degeneracy still need to be resolved - for example, it is not clear over what age range colour tracks primarily metallicity rather than age - but are adequately convinced that the colour bimodality transforms to a metallicity bimodality because the spectroscopic data is less affected than photometry by the age-metallicity degeneracy. We now refer to the two subpopulations as the red, MR GCs and the blue, MP GCs.

Zinn (1985) first examined the Milky Way for subpopulations within its GCS. Zinn found that the MP GCs and MR GCs corresponded to the halo population and disk system, respectively. Ostrov et al. (1993) and Zepf & Ashman (1993) were the first to propose the idea of subpopulations within GCSs of other galaxies when they looked at NGC 1399 and NGCs 4472 and 5128, respectively. Ostrov et al. suggested "multi-modality" for the subpopulations of NGC 1399, but then later changed this conclusion to "bimodal" (Ostrov et al., 1998). Ostrov et al. (1998) also hinted at a dependence on the colour of individual GCs on GC luminosity. They looked at the two GC subpopulations associated with NGC 1399 within a brightness range of $V \approx 21.5$-23.0, and found that at fainter magnitudes the subpopulations were distinct, but

became less so for brighter magnitudes. This relationship, whereby the more massive of the blue, metal-poor GCs become more metal-rich, is now referred to as the blue mass-metallicity relation (blue-MMR) or the "blue tilt".

The division of GCSs into two subpopulations leads to further correlations between the subpopulations and the properties of the host-galaxy. If not equally bimodal in colour, many of the GCSs still have two components that make the overall GC distribution asymmetric (Peng et al., 2006) such that a single Gaussian distribution will not make a sufficient fit to the data. Peng et al. (2006) find that for the brightest and reddest galaxies in their sample up to 60% of the GCs are red whereas for the faintest and bluest galaxies the proportion is closer to $\backsim$15%. Another interesting observation concerns the GCSs of dwarf elliptical galaxies (dEs). These GCSs are seen to have only a blue subpopulation when compared with GCSs of other galaxies - i.e., dE GCSs appear to be unimodal in blue (Lotz et al., 2004). We will return to this point in section 4.

1.2 Substructure

In early-type galaxies, the *mean* GC colour is found to correlate with the host-galaxy luminosity, where GCSs are redder for higher luminosity galaxies (e.g., Geisler & Forte 1990; Bridges et al. 1991; Brodie & Huchra 1991; Ostrov et al. 1993; Larsen et al. 2001; Lotz et al. 2004; Strader et al. 2004; Peng et al. 2006). These galaxies have deeper potential wells and are therefore able to retain more of their metals during starbursts. There is also a relation between the *mean* GC colour and the host-galaxy colour (e.g., Larsen et al. 2001; Peng

et al. 2006). This is expected because of the correlation between luminosity and colour for early-type galaxies (Bower et al., 1992; Stanford et al., 1998).

Other substructure is also seen in the kinematics of the globular clusters. In the review by Romanowsky (2006) the kinematic studies of GCSs of five spiral galaxies and two ellipticals are compared with one another. Romanowsky (2006) notes that the ellipticals' GCSs have lower angular momentum than the spirals, although they suggest more angular momentum may be contained within the halos of the ellipticals. This is supported by simulations (Bekki et al., 2005). Côté et al. (2003) look at the elliptical M49's GCS and the giant elliptical M87. They find that M49 has an overall rotation that is due primarily to the net rotation of the MP GCs ($\Omega R \backsim 100$ - 150 km s^{-1}). The MR GCs tentatively show a weak rotation of $\Omega R \backsim 50$ km s^{-1} beyond $R \gtrsim 0.5\ R_{eff}$. Both subpopulations rotate about M49's minor axis - possibly in the opposite direction to one another, although Côté et al. (2003) caution that because they only have $\backsim 100$ GCs this is of low statistical significance. They also note a distinctive group of 10 MR GCs that they tentatively suggest may be a relic of a merger event. Unlike M49 where the kinematics of the two subpopulations are dissimilar, M87 has a MP GC subpopulation with $\Omega R \backsim 172$ km s^{-1} and a MR GC subpopulation with $\Omega R \backsim 160$ km s^{-1} (Côté et al., 2001, 2003). Peng et al. (2004) find that in NGC 5128, similarly to the planetary nebulae, the MR GCs have significant rotation around a misaligned axis - whereas the MP GCs do not rotate as much.

More recently, Woodley et al. (2007) have found that the MP and MR GCs in NGC 5128 have similar rotations, with $\Omega R \backsim 31 \pm 14$ km s^{-1} and $\Omega R \backsim 47 \pm 15$ km s^{-1}, respectively.

Lee et al. (2008a) find strong rotation in M31 for both MR GCs ($\Omega R \backsim 191^{+37}_{-37}$ km s^{-1}) and MP GCs ($\Omega R \backsim 193^{+44}_{-41}$ km s^{-1}). Earlier results for M31 from Perrett et al. (2002) find the rotation for the red GCs to be $\Omega R \backsim 160 \pm 19$ km s^{-1} and blue to be 131 ± 13 km s^{-1}. Fan et al. (2008) clearly see bimodality in their M31 data - which is both photometric and spectroscopic, although their analysis is completed on their spectroscopic metallicity catalogue. They also see a metallicity gradient for the MP GCs, but not for the MR GCs. The MR GCs, however, are more centrally concentrated than the MP GCs.

As with M87, Hwang et al. (2008) find that the GC subpopulations of M60 have similar rotation amplitudes - although the red GCs are slightly hotter (i.e., have faster rotation) - and similar rotation axes. The rotation of the red GCs, $\Omega R \backsim 171^{+58}_{-46}$ km s^{-1}, and the blue GCs, $\Omega R \backsim 130^{+62}_{-51}$ km s^{-1}, leads to a significant overall rotation, $\Omega R \backsim 141^{+50}_{-38}$ km s^{-1}. The rotation axes are aligned almost perpendicular to the line between M60 and its neighbour, NGC 4647. Having this alignment connected to objects outside the galaxy itself, M60 is again similar to M87. Virgo's brightest gE galaxies form a line, roughly centred on M87; this line is called the "principal axis" of the Virgo Cluster. The GCS of M87 is not only aligned with M87's minor axis, but also with the minor axis of the surrounding galaxies (Côté et al., 2001).

Schuberth et al. (2008) study the GCs around NGC 1399 in the Fornax Cluster of galaxies. They distinguish between intra-cluster GCs, which are GCs far out from the parent galaxy, and "vagrant" GCs, a determination made on radial velocity measurements. However, this was made difficult for Schuberth et al. (2008) because of the high velocity dispersion of NGC 1399's GCs, and as such they only identify one vagrant GC candidate.

In other studies, substructure is seen in the spatial distribution of GCs. Geisler et al. (1996) showed that the colour gradient (or how the relative proportion of red and blue GCs changes with radius) in the GCS of the gE NGC 4472 appears solely because of the subpopulations (which show no colour gradients themselves). Rhode & Zepf (2001) found a gradient within 8', which they attribute to the increasing ratio of blue to red GCs, but do not see a gradient as they increase their area under study out to the edge of the GCS (22' or 110kpc). Studies of another gE (NGC 1399) were completed out to 25' (135kpc) where a galaxy light profile power-law had an index of -1.85 (Dirsch et al., 2003). These studies were extended to 35' by Bassino et al. (2006), who also found galaxy light profile power-law indices, which were -1.61 and -1.90 for the MP GCs and MR GCs, respectively.

Recently, Gómez & Woodley (2007) have looked at the size difference between MR and MP GCs in NGC 5128. Within one effective radius, R_{eff} [1], of the galaxy MP GCs on average appear to be 30% smaller than MR GCs. This confirms many previous studies referenced within Gómez & Woodley (2007). Past 1 R_{eff} out to the extent of their sample at 8 R_{eff} there is no such relation. They propose that the relation in the inner part of the galaxy (i.e., red clusters appear smaller) is just a projection effect because an r_e-R_{GC} (where r_e stands for effective radii of the clusters, and R_{GC} is the galactocentric radius of a GC) relation is seen for the red but not the blue (e.g., as opposed to a situation where both subpopulations get smaller but by different amounts).

[1] The radius within which half of the galaxy bulge's light is emitted is known as the effective radius, R_{eff}.

The possibility of these projection effects was first put forward by Larsen & Brodie (2003).

Zepf (2008) discusses the following puzzling observation. Other systems, e.g., galaxies in a cluster, clusters of galaxies, and molecular clouds, show a strong mass-radius correlation. The progenitors of GCs are thought to be dense cores within giant molecular clouds (GMCs) so that there could be several progenitors within one GMC (see section 1.6.6). Scheepmaker et al. (2007) take information from Larson (1981) and Solomon et al. (1987) and conclude that radius-mass relations are $R_{GMC} \backsim M_{GMC}^{0.57}$ and $R_{GMC} \backsim M_{GMC}^{0.5}$, respectively. Harris & Pudritz (1994) find that the mass distribution, $N \backsim M^{-1.7}$, of GCs in their study of several large elliptical and disk galaxies is identical to the mass distributions of GMCs, cloud cores embedded in GMCs and giant HII regions. It is therefore reasonable to think that if the GMCs show a mass-radius relation, then the GCs would also. However, mass-radius relations for GCs are non-existent or weak. Looking at HST WFPC2 (Wide Field Planetary Camera 2) data for M87, Waters et al. (2006) find a correlation between cluster effective radius and cluster luminosity to be $r_{eff} \backsim L^{0.04}$. Jordán et al. (2005) study 100 early-type galaxies in the ACS Virgo Cluster Survey and find no variation of GC size with luminosity and infer $r_{eff} \backsim M_{GC}^{0}$. The following three studies look at young GCSs. Zepf et al. (1999) look at NGC 3256 with HST WFPC2 data and find $r \backsim L^{0.07}$. Larsen (2004) similarly use WFPC2 data for 18 spiral galaxies. They find a large scatter in their correlations, but conclude that their slope is slightly steeper than but nonetheless consistent with Zepf et al. (1999). Finally, Scheepmaker et al. (2007) observe M51 with HST/ACS (Advanced Camera for Surveys) data and find that for the interarm regions

$r_{eff} \backsim L^{0.15\pm0.02}$ and for the spiral arm regions $r_{eff} \backsim L^{-0.11\pm0.01}$. Although they see these correlations between cluster luminosity and cluster radius, they do not see one for cluster mass. Zepf claims that because the mass-radius relation for both young and old GCs is weak or non-existent this suggests that it is not an evolutionary artifact but rather is connected to the GC formation process. Scheepmaker et al. (2007) further suggest that when GCs emerge from GMCs, the mass-radius relation is somehow erased. However, it still remains a puzzle why GCs do not have a mass-radius relation while their progenitors do.

Lee et al. (2008b) find that for M60 the radial number density profile for the blue is more extended than the red. When looking at number density maps, they also find that the blue component is circular while the red is more elongated, and as such, is more like the stellar halo.

1.3 Galaxy Formation Models

1.3.1 A Broad Overview

After the Big Bang it is believed that structure began to form due to the slight variation in density caused by the permeating quantum fluctuations (e.g., Eisenstein et al. 2005; Cole et al. 2005). This "structure formation model" was predicted over thirty years before its detection (Sachs & Wolfe, 1967). The angular momentum in pre-galactic clouds has some dispersion but it is roughly the same from one cloud to the next (Peebles, 1969; Efstathiou & Jones, 1979; Heavens & Peacock, 1988; Bullock et al., 2001). From there,

the question becomes how do spirals collapse to form their disk (or, similarly, how are ellipticals prevented from doing so)?

After the first generation of stars formed, it is widely believed that subsequent collapse was temporarily halted due to the photodissociating background. Once collapse resumed, Eggen et al. (1962) proposed the "monolithic collapse" in which the largest structures form prior to the smaller ones. GCSs of ellipticals are bluer than their host-galaxy implying that the clusters and their stars formed earlier than the host-galaxy (Harris, 1986; Beasley et al., 2006). Strong rotation of GCSs seen in M87 and M60 is not expected from this collapse (Hwang et al., 2008).

At the opposite extreme Searle & Zinn (1978) suggested that smaller things form first in a "bottom-up" or "hierarchical merger process" - an idea that expands on that of Toomre & Toomre (1972). This appears to be consistent with the cosmological model of ΛCDM which includes hierarchical clustering that still appears to be occurring for clusters and super-clusters (e.g., Peebles 1984; Baugh et al. 2004; De Lucia & Blaizot 2007).

The most recent addition is by Cowie et al. (1996) who suggest a paradigm that is known as "downsizing". This picture assumes that the dark matter follows the hierarchical merger process, whereas luminous matter more resembles the monolithic collapse because with downsizing the "assembly of the upper end of the galaxy luminosity function is occurring from the top down with decreasing redshift" (Cowie et al., 1996).

Merging events are also known to be very important. Seeing a potential merger event so close to home - the Sagittarius Dwarf Elliptical Galaxy merging

with our Galaxy (Ibata et al., 1994) - prompted a renewed interest in this area. More information on this topic is given in the next section.

1.3.2 GC Formation within the ΛCDM Universe

Assuming a cold dark matter (CDM) Universe, Peebles (1984) find that cosmological models lead to two length scales: the longer one to galaxies and the shorter one to GCs, where the latter form within extended dark haloes. Gas clouds of length 1 kpc and total mass of $\backsim 10^8_\odot$, have a $\backsim$ 3 x $10^6_\odot$ component of hydrogen at a temperature of T $\backsim$ 100 K. These hydrogen components are the first resemblances of GCs, and occur at redshifts of $z \backsim 50$. When the 3 x $10^6_\odot$ hydrogen cloud has collapsed to 30 pc (i.e., having shrunk by a factor of $\backsim$ 30 in radius), the centre can form stars, temporarily re-expand the cloud by heating it up, and add more metals back into the gas through supernovae. If the stars and supernovae do not blow the cloud apart, then the process repeats itself until there is no more hydrogen left. This scenario, Peebles claimed, would be able to explain several relations such as that between 1) the GC metallicity and density of halo, 2) GC metallicity and galactocentric distance, and 3) the GC radius with galactocentric distance. The dark matter (DM) halo would be left around the GC - although there was no observational evidence for this at that time (as there also does not appear to be now - see next paragraph). Two further problems raised then that continue to be problems today are that the high rotation expected from the large factors involved in the shrinking of the gas cloud are not seen, and it is not certain how the scattering of metals can occur efficiently enough to explain observations.

Several papers cover simulations concerning GCs and their formation, dark matter (DM) components and possible connections to dwarf spheroidal galaxies and other similar objects (Mashchenko & Sills, 2004, 2005a,b; Mashchenko et al., 2006a,b). Mashchenko & Sills (2004) simulate the violent relaxation of initially identical stellar spheres that result in a range of GCs which match the observed GC radial density profiles which, they argue, suggests that the gas that formed the GCs across the Universe was the same temperature and density. In Mashchenko & Sills (2005a), simulated DM-dominated GCs show features - such as tidal cutoffs, extratidal stars or eccentric outer contours - consistent with interactions of a tidal field from the host galaxy. The simulations indicated that the GC would lose most of its DM. More observations are needed to distinguish amongst these types simulations, but in the second part of this two-paper series (Mashchenko & Sills, 2005b) the "primordial scenarios" of GC formation - which predict GCs form in potentials of DM minihaloes (i.e., like a mini-galaxy) - are consistent with current observations. Saitoh et al. (2006) also perform further simulations and have similar conclusions.

Finally, Mashchenko et al. (2006a) simulate the collapse of previously photoionized mini-galaxies, and suggest a possible connection between these and MP GCs and dwarf spheroidal galaxies. Collapsed core sizes are comparable to the size of GCs ($\backsim$ 5 pc), and if the metallicity increases above a certain value ($\backsim 10^{-3}\ Z_{\odot}$) they believe star formation will switch from producing Population III to Population II stars and may account for the MP GCs that we see today. In their review, Brodie & Strader (2006) argue that the cosmological formation of the MP subpopulation is supported by the material discussed above, but does the formation of the MR subpopulation need to be explained

in a different way? The strongest similarity between the two, they say, is their mass function with indices of $\backsim$-1.8 to -2.0 - although they also note that mass functions can be brought about by various different mechanisms.

1.4 The Origin of Bimodality

The next question asks how bimodality comes about. Ashman & Zepf (1992) suggest major disk-disk mergers where MP GCs come from the progenitor disks and the MR ones form through the merging process. Many young massive stellar clusters are also seen in major-merger remnants (Ashman & Zepf, 1992), lending more support to this scenario. However, there is still a conflict between the predicted and observed relative number of MP and MR GCs. At the end of section 11.1.1 in their review, Brodie & Strader (2006) highlight that the existing problems - also seen throughout the 1990s - for the merger models arise from expecting present-day ellipticals (Es) to have formed from present-day spirals. These problems call for spirals at higher redshift to have higher values of specific frequency, S_N values. Harris (1998) comments that although mergers can explain observations of elliptical galaxies that have low S_N, giant elliptical (gE) and cD [2] galaxies need to be described qualitatively differently because they have higher S_N. Peng et al. (2008) find that values of S_N depend mostly on the blue GCs (when compared across galax-

[2] Historically, the 'c' has stood for supergiants in the spectral classification of star, and 'D' for a galaxy with a diffuse envelope, so that combining them means that a cD galaxy is one that is a supergiant one with a diffuse envelope (Matthews et al., 1964). We also note that cD galaxies are usually found at the centre of a group, and as such are the centrally dominant member.

ies with similar masses), although the proportion of red GCs increases with galaxy luminosity to $M_V \backsim$ -22, at which point it flattens out.

Forbes et al. (1997) propose multi-phase dissipational collapse where the MP GCs form at a very early stage, the process halts, and then it resumes again from richer gas (i.e., the process occurs in an isolated system, unlike the previous scenario). Santos (2003) suggests that cosmic reionization is the mechanism that halts the process. Semi-analytic models, such as Beasley et al. (2002), find it necessary to truncate MP GC formation at a redshift of $z>5$ to produce the observed bimodality. Beasley et al. (2002) also find that their semianalytic models show both the MR and the MP GCs show a weak relation with the host galaxy luminosity - giving us a hint of what was about to come (see section 1.5). Harris (2001) alternatively suggest that the initial gas in the proto-galaxy formed the MP GCs that we see today, but was prevented from forming a corresponding population of MP field stars by the first round of supernovae and the onset of the galactic wind. The gas left over from the MP GC formation became enriched through these supernovae and collapsed to make up not only the MR GCs but also the MR field stars. Harris et al. (1999) also find that two distinct star formation epochs fit their observations of NGC 5128, the nearest gE galaxy. It is interesting to note the halo and bulge field stars do not reflect the bimodality seen in the GCs but rather show a unimodal distribution containing few MP stars (Harris & Harris, 2002). Harris et al. (2006) suggest that this could be due to a much more efficient cluster formation period, or conversely that there was some destruction process which targetted MR GCs.

Côté et al. (1998) have an accretion scenario - consistent with the hierarchical structure formation - where the MR GCs formed in-situ in a massive galaxy, whereas the MP ones were accreted from neighbouring lower-mass galaxies. The high accretion rates might not be plausible to produce the observed bimodality, which itself would just be a statistical accident because the galaxy would have to accrete many *small* galaxies and none at all in a mid-range size.

Accretion rates must be quite high to produce the observed bimodality, and it is not yet known if these high rates are plausible.

Finally, Harris (2003) suggests that the three preceding models are not mutually exclusive. A given galaxy may actually be a combination of all three in a way that is dependent on the amount of gas in the system (see also Harris 2001).

To distinguish among the plethora of GC formation models, Fall & Rees (1988) propose that GCs can be categorized according to which period relative to the formation of their host galaxy that they formed in. GCs which were formed before, during and after the formation of their host galaxy are referred to as primary, secondary and tertiary formation, respectively. The exact point at which a galaxy is said to have formed is quite vague, so the host galaxy and GCs are said to form together if the galaxy is still undergoing proto-galactic collapse. If the galaxy is quiescent, the GCs are said to have formed after the galaxy.

1.5 The Observed Blue Mass-Metallicity Relation

There are two relations which appear similar - but only the second of which we study here in this paper. We outline the first relation in section 1.5.1 to avoid confusion, and then continue with the second, the MMR, in section 1.5.2.

1.5.1 The Mean Colour of GCSs for Many Galaxies

The first relation looks at the *mean colour of the GC subpopulations within one galaxy* which is then plotted against the luminosity of the host galaxy, *for many different galaxies* (see figure 1.1, originally printed as figure 3 in Peng et al. 2006). There is not, unfortunately, a name for this relation in the literature, so for ease of referencing we call it the GC colour-galaxy luminosity relation, or CGL relation. To characterize the CGL relation a slope is estimated for the trend of the blue (and another for red) MP (MR) GCs over galaxy luminosity. The first studies of this CGL relation (e.g., Forbes et al. 1997; Forbes & Forte 2001; Larsen et al. 2001), found that MR GCs correlated with host-galaxy luminosity, but - with the exception of Larsen et al. (2001) - MP GCs did not. Burgarella et al. (2001) constructed a database of MP GCS from 47 galaxies whose range in absolute brightness was about 10 magnitudes. They found the slope between the MP GC mean metallicity and absolute V magnitude was very low and included zero.

Contrary to the above, Strader et al. (2004) and references therein use a Bayesian Markov Chain Monte Carlo method with a variety of data sets from studies with the V and I bands to derive a MP GC colour-galaxy luminosity relation of the form $Z \sim L^{0.15 \pm 0.03}$. Peng et al. (2006) comment that previous

authors who have suggested that a lack or weakness of the blue-CGL relation were not using homogeneous data sets and usually used *V-I* colours. The filters used can affect the strength of the correlation observed (Mieske et al., 2006b). *B-I* colours are more sensitive to the older metallicities, but *V-I* are used because the *HST* Wide-Field Planetary Camera 2 (WFPC2), which was commonly used before the Advanced Camera for Surveys (ACS), was insensitive to the blue. The results of Strader et al. (2004), who are against both the accretion and major merger scenarios but instead support the picture of truncation through ionization, are confirmed in other studies below.

With *(g-z)* colours, Peng et al. (2006) find a correlation between metallicity[3] and host-galaxy luminosity and stellar mass for *both* subpopulations: $Z_{MP} \sim L^{0.16\pm0.04} \sim M_{\star}^{0.17\pm0.04}$ and $Z_{MR} \sim L^{0.26\pm0.03} \sim M_{\star}^{0.33\pm0.03}$. With such similar relations for both subpopulations, the authors argue that the conditions under which both formed could not have been too different. Note that Peng et al. (2006) data has the brightest data at M_B=-22. Peng et al. (2006) also comment that metallicity dispersions of GCSs potentially hint at the degree of mixing within the host galaxy as it formed. A large dispersion could suggest a much greater time span over which formation occured or that it occurred with more spatially isolated pockets within it.

We have been discussing the relation between mean colours of the GC subpopulations and the host galaxy luminosity *at current times* (i.e., at z=0). The relation is characterized by $Z_{GC} \sim L^{\alpha}$ where estimates for α have been 0.15±0.03 (Strader et al., 2004) and 0.16±0.04 (Peng et al., 2006). "Bias-

[3] Although Peng et al. (2006) use [Fe/H] in their CGL relations it is implicit that they actually mean Z, where [Fe/H]=log$Z$.

ing" (Bekki et al., 2006) is the term used to describe the effect where α may have been larger at higher redshifts. Bekki et al. (2007) produce numerical simulations that demonstrate a steeper relationship (α=0.5) at high z results in a value of α at z=0 that matches the recent observations (Strader et al., 2004; Peng et al., 2006). The best results are obtained if the MP GC formation period is truncated at z_{trunc}=10, and also that the mass-to-light ratio at that time is constant. Santos (2003) first demonstrated that this truncation was necessary to explain the high S_N values in cluster ellipticals and other structures. This has been further discussed by Bekki (2005), Bekki & Chiba (2005), Rhode et al. (2005) and Moore et al. (2006). Bekki et al. (2007) argue that the slope characterized by α becomes flatter at more recent times due to hierarchical merging. Although it is observationally and theoretically unclear how the slope could get so steep in the first place, a tentative suggestion is that stripped galactic nuclei may play a small role. They would do this by populating the the most luminous blue GC region to help produce the observed blue CGL relation (see also section 1.6).

1.5.2 MMR for Individual Subpopulations Within One GCS

The second MMR looks at the *individual slope of the blue (and red) GCs within one galaxy* on a colour-magnitude diagram (CMD), which is then converted into a MMR (see figure 1.2, originally printed as figure 20 in Harris et al. 2006).

Looking at the blue subpopulation of GCSs of Brightest Cluster Galaxies (BCGs), Harris et al. (2006) find a significant trend for the blue GCs within one galaxy towards redder colours for increasing GC luminosity. They found this

mass-metallicity relation to scale as $Z \sim M^{0.55}$. No similar relation is found for the red subpopulation. Harris et al. (2006) conclude that these characteristics are consistent with a hierarchical-merging model whereby the lower-mass, blue, metal-poor GCs form in lower-mass protogalactic clouds whereas the higher-mass GCs formed in bigger clouds. These bigger clouds would have had a deeper potential well that could have held onto significantly more pre-enriched material. They suggest that a MMR is not seen for the red subpopulation because these GCs form later. At this stage galaxy-merging events could create various sizes of protoGC clouds which are all under the influence of the potential well of the host BCG, which itself has now fully formed on the large-scale.

Wehner et al. (2008a) look at NGC 3311, which has a very large GCS ($\backsim$ 16,000 GCs). Bimodality is seen, and the corresponding blue MMR is $Z \sim M^{0.6}$. Wehner et al. (2008a) also note that no MMR is found for the red subpopulation, but that it extends far more into the typical region of UCDs (see section 1.6.1).

Mieske et al. (2006b) use a KMM ("Kaye's Mixture Modelling"; Ashman et al. 1994) algorithm to find a colour-magnitude relation for 79 early-type galaxies (-21.7 < M_B < -15.2) with *HST* ACS imaging. They divide these galaxies into four magnitude bins. The co-added GC CMD for the brightest group, which contains M49, M87 and M60, is found to have a blue subpopulation with a colour-magnitude relation of $d(g\text{-}z)/dz$=-0.037±0.004. With piecewise colour-metallicity relations from Peng et al. (2006), this corresponds to a mass-metallicity relation that scales as $Z \sim M^{0.48\pm0.08}$. Like Harris et al. (2006), they find no MMR for the red subpopulation.

Strader et al. (2006) also find a trend for the more luminous blue GCs to be redder in the GCSs of M87 and NGC 4649. The colour-magnitude relations found are $d(g\text{-}z)/dz$=-0.043±0.010 for M87 and $d(g\text{-}z)/dz$=-0.040±0.005 for NGC 4649. With Maraston (2005) models, these correspond to MMR such that $Z \sim M^{0.48}$ for M87 [4] and $Z \sim M^{0.43}$ for NGC 4649. They suggest self-enrichment as a plausible interpretation, and also tentatively suggest these blue GCs may have had dark matter halos which were later stripped away.

Cantiello et al. (2007) find evidence for the blue-MMR while looking at the GCS of NGC 5866. The authors caution that this result is tentative as the sharp separation limits that split the two subpopulations introduce bias into the results as there will naturally be some overlap. They also note that they use a system of only 109 GCs to detect these slopes. The colour-magnitude relation is $d(B\text{-}R)_0/dR$=-0.012±0.009. With their colour-metallicity relation, this corresponds to a MMR that scales as $Z \sim M^{0.11\pm0.09}$. Just as Harris et al. (2006) find that the blue-MMR is most noticeable for the galaxies with the most numerous cluster populations, so Cantiello et al. (2007) agree with this trend when they compare the GC system of NGC 5866 to the results from the Sombrero galaxy GCS (Spitler et al. 2006; see below).

Curiously, Strader et al. (2006) find no blue-MMR in NGC 4472 (M49), a bright elliptical. If this is confirmed, it will provide an intriguing constraint on the formation models for an otherwise "universal" trait. Mieske et al. (2006b) suggest that an environmental effect may be responsible for this non-detection,

[4] Note that the same colour gradients of Mieske et al. (2006b) and Strader et al. (2006) result in slightly different indices because different models were used, and because Strader et al. (2006) are more approximate in their method.

which they confirm, by noting that the galaxy is found in the centre of its own sub-cluster which is $\backsim 4.5^\circ$ away from the Virgo Cluster centre.

DeGraaff et al. (2007) look at colour-magnitude slopes of the red and blue subpopulations of the GCS of NGC 1533. Within errors the slopes are consistent with zero which is unsurprising to DeGraaff et al. (2007) since NGC 1533 is not a bright elliptical nor is it in a group of galaxies. They conclude it would not have been able to undergo the necessary self-enrichment they favour to explain these slopes.

Another point of interest is that it is not just ellipticals that display a blue-MMR as it has also been seen in Sa galaxies, too (e.g., Spitler et al. 2006). Spitler et al. find that for the MP GCs in the Sombrero Galaxy (NGC 4594), the colour-magnitude relation is $d(B\text{-}R)_0/dR$=-0.035±0.005 and the corresponding MMR is $Z \sim M^{0.27}$. There is no evidence for a trend in the MR GCs. Spitler et al. (2006) argue that the blue-MMR is not simply a feature of luminous MP GCs, but seems to extend down to lower GC luminosities as well. They argue that it is therefore not likely to be due to an additional population at the brighter end. It is also interesting to note that while Harris et al. (2006) find the dE,N appear as an extension of the blue side of the GC distribution - most noticeably for NGC 4696 but also in their other seven BCGs to a lesser degree - Wehner & Harris (2007) find that their ultra-compact dwarfs (UCDs; see Section 1.6.1 for further details) are an extension of the red side.

The Milky Way has not shown any indication that it has a blue-MMR but this may be due to the small number of ~150 (Harris, 1997) of GCs within its system. A series of three papers by Parmentier and colleagues (Parmentier et al., 1999, 2000; Parmentier & Gilmore, 2001) find and discuss

a relation that *is* seen among the Galactic Old Halo GCs where, contrary to the previous MMRs, the *least* massive old clusters are the most metal-rich (see section 1.6.6). They do this through a model of self-enrichment. Parmentier & Gilmore explain that within a self-enrichment scenario, the more metal-rich material there is the more mixed up in a larger amount of gas it will be, so you would *not* necessarily expect more massive clusters to be more metal rich. However, the ability of higher mass clusters to be able to retain the metals is also an important consideration (e.g., Harris et al. 2006). They emphasize that it is the ratio of the two components that is important to consider. As this metallicity gradient is seen only in the Galactic Old Halo and not the whole Halo it is suggested that the Halo is partly constructed through merger and accretion processes with satellite systems.

1.6 The Origin of the Blue Mass-Metallicity Relation

Why might the blue-MMR exist? Mieske et al. (2006b) outline five physical mechanisms: 1) presence of contaminators; 2) accretion of GCs from low-mass galaxies; 3) stochastic effects; 4) field-star capture; 5) self-enrichment. There is also another mechanism proposed in the literature: 6) pre-enrichment. Details of each of these mechanisms are outlined below. Mieske et al. (2006b) emphasize that there has yet been no reason to suggest that the observations are explained by one mechanism alone.

1.6.1 Presence of Contaminators

It has been proposed that the more luminous GCs might fall into a separate category of objects called ultra-compact dwarf (UCD) galaxies. Hilker et al. (2007) elucidate that compared to typical compact dwarf (CD) galaxies, UCDs are more dense. UCDs were originally found independently through studies in the Fornax galaxy cluster of both GCs (Hilker et al., 1999) and compact dwarf galaxies (Drinkwater et al., 2000; Phillipps et al., 2001). Two objects were found in the former study while five (including a repetition of the previous two) were found in the latter. Further studies (Drinkwater et al., 2004) have revealed more than 50 UCDs in this cluster. Other UCDs have also been found in the Virgo (Haşegan et al., 2005; Jones et al., 2006; Evstigneeva et al., 2007b), Centaurus (Mieske et al., 2007) and Hydra clusters (Wehner & Harris, 2007), as well as Abell 1689 (Mieske et al., 2004). Evstigneeva et al. (2007a) also looked at less dense environments and found UCD candidates in the Dorado and NGC 1400 groups, with further non-detections in the NGC 0681, 4038, 4697 and 5084 groups. In addition to UCDs diminishing the gap between very luminous GCs and dwarf elliptical galaxies, Chilingarian & Mamon (2008) propose that they have found a compact object near M59 that lies between UCDs and dwarf ellipticals, and suggest it may have formed as a result of tidally stripping a low-luminosity elliptical.

There are three main scenarios which could explain UCD formation. The first is that UCDs are the surviving cores of dwarf elliptical nuclei (dE,N; Zinnecker et al. 1988; Bekki et al. 2001b; Harris et al. 2006). The outer stars of the dE,N are thought to be stripped away in a process called "galaxy threshing" (Bekki et al., 2001a). This threshing occurs as the dE,N interact with their

host galaxy. It causes their cores, which tend to be more massive than regular GCs, to be left behind and so populate the brighter end of the CMDs.

A second possibility is that UCDs form from an amalgamation of stellar super-clusters which are themselves a collection of young massive star clusters (Fellhauer & Kroupa, 2002). In their analysis, Mieske et al. (2006a) find that the Fornax UCDs are more consistent with the merger model, where the young massive clusters (YMCs) themselves merge during the galaxy-galaxy merger. The result of the merging YMCs would then be the progenitors for the UCDs. However, the Virgo UCDs are more consistent with the threshing model. In looking at differences between UCDs and dE,N, De Propris et al. (2005) find that UCDs are generally more extended and have higher surface brightnesses than dE,N, which tend to have luminosities, colours and sizes closer to those of Galactic GCs. Wehner & Harris (2006) look at the possibility that dE,N are the low-mass analogues of super-massive black holes.

In the third and final main scenario, Wehner & Harris (2007) propose that the UCDs really are just an extension of the lower-mass GCs up to higher masses. For example, Hilker et al. (1999); Drinkwater et al. (2000); Mieske et al. (2002); Evstigneeva et al. (2007b) suggest that these candidates are massive, intra-cluster GCs.

Haşegan et al. (2005) find evidence for all three scenarios in examining M87 and as such call this collection of objects, "dwarf-globular transition objects" (DGTOs). This counters the argument from Mieske et al. (2006b) who say that the required numbers of these contaminators make it unlikely that the contamination model can explain the observed blue-MMR. Spitler et al. (2006) argue that the blue-MMR is not simply a feature of luminous MP GCs, but

seems to extend down to lower GC luminosities as well. They argue that it is therefore not likely to be due to an additional population at the brighter end. It is also interesting to note that while Harris et al. (2006) find the dE,N appear as an extension of the blue side of the GC distribution Wehner & Harris (2007) find that their UCDs are an extension of the red side. Hilker et al. (2007) find that for objects with masses above $\backsim 10^6$ $M_\odot$ the mass-to-light (M/L) ratio increases above typical values expected for a 10^6 $M_\odot$ GC. Several explanations are put forward including that 1) UCDs form in concentrations of dark matter sub-structure, and 2) a top- or bottom-heavy IMF may explain observations where unseen mass is contributed by massive-star remnants (e.g., white dwarfs, neutron stars or black holes) or low-mass stars, respectively. Mieske & Kroupa (2007) propose that if the UCDs were to be explained by dark matter, the distribution needed (i.e., cuspy dark matter halos) would be inconsistent with what is presently seen (i.e., cored dark matter profiles, e.g., seen by Gilmore et al. (2007) in dwarf spheroidal galaxies). However, they propose tests that they hope will reveal whether or not bottom-heavy IMFs can account for the high (M/L) ratios. Dabringhausen et al. (2008) say that because continuity exists between the GC and UCD populations that the formation process is likely to have been the same, but because the mass-radius relations are different then the evolution must not have occurred in the same way.

1.6.2 Accretion of GCs from Low-Mass Galaxies

Mieske et al. (2006b) argue that for GCs accreted from galaxies with a range of masses, MMR relations will be observed if a) the *mean* GC colour of

the accreted GCs varies with the original host galaxy, and b) more luminous GCs form in deeper potential wells associated with their original host galaxy. a) is observed as already discussed in section 1.1 (see Larsen et al. 2001; Peng et al. 2006), and b) is also seen (Jordán et al., 2006). Mieske et al. (2006b) can simulate a weak MMR after combining some of their data from low-mass galaxies that themselves do *not* show a trend. The weakness of the trend that is simulated compared to what is observed leads them to discount this mechanism as a major contributor. They claim, however, that it is one plausible way to account for the non-detection of the blue-MMR in NGC 4472, and briefly explain that this would be due to different accretion and merger histories.

1.6.3 Stochastic Effects

Red giants will dominate the red and near-infrared passbands (e.g., Cerviño et al. 2002 and references therein), so is it possible that they could skew the GC luminosity distribution and produce or contribute to the observed MMR? Mieske et al. (2006b) state that any stochastic effect will be weaker for higher GC luminosities (where there are a larger total number of stars) and also for bluer bands (where there is lower average stellar luminosity). As such, it is unlikely that the stochastic effects have an effect on the MMR which is dominated by the brighter GCs.

1.6.4 Field-Star Capture

Bica et al. (1997) argued that with their results of N-body calculations a significant fraction of stars within a cluster may have been captured. This

was proposed to explain a double red giant branch seen in a Galactic GC, HP1 (Ortolani et al., 1997). Mieske et al. (2006b) quantify this scenario and estimate that for a GC of mass $10^6 M_{\odot}$ approximately 6000 stars (or 1.5% of the total assumed GC luminosity) would be captured in a Hubble time. This small fraction is not able to explain the observed effects. However, if the authors use a smaller orbital distance of 1 kpc (as opposed to the previously used 3 kpc) they find that the number of captured stars increases to about 4 x 10^4 (or 10%). Considering the opposite effect of cluster stellar evaporation, Mieske et al. (2006b) conclude that evaporation would not be significant as it has the overall effect of making the GCs bluer over time due to the loss of redder, lower-mass stars. This mechanism, along with self-enrichment or a combination of the two processes, are the two that Mieske et al. (2006b) favour to explain their observations. Mieske & Baumgardt (2007) revisit this topic, and comment that Bica et al. (1997) and Mieske et al. (2006b) previously used an approach which neglected the fact that field stars are gravitationally influenced by the cluster even before they are captured or interact with it. This additional fact reduces the ratio of captured field stars to star cluster stars to $\lesssim 10^{0.4}$, even when the field star velocity dispersion is very low (σ=15 km s^{-1}. Mieske & Baumgardt (2007) conclude that field star capture cannot explain the observed MMRs.

1.6.5 Self-Enrichment

Self-enrichment (like section 1.6.6) is one scenario implied from the observed star-to-star homogeneity in iron-peak elements (section 7.3.2 in Ashman & Zepf 1998). Unlike pre-enrichment, however, this occurs in the proto-GC

itself where there are multiple generations of star formation. The first generation of stars within the GCs must no longer be visible if they are to account for the enrichment of the GCs. To form a MMR, the more massive clusters must - with their deeper potential wells - be able to more efficiently retain their metals. The main problem with this scenario is how to get the metals well-mixed before the currently visible stars start forming. However, it does naturally explain the lack of MMR seen for the red subpopulation as these MR GCs are already metal-enriched, and so any further supernovae will only cause a relatively small metallicity increase (Mieske et al., 2006b). This mechanism, along with field-star capture or a combination of the two processes, are the two that Mieske et al. (2006b) favour to explain their observations. It remains to be seen whether or not self-enrichment can account for the galactocentric dependence that these authors see. Fan et al. (2007) see no relation between luminosity and metallicity for their sample of GCs in M31, which they say indicates self-enrichment is unimportant - at least in M31.

Within our own Galaxy, Omega Centauri (ω Cen) is a prime candidate for the self-enrichment mechanism where it would have formed in isolation and then would have been captured by the Galactic potential well (Carraro & Lia, 2000; Bekki & Freeman, 2003; Tsuchiya et al., 2004). Ikuta & Arimoto (2000) present evidence against ω Cen forming as an isolated system. Other suggestions are also made, including a GC seed which collected up to 40% older galactic field stars during its formation process (Fellhauer et al., 2006) or an alternative formation through mergers between clouds, clusters and dwarf galaxies (Icke & Alcaino, 1988; Norris et al., 1997; Tsujimoto & Shigeyama, 2003).

1.6.6 Pre-Enrichment in GCs embedded within Giant Molecular Clouds

Pre-enrichment (like section 1.6.5) is another scenario implied from the observed star-to-star homogeneity in iron-peak elements (section 7.3.2 in Ashman & Zepf 1998). Here, however, proto-GCs form within a giant molecular cloud (GMC), and it is within this GMC that the enrichment occurs. This assumes the metals in GCs formed before the GCs themselves, and requires those metals to be well-mixed in the protogalactic clouds.

In a series of three papers, Parmentier et al. (1999; 2000; 2001) study and model pre-enrichment of Galactic Halo GCs. The first paper (Parmentier et al., 1999) aims to counter the main argument, i.e., that supernovae would be too disruptive to allow GC formation through this method. Their model produces metallicities in agreement with those observed. Based on this pre-enrichment model, the second paper (Parmentier et al., 2000) discusses a scenario where the Halo is partly built by accretions and mergers, which they say explains why there is a metallicity gradient seen in the Old Halo and only in the Old Halo - i.e., not in the whole Halo. In their final paper (Parmentier & Gilmore, 2001), an MMR in the Old Halo GCs is shown to be statistically present. This MMR, whereby the least massive old clusters are the most metal-rich (see section 1.5.2), is claimed to be consistent with the pre-enrichment model.

1.6.7 Origin of Blue-MMR Summary

The accretion of GCs from low-mass galaxies is statistically unlikely, as are any contributions from stochastic effects (Mieske et al., 2006b). While field-star capture was thought possible (Mieske et al., 2006b), Mieske & Baumgardt

(2007) realize gravitational influences - previously neglected in calculations - also greatly reduce the likelihood of this scenario. Contaminators may not be able to explain the blue-MMR as 1) the required numbers are too large (Mieske et al., 2006b), and 2) Spitler et al. (2006) claim that the blue-MMR extends to lower luminosities. However, Dabringhausen et al. (2008) suggest that the continuity between GCs and these brighter objects imply that the formation was the same, while the different mass-radius relations could have arisen from different evolutionary paths. Finally, self- and pre-enrichment scenarios (which cannot currently be distinguished observationally) can explain both the blue-MMR and the lack of a red-MMR. These latter two scenarios appear the most promising, although the presence of contaminators may also be a valid explanation.

1.7 Aims of this Work

Brightest Cluster Galaxies (BCGs) are rare and are found at the centres of rich clusters of galaxies. The largest GCS populations are found in these BCGs. This paper focusses on the bimodality of the GCSs, and so concentrates on the GCSs of fifteen BCGs, as shown at the centre of each of the figures in figure 1.3. The aim of this paper is to look at the mass-metallicity relation in more detail than two previous works, Harris et al. (2006) and Wehner et al. (2008a). We will use not only the total of nine galaxies studied in those works, but will also include new data for six more galaxies. Chapter 2 details the data reduction. In chapter 3 we determine the blue-MMR for each GCS and

search for a possible correlation between the blue-MMR with the host-galaxy luminosity. Chapter 4 discusses and concludes this work.

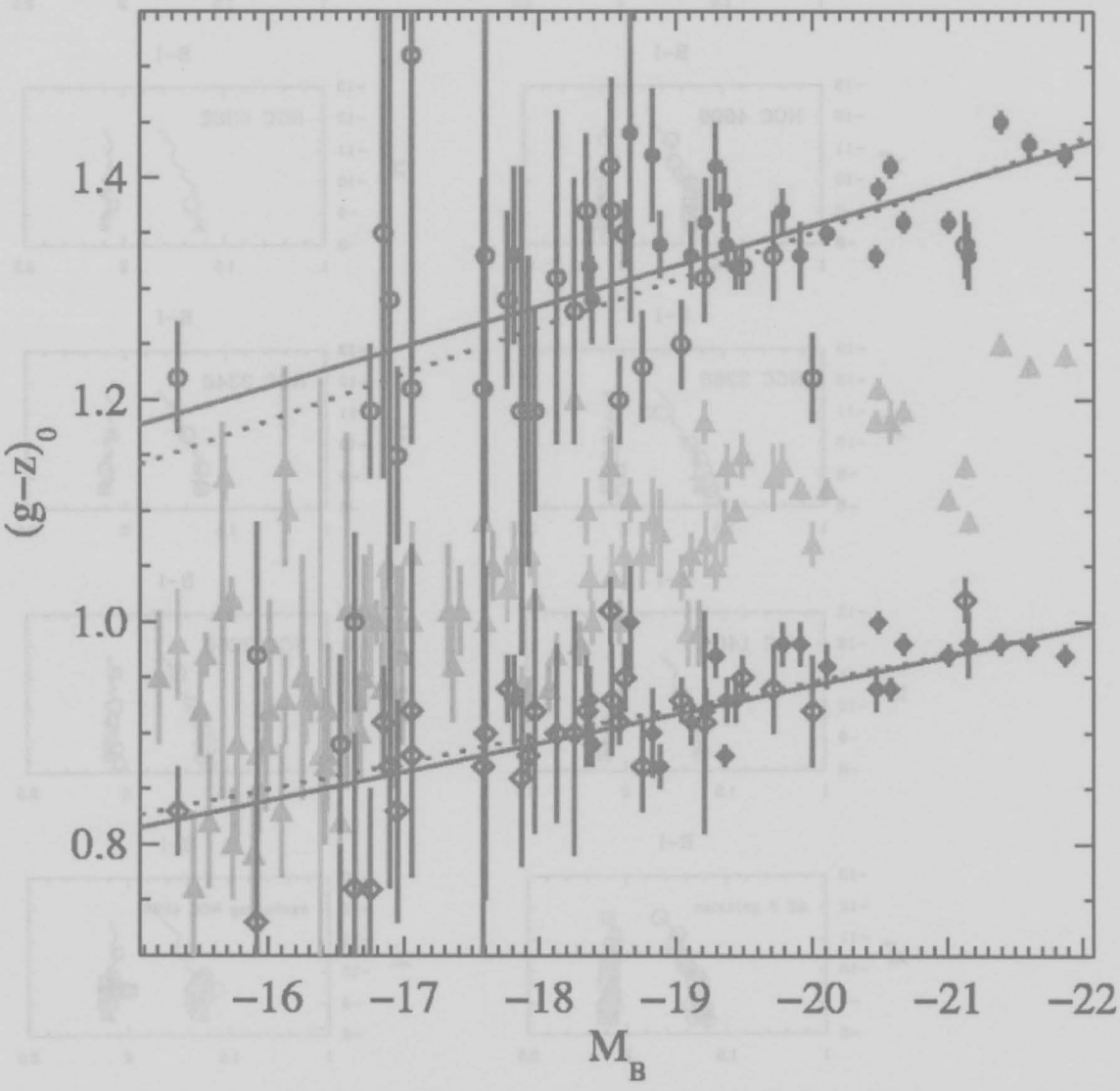

Figure 1.1: An example of the mean colour of GC subpopulations within one galaxy plotted against the luminosity of the host galaxy, for many different galaxies - described in section 1.5.1. The lower line indicates the blue subpopulation; the upper line, the red. Taken from figure 3 in Peng et al. (2006).

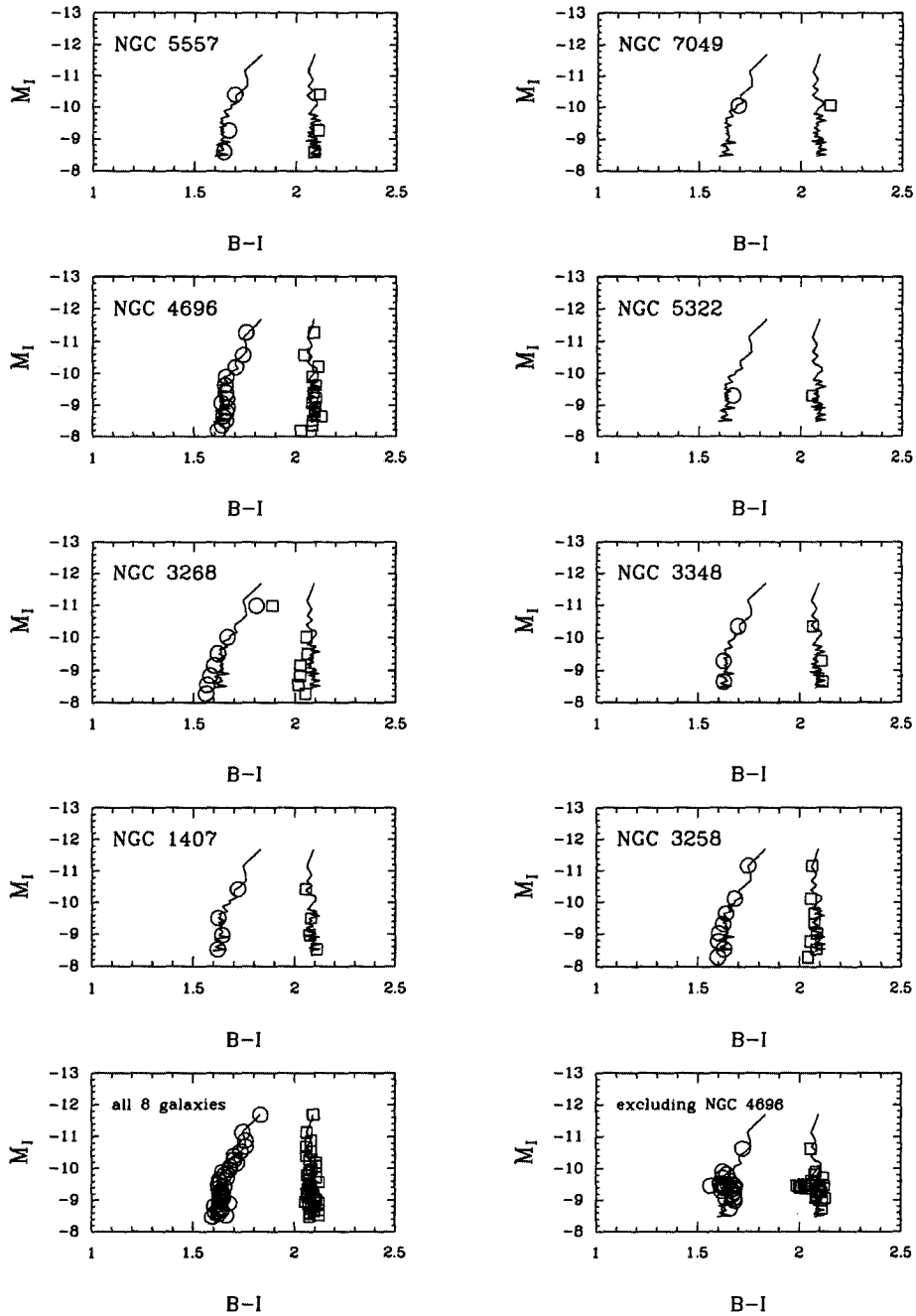

Figure 1.2: Examples of the blue mass-metallicity relation - described in section 1.5.2. Taken from figure 20 in Harris et al. (2006).

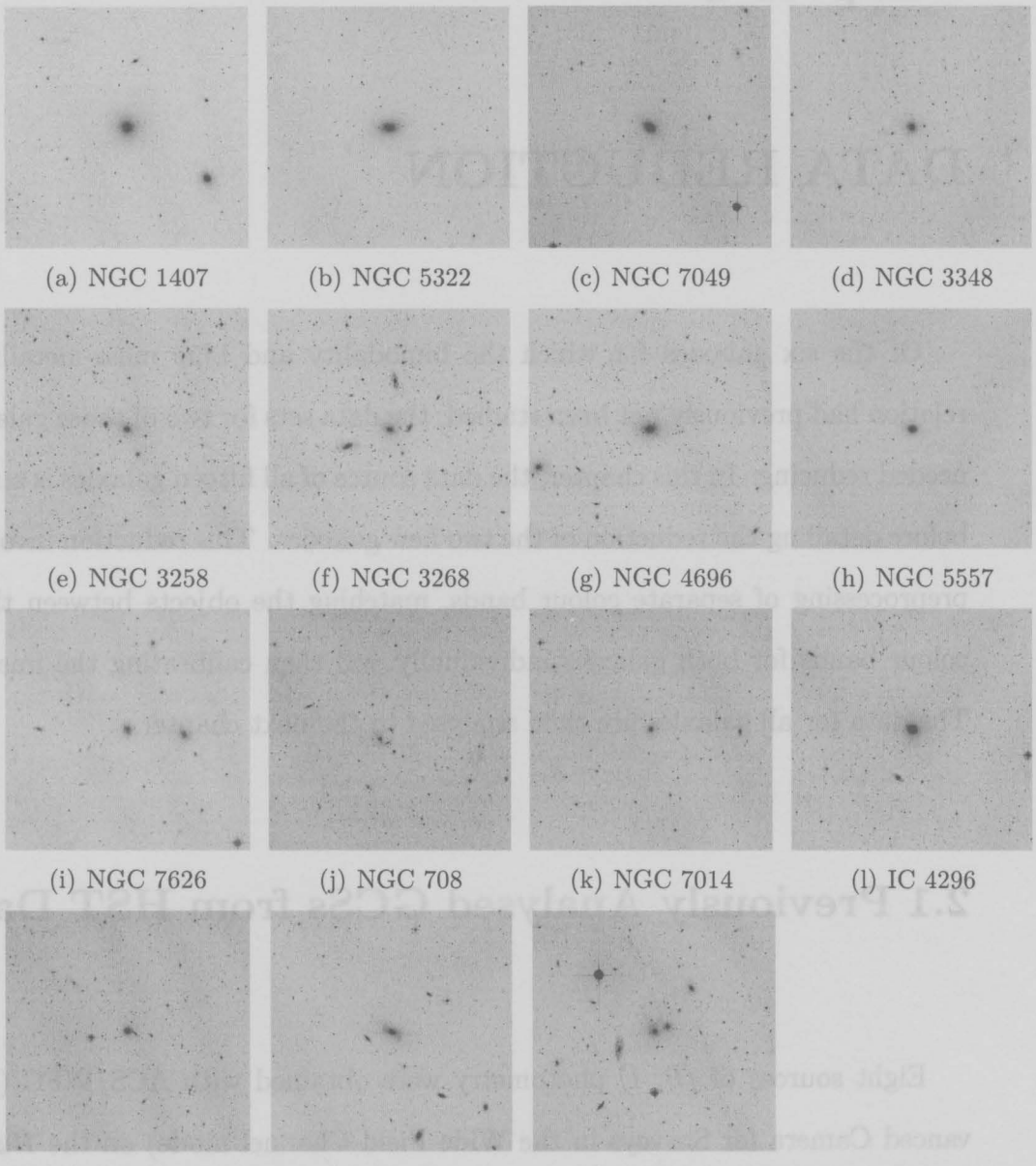

(a) NGC 1407 (b) NGC 5322 (c) NGC 7049 (d) NGC 3348

(e) NGC 3258 (f) NGC 3268 (g) NGC 4696 (h) NGC 5557

(i) NGC 7626 (j) NGC 708 (k) NGC 7014 (l) IC 4296

(m) NGC 5193 (n) IC 4329 (o) NGC 3311

Figure 1.3: All fifteen BCGs in SAO DSS images (30′x30′)

Chapter 2

DATA REDUCTION

Of the six galaxies for which the bimodality and blue mass-metallicity relation had previously not been studied, the data sets for two of those galaxies needed reducing. In this chapter, the data source of all fifteen galaxies is stated before detailing the reduction of the two new galaxies. This reduction involved preprocessing of separate colour bands, matching the objects between these colour bands for both galaxies individually and then calibrating the images. The data for all galaxies are then analysed in the next chapter.

2.1 Previously Analysed GCSs from HST Data

Eight sources of *(B, I)* photometry were obtained with ACS/WFC (Advanced Camera for Surveys in the Wide Field Channel mode) on the *Hubble Space Telescope* (HST). These sources were previously presented in Harris et al. (2006), and are analysed further here.

2.2 Newly Analysed GCSs from HST Data

There are an additional four galaxies included in this paper that use B photometry from the ACS, and I photometry from WFPC2 (Wide Field Planetary Camera 2).

2.3 Previously Analysed GCS from Gemini South Data

(g,i) photometry was obtained for NGC 3311 with the Gemini Multi-Object Spectrograph (GMOS) on Gemini South. This source was previously presented in Wehner et al. (2008a), and is further analysed here. The Gemini data is in *(g,i)* and not *(B,I)* because the GMOS camera only has filters in u, g, r, i and z - which is similar to the Sloan Digital Sky Survey (SDSS). A comparison between the Johnson-Cousins UBVRI and SDSS ugriz photometry systems can be seen in the reproduction of the figure by Jordi et al. (2006), shown in this chapter in figure 2.1.

2.4 Newly Analysed GCSs from Gemini South Data

Two new sources, NGC 5193 and IC 4329, of *(g-i)* photometry are analysed here. As with NGC 3311, this data comes from GMOS on Gemini South, and is part of a program (GS-2006A-Q-24) to look at GCSs in BCGs. The GMOS camera has a 5.5′ x 5.5′ field of view and an image scale of 0.146″ per pixel. The data for both g- and i-band images for NGC 5193 was obtained on the night of 2006 March 25, with thirteen images for g and twelve images for i; for

IC 4329, the g-band data (thirteen images) was obtained on the night of 2006 March 26 and the i-band data (twelve images) on the night of 2006 March 27.

2.4.1 Preprocessing

Within the Image Reduction and Analysis Facility (IRAF), the GMOS package was used to produce photometric images for NGC 5193 and IC 4329. The fifty raw images and their average air masses are shown in table 2.2. The *gprepare* command prepared all fifty of these raw GMOS data files for reductions. *gireduce* flatfielded and bias subtracted, with the flat and bias frames shown in table 2.3. *girmfringe* was used on i-band images only, and removed the fringes. A number of trials were conducted where the amplitude of the fringe frame subtracted was varied to find a satisfactory balance between getting good fringe subtraction while not losing quality in the images. For NGC 5193 and IC 4329 we found that amplitudes of 90% and 120% were optimal. The fringe frame used was the same as in Wehner et al. (2008a) which came from the Gemini Science Archives. *gmosaic* was the final command within GMOS that was used. In this process each of the three individual CCD chip images for the same field were mosaicked to produce one continuous image. The only default setting that was changed for *gmosaic* was "fl_clea". The default setting subtracts the overscan level. However, this introduces errors in the gaps between the chips so we chose to make the change to "fl_clea=no". After running *gmosaic*, we checked the mosaicked images to make sure that the background levels were similar across each of the previously separate chips.

Within the larger IRAF package, *imshift* was used to calculate the amount needed to shift all images within one band with respect to one image chosen

to be the reference frame. The x- and y-shifts obtained from *imshift* were then used in *imcombine* to actually combine the shifted images, producing one image in g and one in i for each of the galaxies - with the result that these final images probed fainter magnitudes than any individual image by itself. (Originally, *imcoadd* was unsuccessfully used where *imshift* and *imcombine* were successfully used instead. *imcoadd* appeared to work for the g-band but not for the i-band. The cause was uncertain, but we speculate that it was the fringe-frame subtraction as this was the only difference in the preprocessing up to this point.)

imcopy was used to then trim off the outer regions of the images so that the final four images had strut obscurations and edges removed. The results for the g-bands are shown in figures 2.2(a) and 2.3(a). As a comparison, the Smithsonian Astrophysical Observatory's Digitized Sky Survey (SAO-DSS) images are shown in figures 1.3(m) and 1.3(n). All images were viewed and printed to file with the SAOimage display utility (see figure 1.3).

2.4.2 Identifying Globular Cluster Candidates

DAOPHOT (the standalone version 4) and ALLSTAR were packages used to enable the identification of target objects within the four frames. NGC 5193 and IC 4329 are at distances of 56.6 $\pm$ 3.8 Mpc and 72.4 $\pm$ 4.6 Mpc, respectively (using values of cz, in the CMB reference frame, taken from the NASA Extragalactic Database (NED), and a value of $H_0 = 70$ km s^{-1}). At these distances stars within the GCs cannot be resolved but the GCs themselves look star-like - and this is why stellar packages such as DAOPHOT and ALLSTAR can be used to identify and measure the GCs. Both packages re-

quire information about the instruments used to obtain the images and also estimates for the parameters within those images. This information is contained within the daophot.opt, allstar.opt and photo.opt files (examples are shown in appendix section 5.1). The parameters of particular interest - the stellar full-width half-maximum (FWHM) estimates and the gain and noise for each of the CCD chips - are shown in tables 2.4 and 2.5, respectively. To create the point-spread function (PSF), one hundred objects were requested with the PICK command and an average of sixty objects per frame were used. This was enough to create a PSF fit that was quadratic in (x,y), which would account for any fluctuations across the image (e.g., scale distortions on the CCD chips).

In producing a list of target objects, ALLSTAR also produces an image from which it has subtracted all the objects. These images were then used in the process called "median subtraction", whereby most of the galaxy light is removed from an image. Within IRAF again, the image is 'smoothed over' with the *median* command using a small square of dimension 30 pixels (the images were 2001x2121 pixels for NGC 5193, and 2051x2001 pixels for IC 4329). Examples of the smoothed over images are shown in figures 2.2(b) and 2.3(b). This smoothed-over image was subtracted from the original image with the background count added back in, and the results of which are shown in figures 2.2(c) and 2.3(c). Some of the galaxy light at the very centre of the frame still remains, but the result has considerably less than in the figures 2.2(a) and 2.3(a).

The DAOPHOT and ALLSTAR packages were run again. With the galaxy light removed, more accurate target object identifications were achieved in

slightly greater numbers. Examples of the image with removed objects are shown in figures 2.2(d) and 2.3(d), and were used as a visual aid to check the accuracy of object identification and subtraction.

The file that ALLSTAR produces contains nine parameters associated with each object identified, including the x- and y-coordinates, and the magnitude and associated error. When error is plotted against magnitude, a subpopulation of false identifications can be seen as shown in the boxes of figures 2.4 and 2.5. The boxes' limits were chosen such that they would avoid overlap with real identifications. The false identifications, when their x- and y-coordinates are plotted, can be seen to be associated primarily with the innermost regions of the galaxies where the background light is bright or where the CCD chip was saturated. The objects within these regions were excluded from the work following.

To match the objects between each of the g- and i-images, the reduced list of images from ALLSTAR was input into DAOMATCH and DAOMASTER. DAOMATCH takes these two files, and produces outputs of the x- and y-shifts, rotations and magnifications needed to go between the two images. In both galaxies, the rotations and magnifications were extremely close to zero and one, respectively. DAOMASTER was then used to refine the estimate from DAOMATCH. DAOMASTER was restricted to being allowed to vary only the x- and y-shifts to transfer between one image and the other. DAOMASTER's outputs included a file with the coordinate transformation between the g- and i-band images, as well as a file with the g- and i-band detections matched up with their respective positions, magnitudes, etc.

As a self-check at this point, GEOMAP was used. Several tens of stars across the entire frames were matched manually in the g- and i-band images. The locations of these manually matched objects were recorded in a file that was then input into GEOMAP. Running GEOMAP then produced the coordinate transformation. As GEOMAP also allowed for rotation and magnification, the x- and y-shifts are close in value to those of DAOMATCH.

All DAOMATCH, DAOMASTER and GEOMAP outputs can be seen in table 2.6. The DAOMASTER x- and y-shifts have different values than those for DAOMATCH and GEOMAP because, as previously mentioned, the former was restricted to being allowed to vary only these transformations (i.e., no rotations or magnifications).

2.4.3 Calibration

There were two calibrations that needed to be made so that the arbitrary CCD magnitudes could be converted to standard apparent magnitudes.

The first calibration that needed to be made involved using images of standard stars of known apparent magnitude. The calibration stars used for NGC 5193 were Rubin 149 (RU149); for IC 4329, Selected Area 107 (SA107-F2-599). The standard images of RU149 and SA107 can be seen in plate 35 and 57, respectively, in Landolt (1992) which are reproduced here in figures 2.6(a) and 2.7(a). The calibration images taken for this project are shown in figures 2.6(b) and 2.7(b). See also table 2.2 showing file numbers, exposure times and airmass. As can be seen the airmasses are approximately the same as the raw science frames - but as this is only an approximation the zero-points of this calibration remain preliminary.

The standard star magnitudes were taken from the catalog[1] of standard stars produced by E. Wehner who transformed Landolt (1992) standard star UBVRI magnitude system to the Sloan Digital Sky Survey magnitude system (u, g, r, i and z) with the equations given by Fukugita et al. (1996).

Each standard star found on the calibration image was run through DAOPHOT to find an arbitrary magnitude for different aperture sizes. These magnitudes were then plotted against the aperture size (e.g., see figure 2.9) to determine which was the smallest aperture that could be used that still contained $\gtrsim 95\%$ of the light. An aperture size of 14.5 pixels was chosen. For each standard star within one colour image Δg, as given by equation 2.1, was then calculated. An average was then taken, to be used in equation 2.3.

Using the aperture size of 14.5 pixels, but this time on the science images, δg, as given by equation 2.2, was calculated for several tens of the brightest objects. This was done by removing all but those brightest objects in the image using SUBSTAR within DAOPHOT. DAOPHOT and ALLSTAR were then run again, without defining a new PSF, and the g_{ap} and g_{als} values were used to find δg, as shown in equation 2.2. When δg was plotted against g_{als} magnitude (see figure 2.8), the value around which the points converged at the brightest magnitudes was the value that was used for δg.

Both Δg, δg values are shown in table 2.1.

$$\Delta g = g_{catalog} - [g_{ap} + 2.5 log t_{exp}] \tag{2.1}$$

$$\delta g = [g_{ap} + 2.5 log t_{exp}] - g_{als} \tag{2.2}$$

[1] The catalog can be found at http://www.physics.mcmaster.ca/~harris/Databases.html

$$g = g_{als} + \delta g + \Delta g \tag{2.3}$$

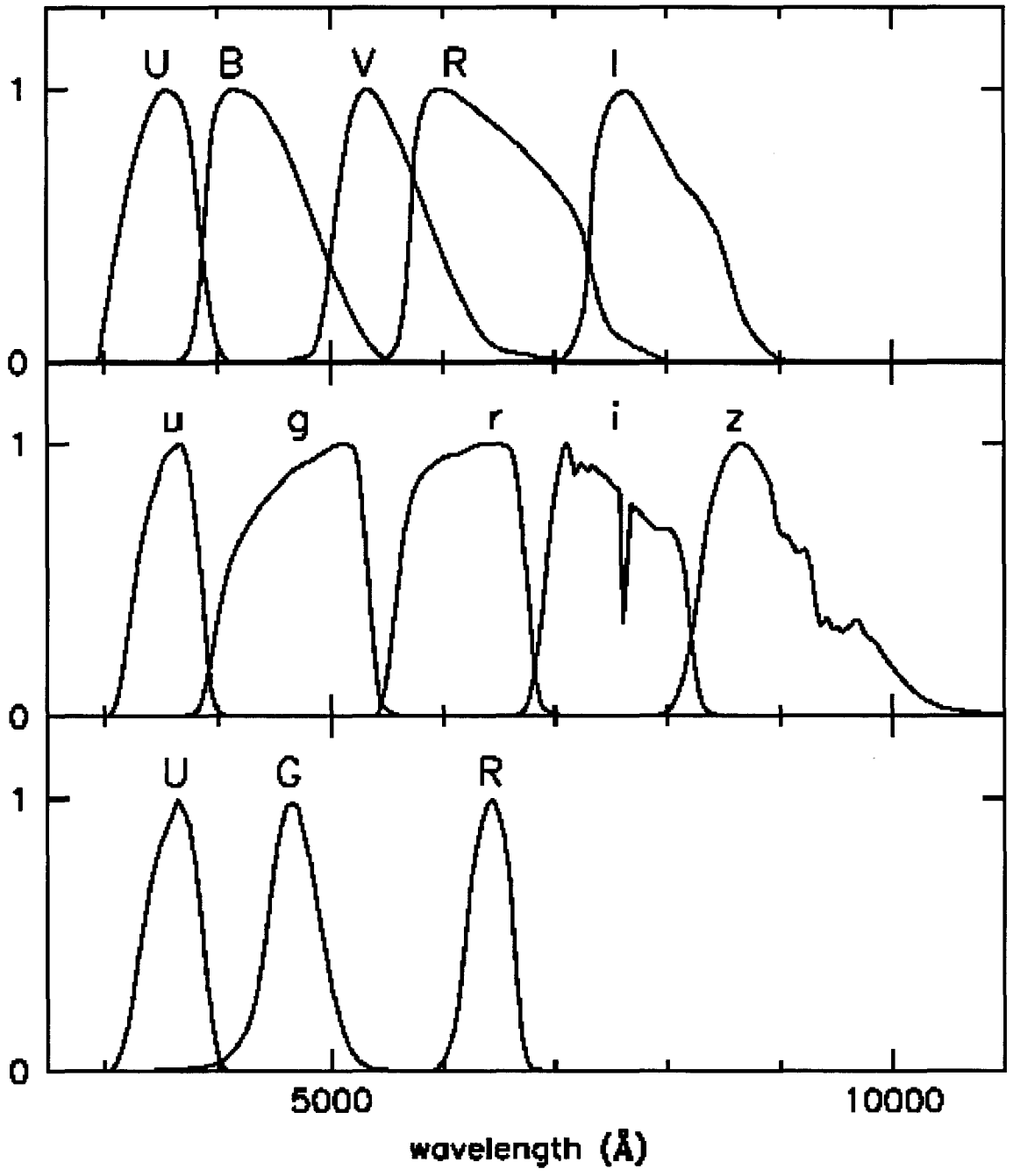

Figure 2.1: A comparison between the Johnson-Cousins UBVRI and SDSS ugriz photometry systems from Jordi et al. (2006). The lowest panel shows the RGU system (Becker, 1946) that was initially introduced to measure stellar parameters and Galactic structure.

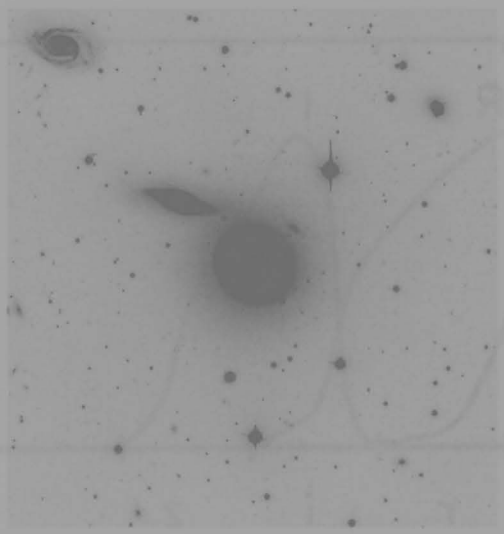

(a) NGC 5193 GMOS g image

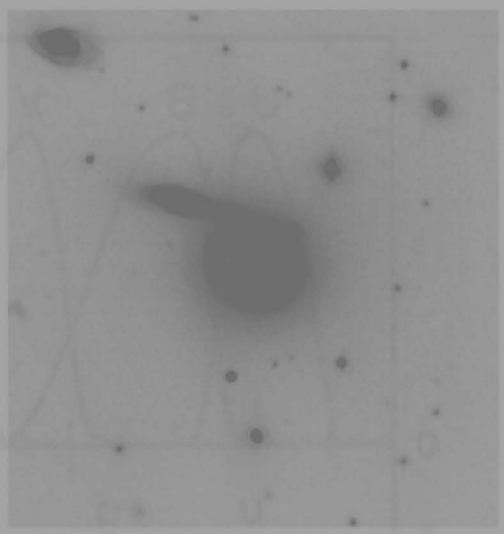

(b) NGC 5193 g smoothed over image

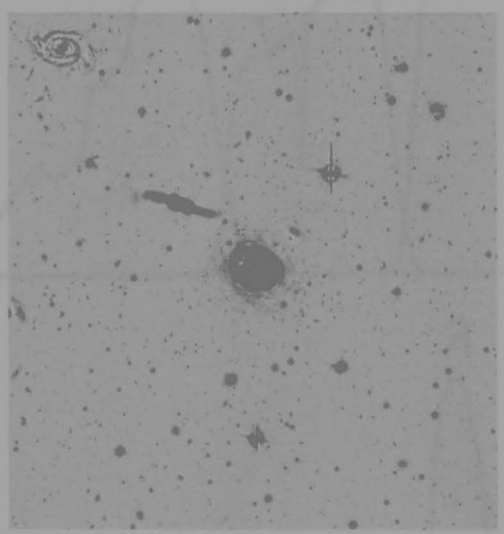

(c) NGC 5193 with galaxy light subtracted, i.e., 2.2(a) - 2.2(b)

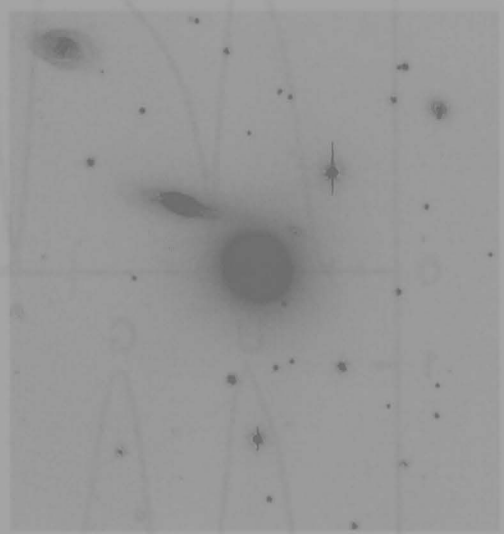

(d) NGC 5193 g subtracted image after median-subtracting and DAOPHOT/ALLSTAR. Note that all but the brightest objects have been removed in comparison to 2.2(a).

Figure 2.2: NGC 5193. See Section 2.4.2 for further details.

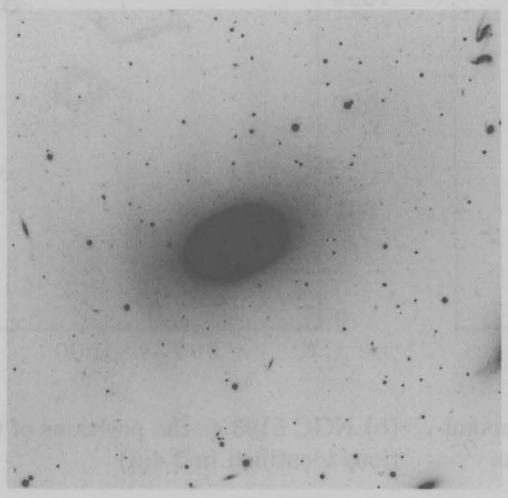

(a) IC 4329 GMOS g image

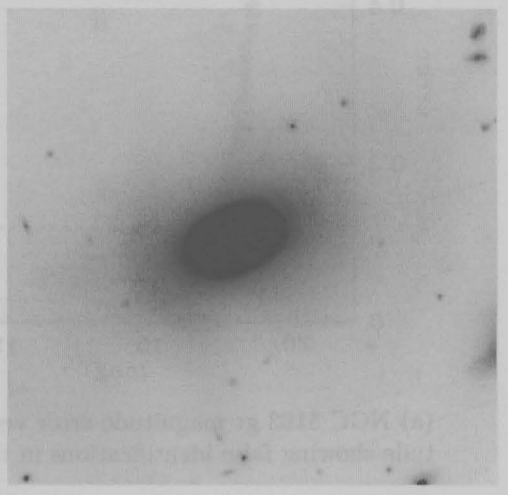

(b) IC 4329 g smoothed over image

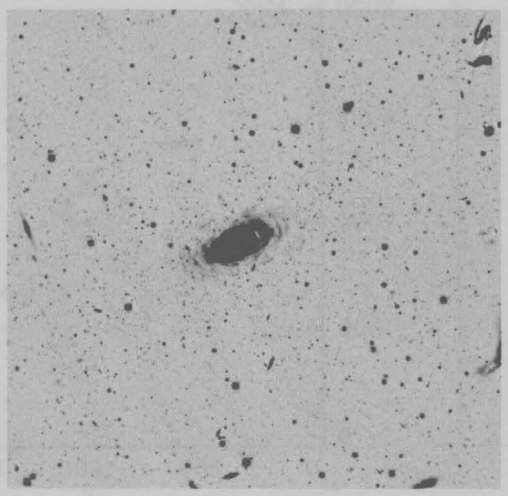

(c) IC 4329 with galaxy light subtracted i.e., 2.3(a) - 2.3(b)

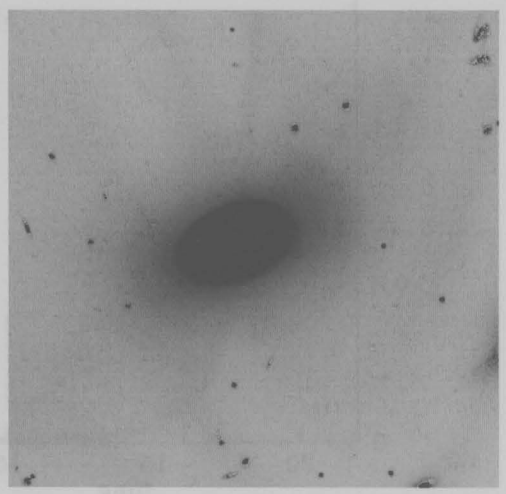

(d) IC 4329 g subtracted image after median-subtracting and DAOPHOT/ALLSTAR. Note that all but the brightest objects have been removed in comparison to 2.3(a).

Figure 2.3: IC 4329. See Section 2.4.2 for further details.

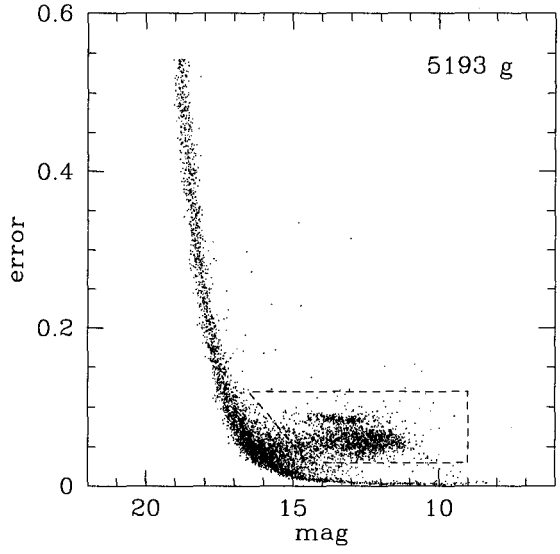

(a) NGC 5193 g: magnitude error versus magnitude showing false identifications in the box

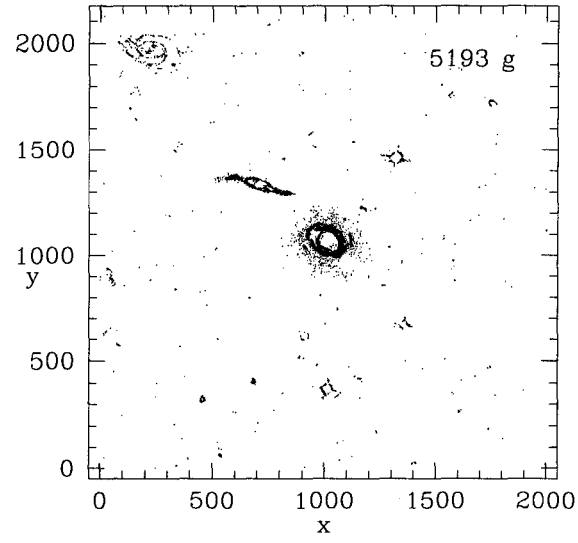

(b) NGC 5193 g: the positions of the false detections identified in 2.4(a)

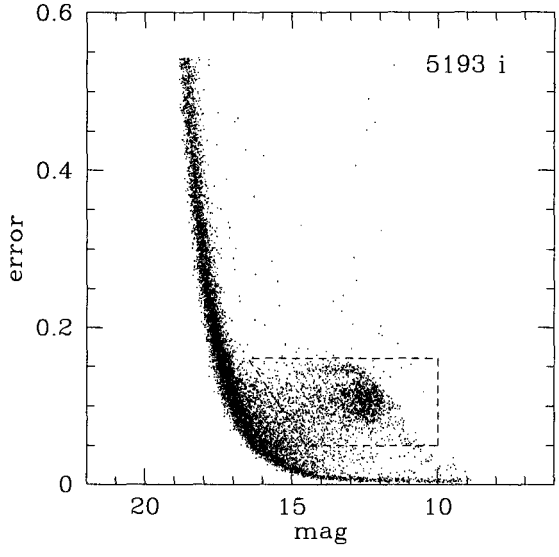

(c) NGC 5193 i: magnitude error versus magnitude showing false identifications in the box

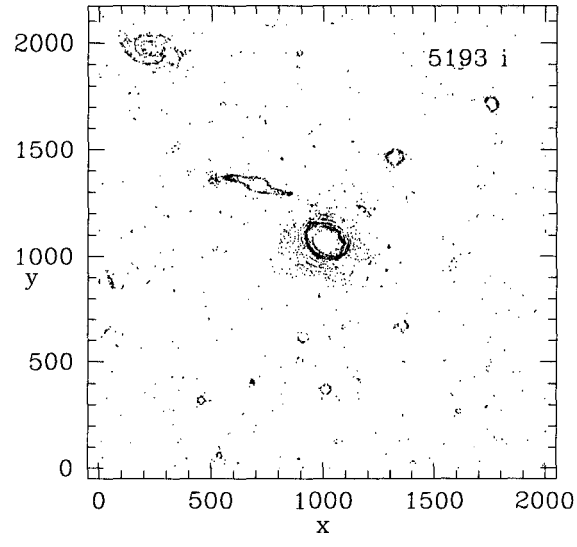

(d) NGC 5193 i: the positions of the false detections identified in 2.4(c)

Figure 2.4: NGC 5193 False Identifications and Their Positions

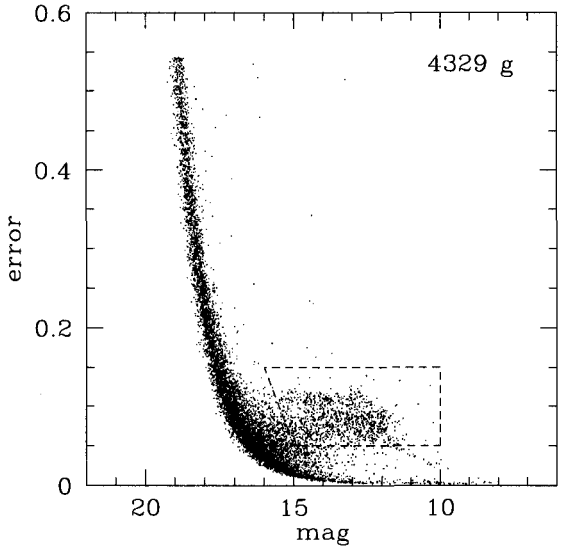

(a) IC 4329 g: magnitude error versus magnitude showing false identifications in the box

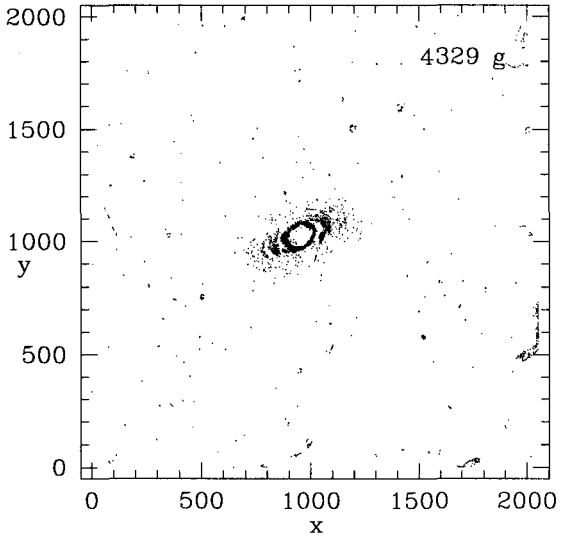

(b) IC 4329 g: the positions of the false detections identified in 2.5(a)

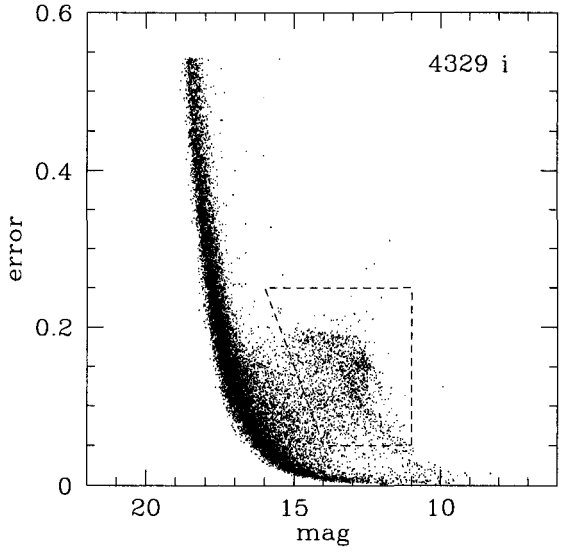

(c) IC 4329 i: magnitude error versus magnitude showing false identifications in the box

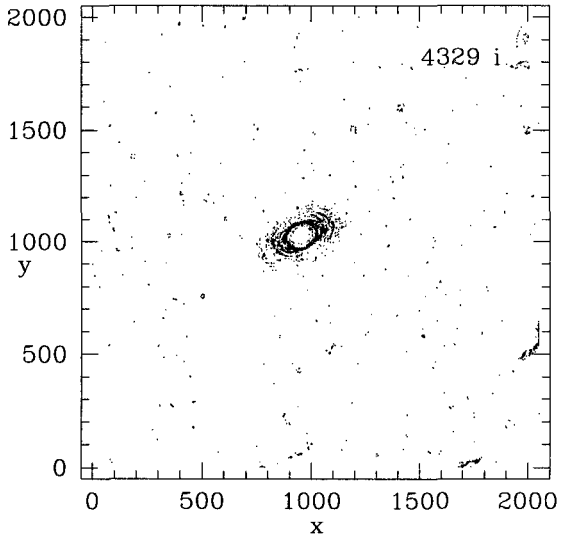

(d) IC 4329 i: the positions of the false detections identified in 2.5(c)

Figure 2.5: IC 4329 False Identifications and Their Positions

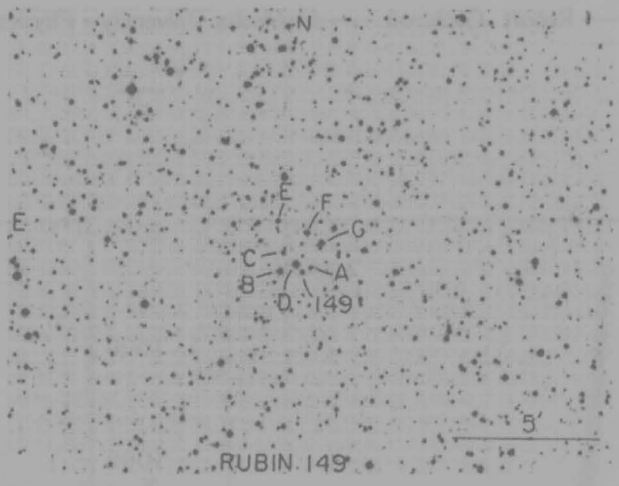

(a) Rubin 149, plate 35 from Landolt (1992)

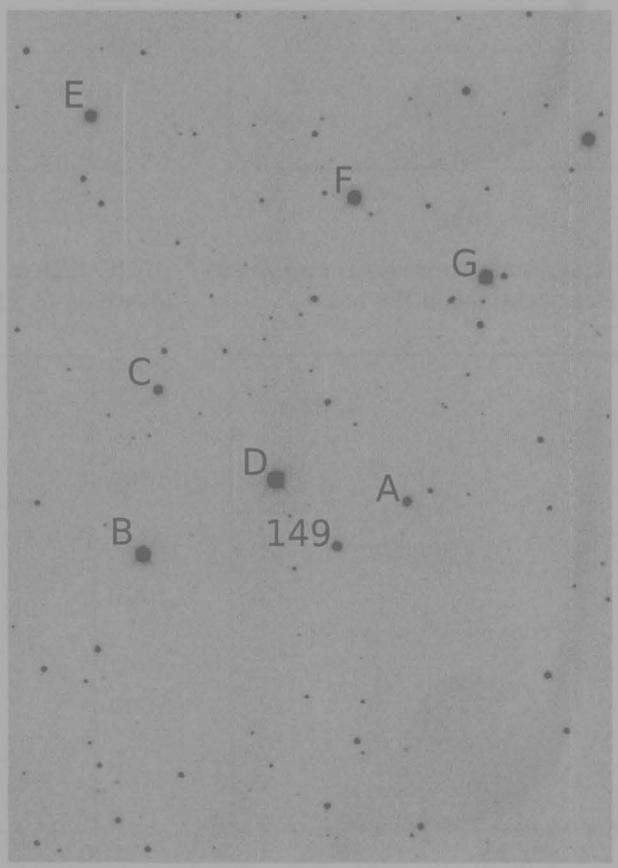

(b) Example of a calibration star image for Rubin 149i

Figure 2.6: Calibration for NGC 5193

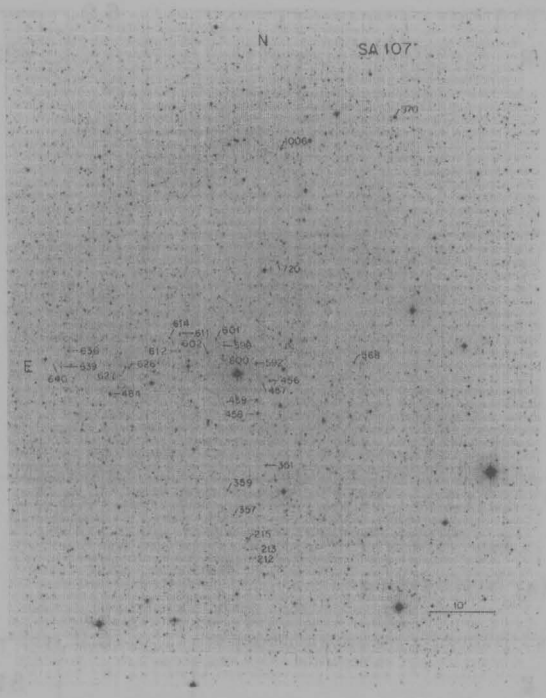

(a) SA107, plate 57 from Landolt (1992)

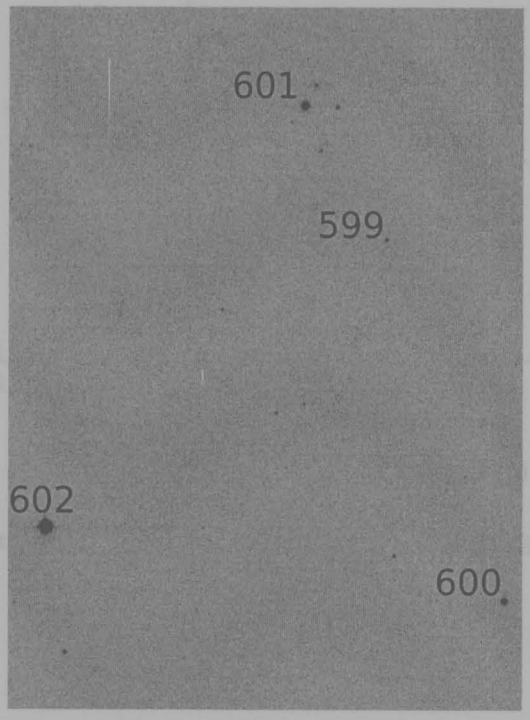

(b) Example of a calibration star image for SA107i

Figure 2.7: Calibration for IC 4329

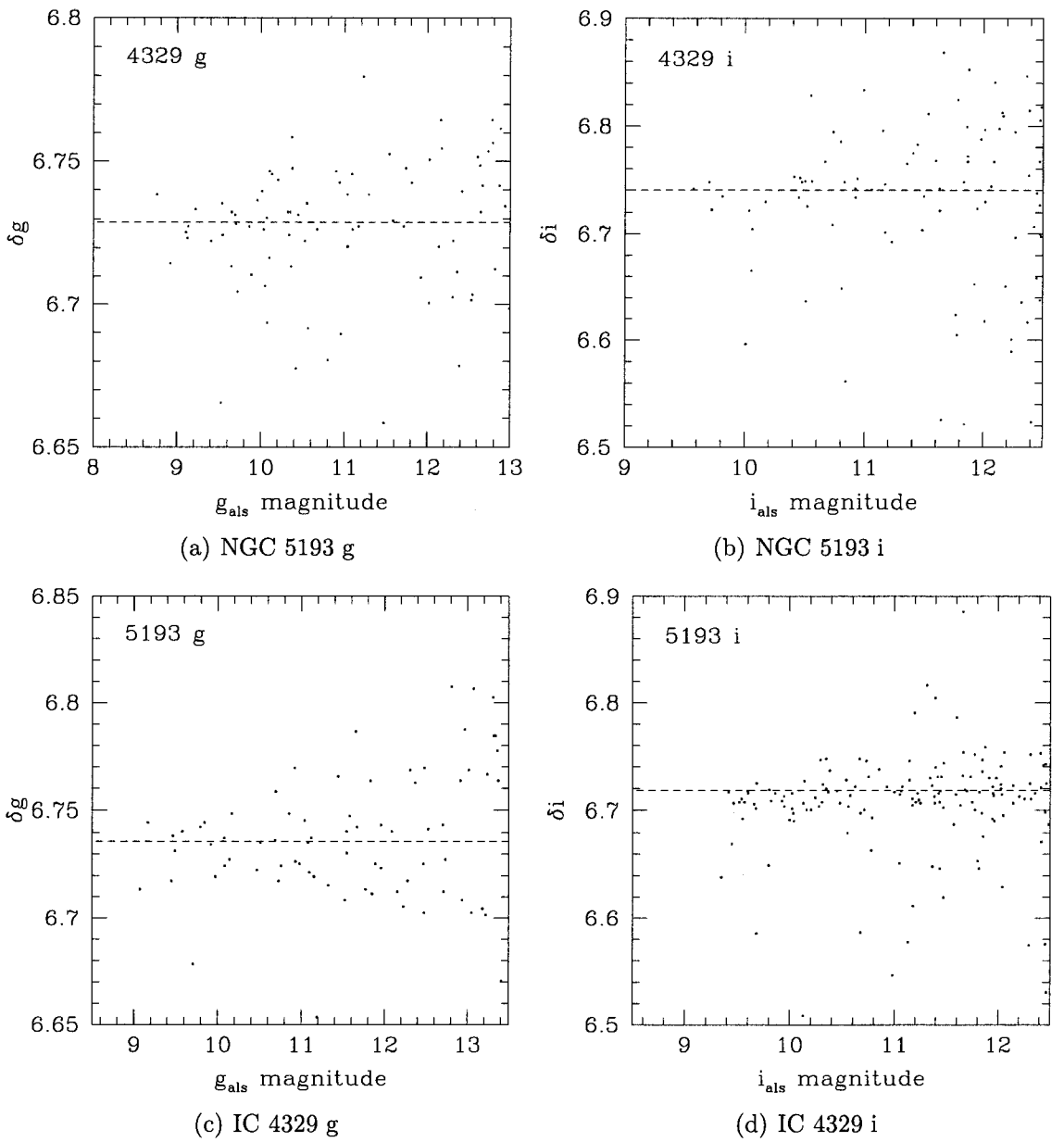

(a) NGC 5193 g

(b) NGC 5193 i

(c) IC 4329 g

(d) IC 4329 i

Figure 2.8: δg estimates for NGC 5193 and IC 4329

Table 2.1: Values of Δ and δ for NGC 5193 and IC 4329

Object	Filter	Δ	δ
5193	g	3.612(from Rubin g)	6.736
	i	3.241(from Rubin i)	6.718
4329	g	3.597(from SA107 g)	6.729
	i	3.386(from SA107 i)	6.740

Table 2.2: Gemini South GMOS Raw and Calibration Images: Exposure Time and Airmass

Target	File Number		Filter	Exposure Time (s)	Average Airmass
Science Object Images					
NGC 5193	S20060325S	0098-0110	g	500.488	1.156
		111-128	i	500.488	1.029
IC 4329	S20060326S	134-146	g	500.488	1.183
	S20060327S	109-120	i	500.488	1.234
Calibration Images					
Target	File Number		Filter	Exposure Time (s)	Average Airmass
Rubin 149	S20060325S00	75,76	g	3.5	1.15
		77,78	g	1.5	1.15
		83,84	i	3.5	1.15
		85,86	i	1.5	1.15
SA107	S20060326S0	147,148	g	3.5	1.28
		149,150	g	1.5	1.28
		151,152	i	3.5	1.29
		153,154	i	1.5	1.29
SA107	S20060327S0	121,122	g	3.5	1.31
		123,124	g	1.5	1.31
		129,130	i	3.5	1.34
		131,132	i	1.5	1.34

Table 2.3: Gemini South GMOS Flat Field, Bias and Fringe Frames

Frame	Original File Name
bias	GS20060202S0126_BIAS
g flat	GS20060228S0131_FLAT
i flat	GS20060208S0186_FLAT
fringe	RGS20060208S0100_FRIN

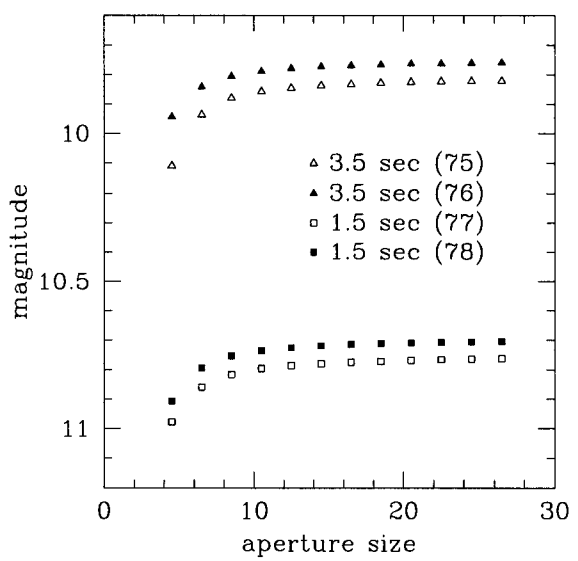

Figure 2.9: The curve of growth for the g frame of Rubin 149 Star C, as shown in figure 2.6(b) . Four images were obtained of this calibration star, two with an exposure length of 3.5 seconds and two with an exposure length of 1.5 seconds. The number in brackets after the exposure time refers to the file number, e.g., GS-CAL20060325-175 for 75.

Table 2.4: Full-Width Half-Maximum Values (in Pixels) Used for the Images

File	Filter	FWHM
5193	g	4
	i	3
4329	g	4
	i	3

Table 2.5: CCD Chip Gain and Noise

CCD Chip	001	002	003	average
gain (e^-/DN)	2.372	2.076	2.097	2.182
noise (e^- rms)	3.98	3.85	3.16	3.66

Table 2.6: NGC 5193 and IC 4329 Outputs from DAOMATCH, DAOMASTER and GEOMAP (all values in pixels)

Program	x shift	y shift	x mag	y mag	x rot	y rot
NGC 5193						
DAOMATCH	-1.89	-0.75	1.00104	1.00104	-0.00001	0.00001
DAOMASTER	-0.7829	0.3446	-	-	-	-
GEOMAP	-1.90919	-0.61871	1.00096	1.00103	0.00418	0.00543
IC 4329						
DAOMATCH	-1.59	-0.93	1.00093	1.00093	-0.00003	0.00003
DAOMASTER	-0.6088	0.0695	-	-	-	-
GEOMAP	-1.62501	-0.79207	1.00093	1.00100	0.00857	0.00670

Chapter 3

ANALYSIS OF THE MASS-METALLICITY RELATION

First, CMDs were produced and relevant regions chosen within them to include the GCS and exclude much field contamination. Details of the MMR analysis followed, and are detailed here, with conversions and comparison between HST, Gemini and Mieske et al. (2006b) data.

3.1 Colour-Magnitude Diagrams

Before analysing the mass-metallicity relation, de-reddened colour versus absolute magnitude diagrams were needed. The information in table 3.1 was used in equations 3.1 to 3.5 to obtain de-reddened colours and absolute magnitudes. Table 3.1 lists in successive columns (1) the target's NGC or IC number, (2) the galaxy group or cluster, (3) the redshift cz of the galaxy, (4) the galaxy luminosity, M_V^T, (5) the foreground reddening, (6) the apparent distance modulus, (7) the number of data points within the initial selection region (see sections 3.1.1 and 3.1.2 for details of the selection regions), (8) the total number of GCs estimated to be in the system, and (9) the specific frequency, S_N. See appendix section 5.2 for information on how (8) and (9) were

calculated. The specific frequency, S_N, of GCs as a function of host-galaxy luminosity can be seen in figure 3.1 and shows that NGC 3311 is a special case.

The standard distance modulus equation is

$$m_\lambda = M_\lambda + 5log_{10}d_{pc} - 5 + A_\lambda, \tag{3.1}$$

and the extinction equation for *(B, I)* colours, for example, is

$$(B-I)_0 = (B-I) - E(B-I), \tag{3.2}$$

where

$$E(B-I) = A_B - A_I. \tag{3.3}$$

3.1.1 HST Data

For the ACS/WFC data the values of *cz*, M_V^T, *E(B-I)* and *(m-M)*$_I$ were taken from Harris et al. (2006). For NGCs 708 and 7014 and IC 4296, values for V_T[1], A_B, A_V, A_I and *cz* (the CMB reference frame) were taken from the NASA Extragalactic Database (NED). The value of *cz* used for each galaxy was that of the associated cluster to exclude any contamination of distance estimates by the galaxy's random motion within the cluster.

(m-M)$_0$ was calculated using an adopted value of $H_0 = 70$ km s^{-1} Mpc^{-1}, using the following equation:

[1] Unlike for the other galaxies, V_T for NGC 708 is listed as $V_{T(25)}$, i.e., referring to the 25^{th} magnitude isophote.

$$(m - M)_0 = 5log_{10}[\frac{cz[kms^{-1}]}{H_0[kms^{-1}]}10^6] - 5. \quad (3.4)$$

M_V^T was then calculated from

$$M_V^T = V_T - A_V - (m - M)_0. \quad (3.5)$$

For NGC 7626, there was a discrepancy between the velocity of the Pegasus Group (also known as the Pegasus I Group), which was found to be 3826 km s^{-1}, and NGC 7626, which had a velocity of 3034 km s^{-1}. Additional sources for the velocity measurement of NGC 7626 were found. These included v_{helio} = 3345 ± 9 km s^{-1} (Denicoló et al., 2005), cz_{helio} = 3409 ± 19 km s^{-1} (Bernardi et al., 2002), cz = 3417 ± km s^{-1} (Smith et al., 2001), cz = 3403 ± 10 km s^{-1} (Wegner et al., 1999), and cz = 3405 ± 4 km s^{-1} (Trager et al., 2000).

Balcells & Carter (1993) commented on the very unusual core of NGC 7626 - even for kinematically peculiar cores. They saw that by using only a Gaussian to fit background velocities and carry out decomposition, incorrect velocity values for features within the galaxy would be obtained. All velocity peaks in their analysis were asymmetric. The interesting core kinematics imply a recent merger, as do the results from Sikkema et al. (2006) who look at six shell galaxies - including NGC 7626. Sikkema et al. noted that NGC 7626 has an abnormal number of luminous clusters ($M_I = -12.5$), the bimodality of the GCs is not fit well by a simple bimodal form because their histogram showed a broad flat peak, and NGC 7626 is located in a low density region (as are the other five galaxies in their paper).

Hibbard & Sansom (2003) say that the optical velocity of NGC 7619 (the other galaxy in the pair at the centre of the Pegasus Group) is $v_{\odot} = 3758$ km s^{-1}. Sadun et al. (2007) state that NGC 7626 is an X-ray Bright Optically Normal Galaxy, and Hibbard & Sansom (2003) say that it is also a radio galaxy with two symmetric jets. There is a faint HI emission outside the optical body of NGC 7626.

As mentioned previously, NGC 7626 lies in the Pegasus Group. The Pegasus Group is also known as the Pegasus Cluster, the Pegasus I Cluster, SRGb031 and as U842. The Pegasus II Cluster is a background cluster in the same line of sight (Chincarini & Rood, 1976; Levy et al., 2007). Kim et al. (2007) measure NGC 7619's velocity to be 480-650 km s^{-1} relative to the intra-cluster medium (ICM). They speculate that it could be because NGCs 7619 and 7626 are likely to be close to the bottom of the Group's potential well and experience motion there, or that the two galaxies are in orbit around one another. The tail structure associated with NGC 7619 could also be due to a tidal interaction with NGC 7626. Levy et al. (2007) find that there are actually three groups of galaxies in the line of sight of the Pegasus clusters: a foreground, a central and a background group. They find that NGCs 7619 and 7626 fall in the velocity range of the central group which is composed of thirty members, and has a mean redshift of 3900 km s^{-1} and a range of 3400 to 4400 km s^{-1}.

Ramella et al. (2002) combine the Updated Zwicky Catalogue (UZC) and the Southern Sky Redshift Survey (SSRS2) into the UZC-SSRS2 Group Catalog (USGC). The Pegasus Group, identified as U842 in the USGC, has a heliocentric group velocity of 3525 ± 414 km s^{-1}.

As the core of NGC 7626 was shown to be peculiar, in addition to the possible interaction with NGC 7619 at the centre of the Group's potential well, we chose the velocity of the Group as found by Ramella et al. (2002) to be the velocity that we used further. This velocity was corrected to the CMB reference frame using the velocity calculator of NED giving a result of 3154 km s^{-1}. It was this velocity that was then used in table 3.1.

Once the values in table 3.1 had been found for all galaxies, they were used to obtain de-reddened colours and absolute magnitudes so that CMDs could be plotted. The GCS on a CMD stands out as a vertical sequence. Data points were selected from an initial region enclosed within the limits $1.2<(B-I)_0<2.8$ and $-10.5<M_I<-7.5$ (see example figure 3.3). The number of data points within this initial selection region is shown in column (7) of table 3.1. As already mentioned in section 1.5.1, using *(B-I)* colours allows a greater sensitivity to the metallicities. M_I were used (as opposed to M_B) because the values of M_I most closely resemble the actual GC luminosity and where it peaks. The limits of $(B-I)_0$ were used to minimize contamination by field stars. The fainter limit of $M_I<-7.5$ was used not only for that similar reason, but also because at fainter magnitudes the limit of the B filter is reached (seen, for example, at the bottom of figure 3.3). The brighter limit of $M_I>-10.5$ was increased incrementally to brighter magnitudes to see what effect, if any, this would have on the mass-metallicity relation.

3.1.2 Gemini Data

A similar process was completed here for the Gemini data as for the HST data in the previous section. To the data from NGC 5193 and IC 4329, we added that of NGC 3311 from Wehner et al. (2008a).

Values for V_T, A_V and cz (the CMB reference frame) were taken again from the NASA Extragalactic Database (NED). To calculate the values of A_g and A_i, all the values of extinction in the UBVRI system were plotted (as shown in the example figure 3.2). Using this approximate $1/\lambda$ correlation, extinction values in the g_{475}- and i_{780}-bands were read off from this graph.

NGC 5193 has, in the past, been incorrectly associated with the Abell 3560 cluster, but Willmer et al. (1999) and Bardelli et al. (2002) point out that both NGC 5193 and NGC 5193A are foreground objects, and as such are instead associated with Abell 3565. Abell 3565 is a cluster centered on IC 4296 (Vettolani et al., 1990). For IC 4329, we list the associated group as Abell 3574, although this group is also known as Shapley 1346-30, K27, the IC 4329 group and Centaurus North (Phillipps et al., 1993).

As with the previous CMDs, data points were selected from within an initial region, shown in figure 3.4, which included GC candidates but excluded most contamination by field stars or background galaxies. These regions were

- $0.5 < (g-i)_0 < 1.4$ and $-11.35 < M_i < -8.35$ for NGC 5193,
- $0.25 < (g-i)_0 < 1.25$ and $-11.4 < M_i < -8.4$ for IC 4329, and
- $0.3 < (g-i)_0 < 1.2$ and $-11.3 < M_i < -8.3$ for NGC 3311.

We do not believe that colours are intrinsically different from galaxy to galaxy, but rather that the differences in limits are due to errors in the photometric zeropoints.

Using the points selected in these regions, the x-y distributions, GC colour versus radius, and radial densities were plotted, and are shown in figures 3.5, 3.6 and 3.7. Note that for the radial densities (figure 3.7), counts of the GCs fall off towards the centre of the galaxies. This is due to incompleteness. The background light was so high in the central regions that it was still not removed in the median subtraction process and GC detections could not be made here. This is shown in the lower left of the magnitude-radius plots in figure 3.8. All data points that were matched by DAOMASTER for NGC 5193 and IC 4329, and all the data points from Wehner et al. (2008a), are shown.

To check for bimodality, histograms for all three Gemini GCSs were plotted and are shown in figure 3.9. Wehner et al. (2008a) completed bimodal fits with both standard KMM ("Kaye's Mixture Modelling"; Ashman et al. 1994) algorithms and RMIX [2], finding that both mixture models returned similar values, but RMIX was more flexible in the choice of fitting functions and it returned values for some small samples where KMM did not. As such, we used RMIX here to fit the histograms. A bin size of $(g\text{-}i)$=0.045 was used for all three galaxies. Gaussians were used as the fitting distribution because this has been the trend in previous literature, and because there is no reason that we can think of to explain the presence of a skewed distribution. We therefore use the most likely of distributions: the Gaussian. One, two and three Gaussians were allowed, with the result that two Gaussians returned better reduced chi-

[2] RMIX is publicly available at http://www.math.mcmaster.ca/peter/mix/mix.html

squared values than one Gaussian. Three-Gaussian fits also gave no significant improvement to the fits.

The values returned by RMIX for each galaxy are shown in table 3.2. The columns in this table represent (1) the target's NGC or IC number, (2) the proportion of the subpopulation, (3) the error on the proportion, (4) the mean value of the Gaussian fitted to the subpopulation (i.e., the peak colour value), (5) the error on the mean, (6) the sigma, or distribution value, (7) the error on sigma (not applicable for the second subpopulation because the values of sigma for both subpopulations was forced to be equal [3]), (8) the degrees of freedom in the fit, (9) the χ^2 value, and (10) the reduced χ^2 value, found by dividing χ^2 by the degrees of freedom.

We note that the reduced χ^2 values for NGC 3311 are higher than expected. The bin size was varied to see how it affected the fit. The parameters returned for the fits with different bin sizes are shown in table 3.3. As can be seen, the fits are better when the bin size is smaller or larger than 0.045. We are unsure why this is so, but note that the values of the proportion and peak values of each subpopulation are approximately the same for bin sizes including and smaller than 0.045.

We also note that the colour difference in the peaks is approximately the same for all three (0.30, 0.31 and 0.29 for NGC 5193, IC 4329 and NGC 3311,

[3] For the GCSs with large numbers of GCs (i.e., NGC 3311), the subpopulations were found to be homoscedastic. However, as the statistics deteriorate, as with NGC 5193, the fits were more likely to be heteroscedastic. To avoid the possibility that the latter was just caused by low numbers of GCs, I forced all the spreads of the two subpopulations to be equal for all three galaxies.

respectively). However, the actual peak values are not. This is probably due to remaining zeropoint errors in the calibrations, as there were only a small number of calibration stars, so these results remain preliminary (see section 4.4). As can be seen in table 3.2, the values of sigma of the subpopulations across the galaxies are approximately the same.

3.2 Mass-Metallicity Relation

3.2.1 HST Data

Within the initial limits shown in figure 3.3, the data points were binned in magnitude bins of 0.3. The selection rule of the Chauvenet criteria (Parratt, 1961) was then applied, whereby data points were discarded if their value was greater than $z\sigma_{mean}$, where

$$z = 0.85(log_{10}n) + 1.12 \tag{3.6}$$

and n is the number of points in a bin. This further reduced the possibility of contamination by field stars.

The aim was then to get colour-magnitude slopes (i.e., $\Delta(B-I)/\Delta M_I$) with one for the blue GCs and another for the red. The data points that remained after the Chauvenet criteria had been applied were split using an initial line with a constant value of $(B\text{-}I)_0$=1.8 (the middle dashed line in figure 3.10). As noted in Peng et al. (2008), although the colour of the GCS bimodal peaks can vary with galaxy luminosity, the "dip" colour (the point at which the GC could be either red or blue) is relatively invariant. The axes of

these figures were switched (i.e., literally, the vertical axis was exchanged with the horizontal axis), both to allow a least-squares fit to be calculated and to compare with models (Rothberg et al 2008, in preparation). The data points were binned in 0.3 magnitude steps, with each bin being assigned a mean point. For each subpopulation, a weighted least-squares (WLSQ) fit was calculated with their respective mean values (the upper and lower dashed lines in Figure 3.10). A new dividing line half-way between these best fits was calculated (the middle solid line in the figures). This second iteration was done to prevent any bias that could occur in applying a constant value to the dividing line between the red and the blue subpopulations. The data points were split again - this time with the sloping line - and the data was then re-binned and fitted with a new WLSQ fit (the upper and solid lines in figure 3.10). The resulting best fit lines with their one sigma errors (calculated using SM[4]) were then overlaid on the original data points, as seen in the series of plots in figure 3.11.

There were two sets of data for NGC 4696. For each of the galaxies obtained from Harris et al. (2006) there are two associated data sets: one using aperture photometry, the other using PSF photometry. Harris et al. (2006) compare the two methods and conclude that they give extremely similar colour-magnitude distributions with the exception of NGC 4696. For that reason, just the aperture data is shown for seven galaxies, whereas for NGC 4696 both aperture and PSF photometry data sets are shown. NGC 5322 was also adjusted as it had one outlying mean value in one of the magnitude bins dissimilar from anything

[4] SM is an interactive plotting program by R. Lupton and P. Monger. More details can be found at http://www.astro.princeton.edu/ rhl/sm/sm.html.

else seen in the data. For this reason, this outlying mean value was excluded from the fit on grounds based similar to that of the Chauvenet criteria.

To explore what effect the brighter end of the globular cluster system had on the fitted slopes the brighter limit, originally at M_I>-10.5, was changed in increments of 0.3 magnitudes up to and including -11.7. Figure 3.12 shows one example of the different fits for the aperture data of NGC 4696. For some galaxies there were insufficient data points at such bright magnitudes so these galaxies had their brightest limit set at -11.1 or -11.4. For NGC 5322, the galaxy with the outlying mean value, a WLSQ fit was included for only nine bins, too, as this did not involve excluding the outlying mean value.

The value of each $\Delta(B-I)/\Delta M_I$ slope was plotted against the host galaxy luminosity, with one plot for the blue slopes and another for the red (see figure 3.13). The values for figure 3.13 are shown in table 3.4. For each GCS there were two sets of slopes - one for the red and one for the blue. Within each set, there are a number of slopes corresponding to the different number of bins used in the WLSQ fit. Obviously each slope from within the same set for one GCS should be plotted at the same luminosity, but we actually offset them from one another so that the variation with number of bins could be seen. In all cases, the fit for twelve bins used the exact host-galaxy luminosity. Figure 3.14 is similar to figure 3.13 with the exception that the values from each of the different number of magnitude bins has been averaged over within one GCS. The values for figure 3.14 are in table 3.5. Figure 3.15 then shows the error on the blue slope value as a function the number of GCs within the initial selection region.

3.2.2 Gemini Data

This data set is similarly processed as the HST data set, with binnings, Chauvenet criteria rejection and the two-stage dividing line. The inital dividing line was placed at the "dip" value of the RMIX fits (i.e., the point at which the GC could either be red or blue). We note that this dip colour or trend of invariance, noted by Peng et al. (2008) and first mentioned at the beginning of section 3.2.1, is seen for IC 4329 and NGC 3311 (with dip values of $(g\text{-}i)_0 =$ 0.78 and 0.80, respectively), but not for NGC 5193 (which has a dip value of $(g\text{-}i)_0 = 1.02$). NGC 5193's different dip value may be due to the low numbers of GCs in its system.

To enable a comparison between colour slopes in different colour systems, we need to convert the colour slopes to metallicity slopes (see section 3.2.3). However, there is currently no calibrated relationship between *(g-i)* and metallicity, so we use an indirect method of first converting *(g-i)* to *(B-I)*. We note that this introduces more uncertainty into the final values for the metallicity slope.

To convert *(g-i)* slope values to *(B-I)* slope values, the relationship seen in figure 3.16 was used: more specifically, where the relation appears linear for $1.2 < (B\text{-}I) < 2.6$. The observational data points of standard stars are shown, with a short dashed line, with a single-star population model from Maraston (2005). The linear conversion calculated was

$$\Delta(B-I) = \frac{\Delta(g-i)}{(0.53 \pm 0.12)} \tag{3.7}$$

which is shown as the long straight solid line in the figure, with the errors shown by long straight dashed lines. This conversion makes the errors for the

Gemini GCS slopes larger when the values are in *(B-I)*, as can be seen in figures 3.13 and 3.15, and table 3.4(c).

3.2.3 Comparisons to Other Data

Using *HST* ACS photometry, Mieske et al. (2006b) looked at 79 early-type galaxies from the ACS Virgo Cluster Survey. Their results were split into four magnitude bins. As the colours used were *(g_{475}-z_{850})*, all colours - both those of Mieske et al. (2006b) and the ones from *HST* and Gemini data in this study - needed to be converted to metallicity so that a standard comparison could be made. The colour-magnitude slopes are converted to mass-metallicity relations of the form $Z = M^p$ (see section 5.3).

We derive mass-metallicity relations for each of the slopes by using equations 3.8, 3.9 and 3.10, as shown in appendix section 5.3. Equation 3.8 is a linear relation from Harris et al. (2006), and is based on *(B-I)* colours and metallicities for Galactic GCs.

$$\frac{\Delta(B-I)_0}{\Delta[\mathrm{Fe/H}]} = 0.375 \pm 0.049 \tag{3.8}$$

Mieske et al. (2006b) use the colour-metallicity conversions from Peng et al. (2006). Peng et al. (2006) base their relations not only on GCs in the Galaxy but also in M87 and NGC 4472. They find a piecewise relation for the *(g-z)* colour, with equation 3.9 for the colour range $0.70<(g_{475}\text{-}z_{850})\leqslant 1.05$ and equation 3.10 for the colour range $1.05<(g_{475}\text{-}z_{850})<1.45$.

$$\frac{\Delta(g_{475}-z_{850})}{\Delta[\mathrm{Fe/H}]} = 0.195 \pm 0.025 \tag{3.9}$$

$$\frac{\Delta(g_{475} - z_{850})}{\Delta[\mathrm{Fe/H}]} = 0.546 \pm 0.069 \tag{3.10}$$

Figures 3.17 and 3.18 show the metallicity slopes versus the host galaxy luminosity. Each of the Mieske et al. (2006b) magnitude bins has two data points associated with it - one set is shown as triangles and the other set as squares. Triangles correspond to *(g-z)* versus g; squares to *(g-z)* versus z. Mieske et al. (2006b) show that because the blue subpopulation extends to higher luminosities than the red, the resulting KMM fits are biased. Tests with artificial CMDs show that the effect seen with g-z versus z is real, therefore we only consider these (square) data points from here on in.

Table 3.1: Galaxies; Their Details and Photometry Sources

NGC or IC	Cluster or Group	Redshift cz (km s^{-1})	M_V^T	$E(B-I)$	$(m-M)_I$	Number of data points	N_{GC}	S_N
(1)	(2)	(3)[a]	(4)	(5)[a]	(6)[b]	(7)[c]	(8)	(9)
(B, I) photometry from ACS/WFC								
NGC 1407	Eridanus	1627	-22.35	0.16	31.96	1046	3983	1.63
NGC 5322	CfA 122	1916	-22.01	0.03	32.22	395	1583	0.60
NGC 7049	N7049	1977	-21.76	0.12	32.36	682	2717	1.09
NGC 3348	CfA 69	2837	-22.13	0.17	33.18	831	3149	1.30
NGC 3258	Antlia	3129	-21.87	0.20	33.23	1812	6928	2.89
NGC 3268	Antlia	3084	-21.96	0.24	33.27	1593	6017	2.57
NGC 4696	Cen 30	2926	-23.31	0.23	33.29	3099	11713	5.06
NGC 5557	CfA 141	3213	-22.32	0.01	33.31	841	3478	1.31
NGC 7626	Pegasus (I)	3154	-22.31	0.17	33.32	1835	6874	2.82
B photometry from ACS/WFC, *I* from WFPC2								
NGC 708	Abell 262	4633	-22.07	0.21	34.26	1282	4828	2.02
NGC 7014	Abell 3742	4736	-21.78	0.08	34.12	962	3779	1.47
IC 4296	Abell 3565	3959	-23.28	0.15	33.79	885	3576	1.45
(g, i) photometry from GMOS								
NGC 5193	Abell 3565[d]	3959	-22.40	0.11	33.87	596	1006	1.41
IC 4329	Abell 3574[e]	5066	-23.20	0.12	34.42	1528	2300	3.81
NGC 3311	Abell 1060	4121	-22.46	0.15	34.02	4936	7484	11.46

[a] Values were taken from NED

[b] Values calculated using an adopted value of $H_0 = 70$ km s^{-1} Mpc^{-1}.

[c] Points in the initial selection regions as detailed in sections 3.1.1 and 3.1.2

[d,e] See discussion in section 3.1.2

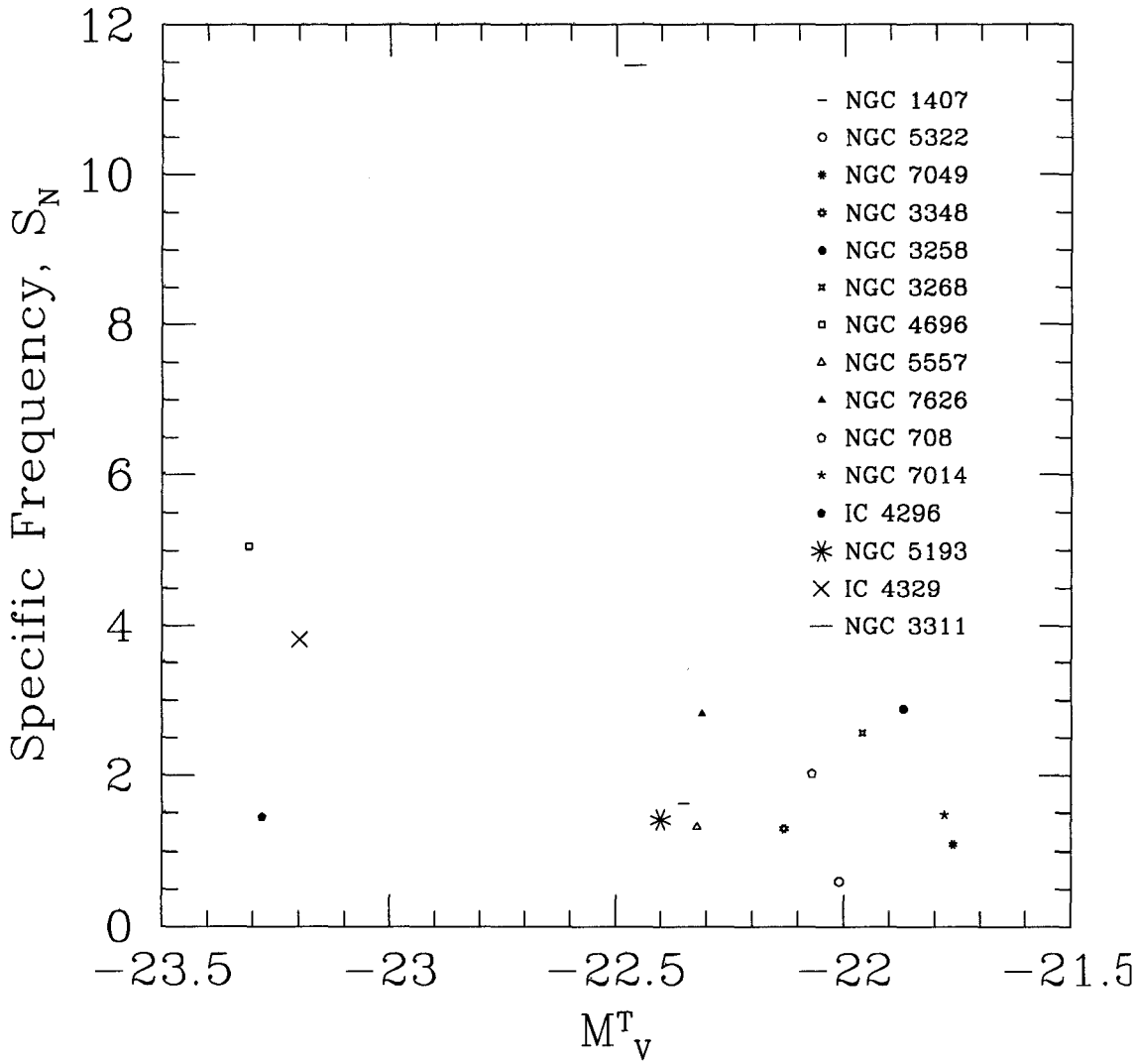

Figure 3.1: Specific frequency of GCs versus host-galaxy luminosity

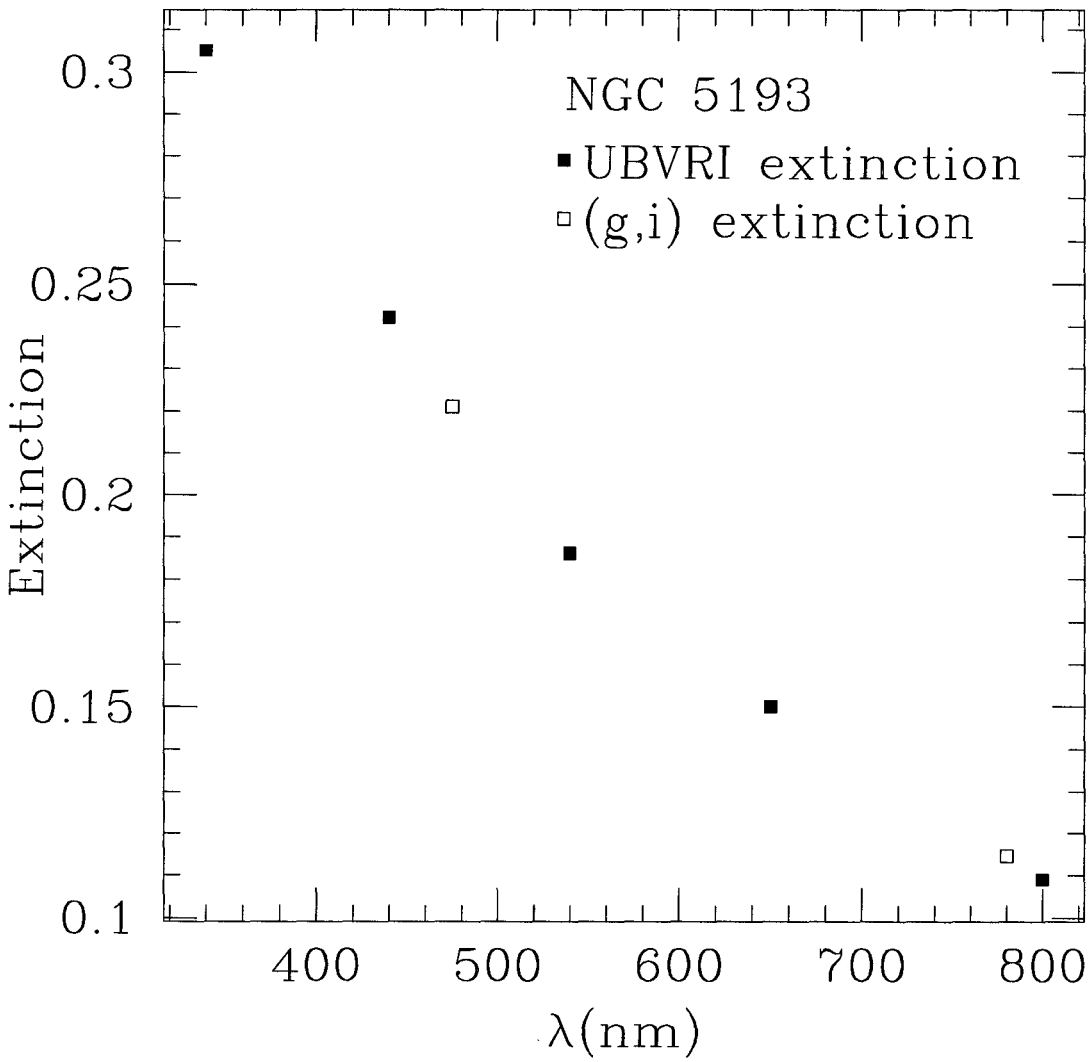

Figure 3.2: NGC 5193 Extinction

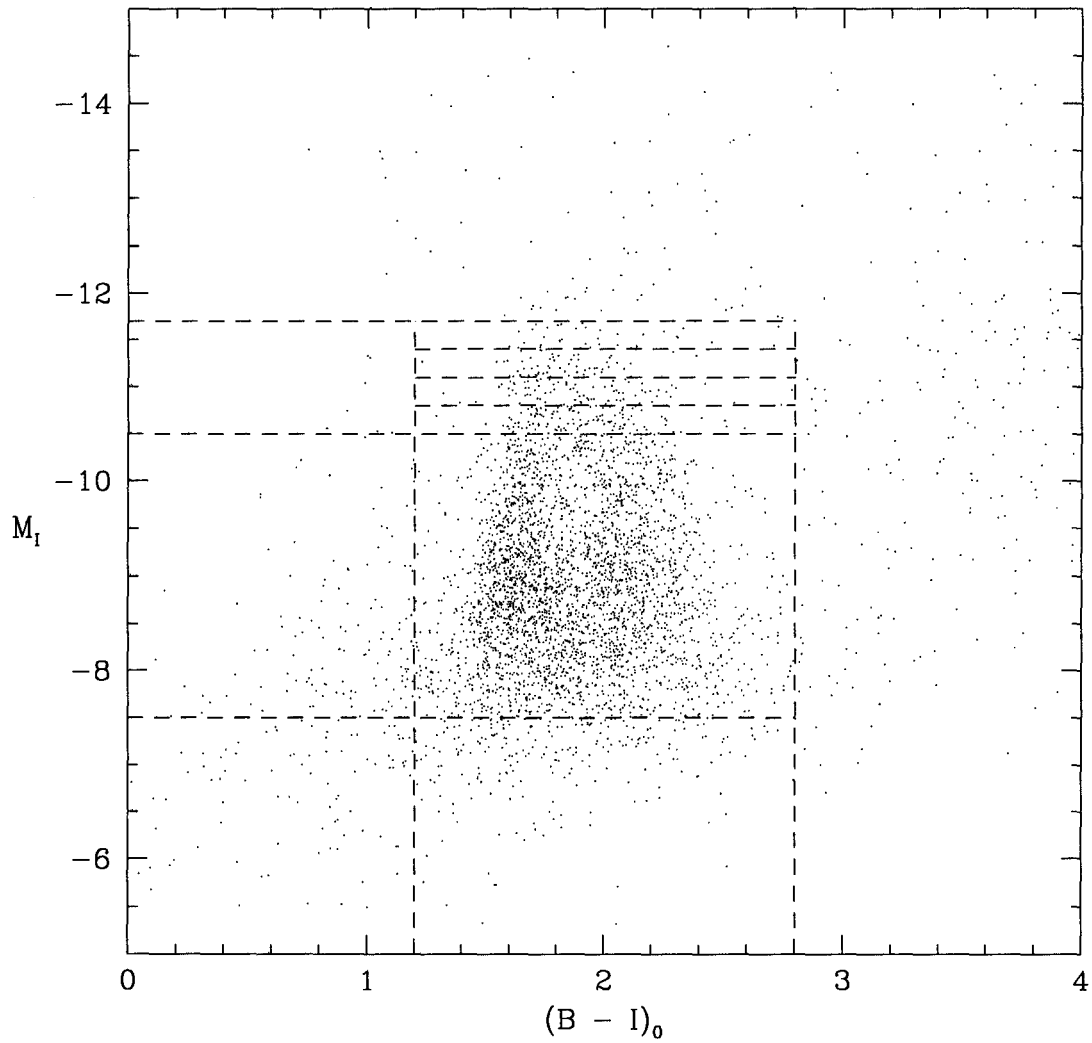

Figure 3.3: A colour-magnitude diagram for the GCS of NGC 4696. The initial limits of $1.2<(B\text{-}I)_0<2.8$ and $-10.5<M_I<-7.5$ used in the analysis of the blue-MMR are shown by the central box. Also shown are the incremental increases of the brighter limit of this box in 0.3 magnitude steps up to $M_I>-11.7$.

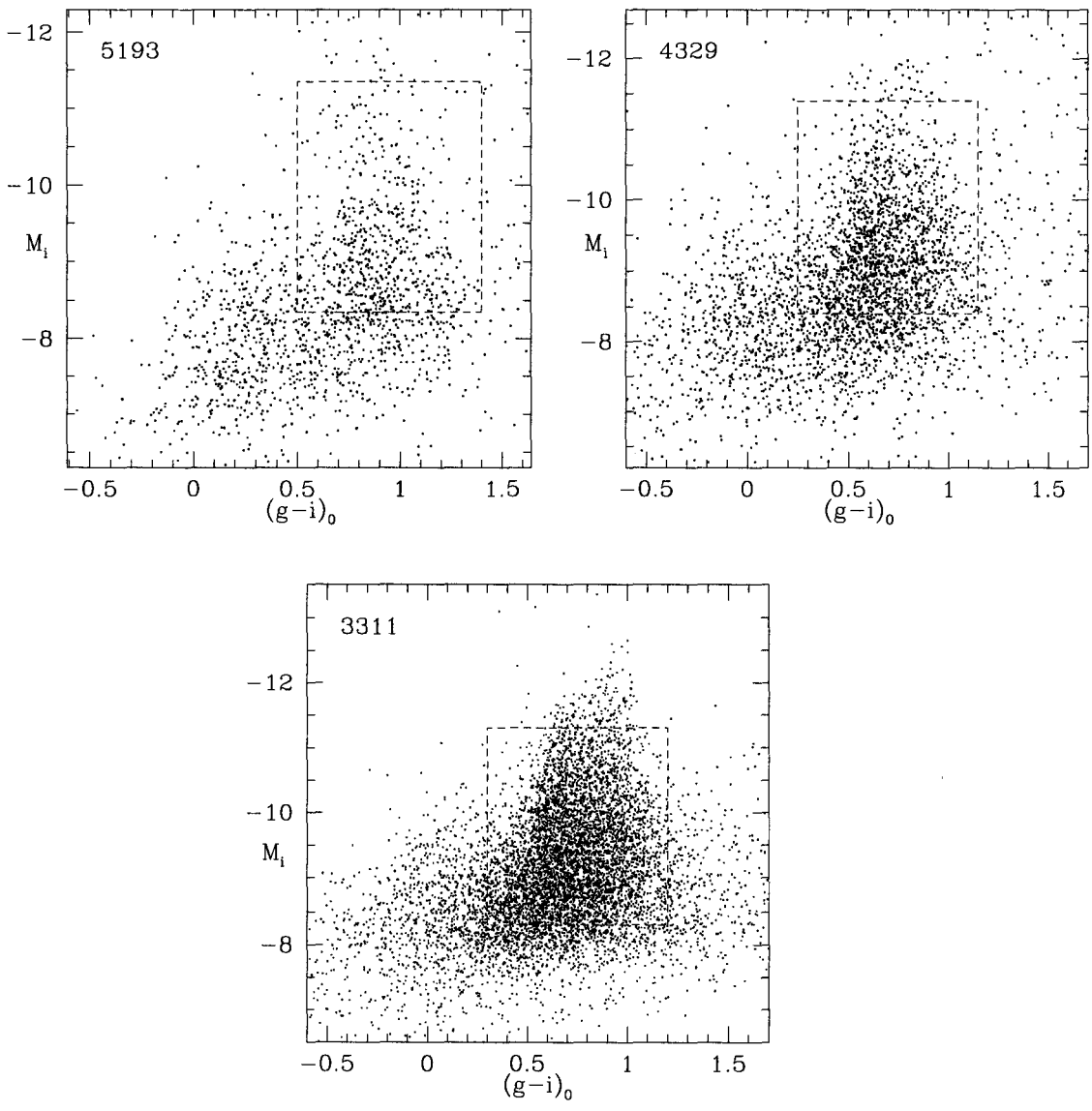

Figure 3.4: CMDs for NGC 5193, IC 4329 and NGC 3311 with the area for GC candidates marked. As with figure 3.3, the brightest limit of the box was incrementally increased in 0.3 magnitude steps.

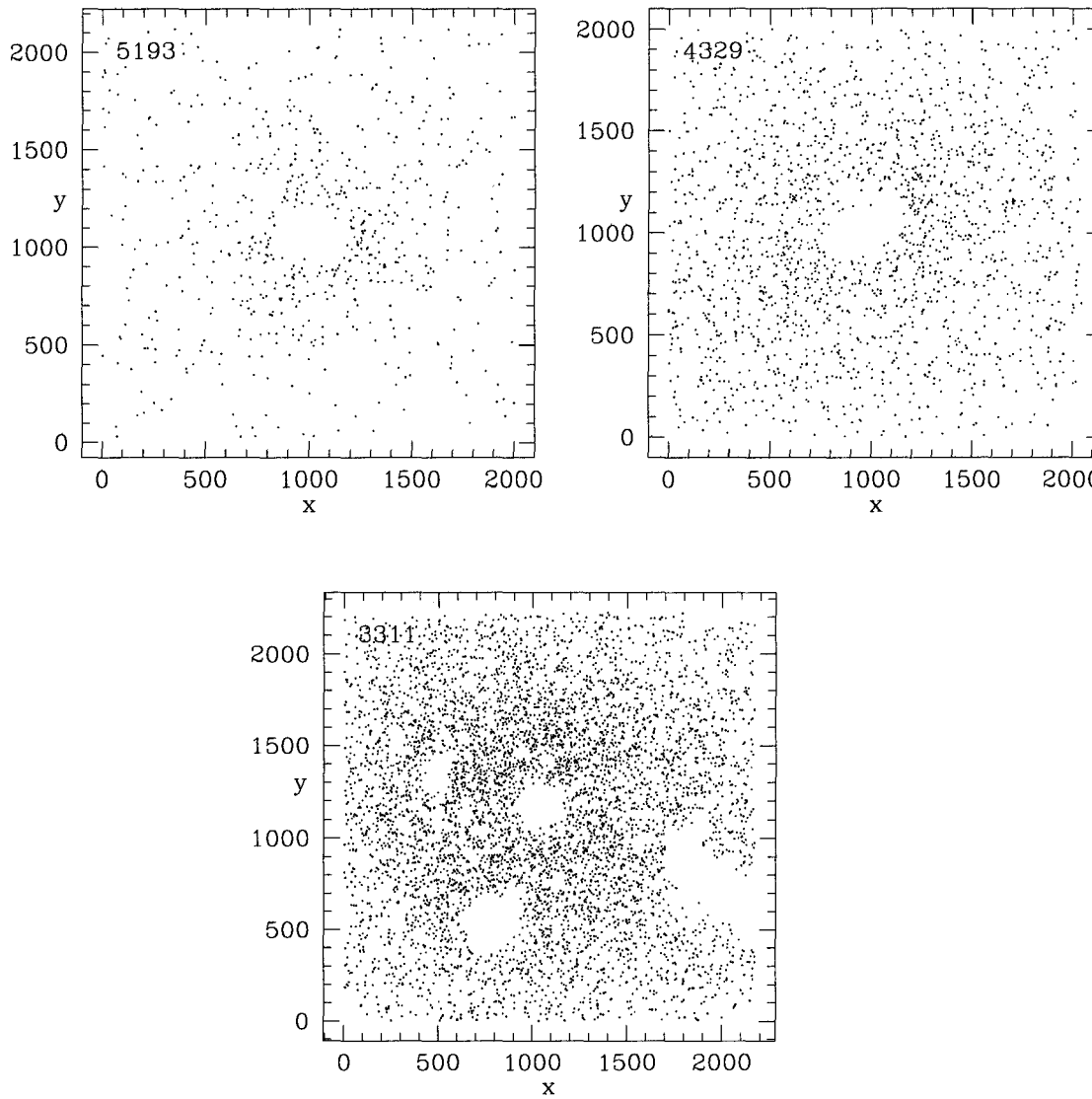

Figure 3.5: Mapping the positions of objects on a physical scale within the GC candidate regions - as shown in figure 3.4 - for the three galaxies.

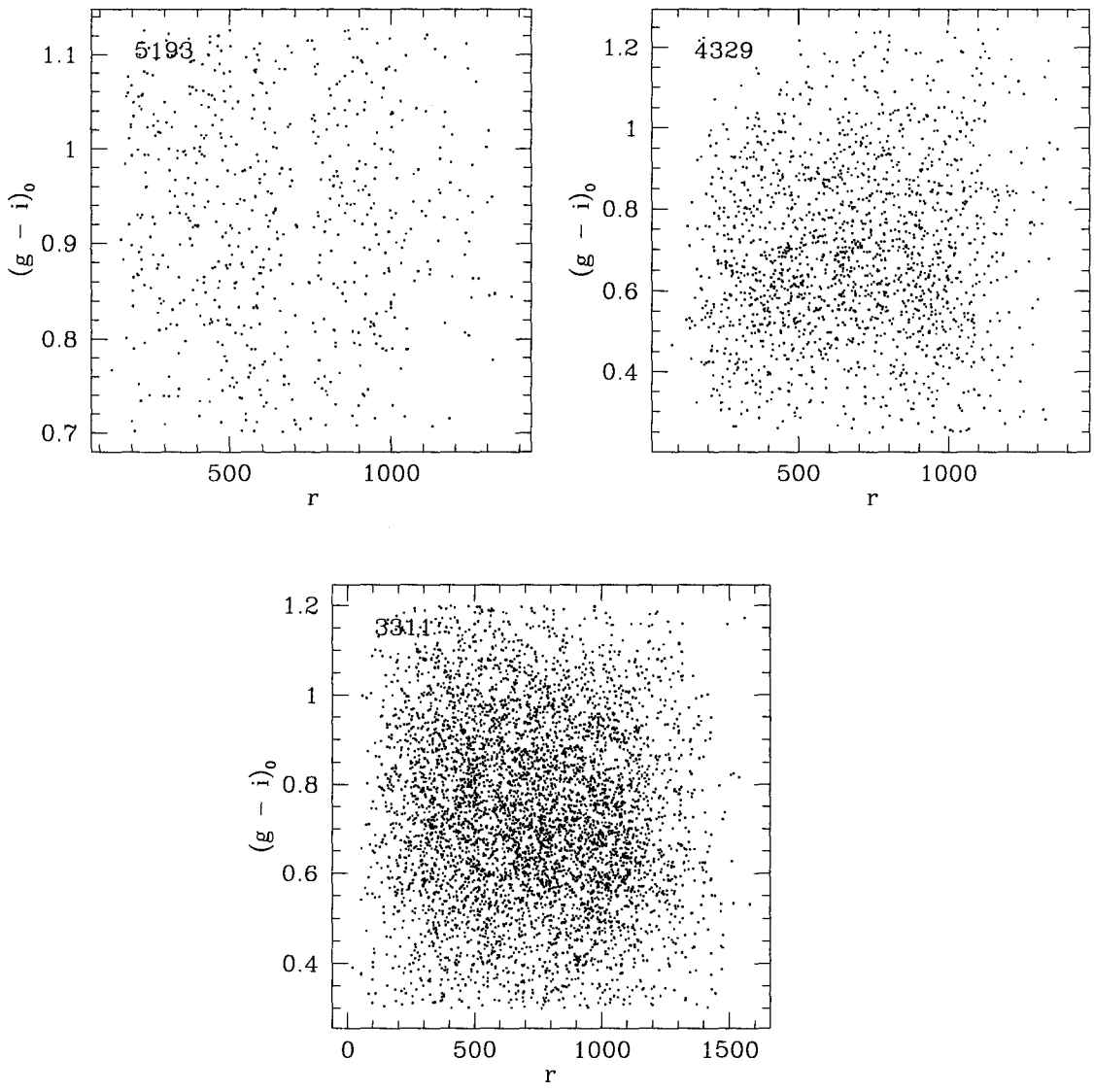

Figure 3.6: Colour versus radius for objects within the GC candidate regions - as shown in figure 3.4.

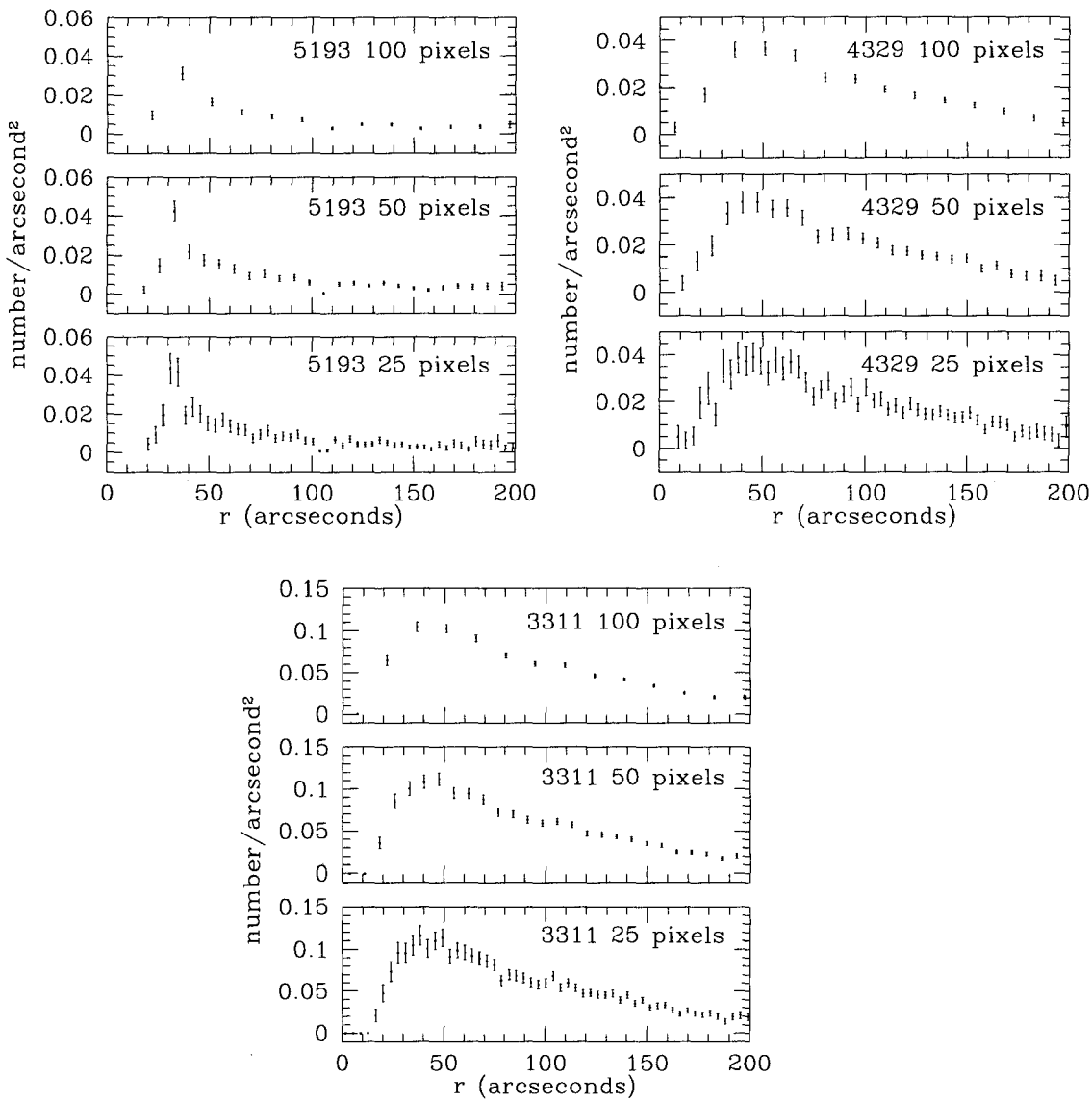

Figure 3.7: Number of GC candidates per unit area on the sky as a function of radius from the centre of the respective galaxy. 25, 50 and 100 pixels refer to the width of the radial bin, and correspond to a radius on the sky of 3.65, 7.3 and 14.6 arcseconds, respectively. Errors are shown as the square root of the number of GC candidates, divided by the area.

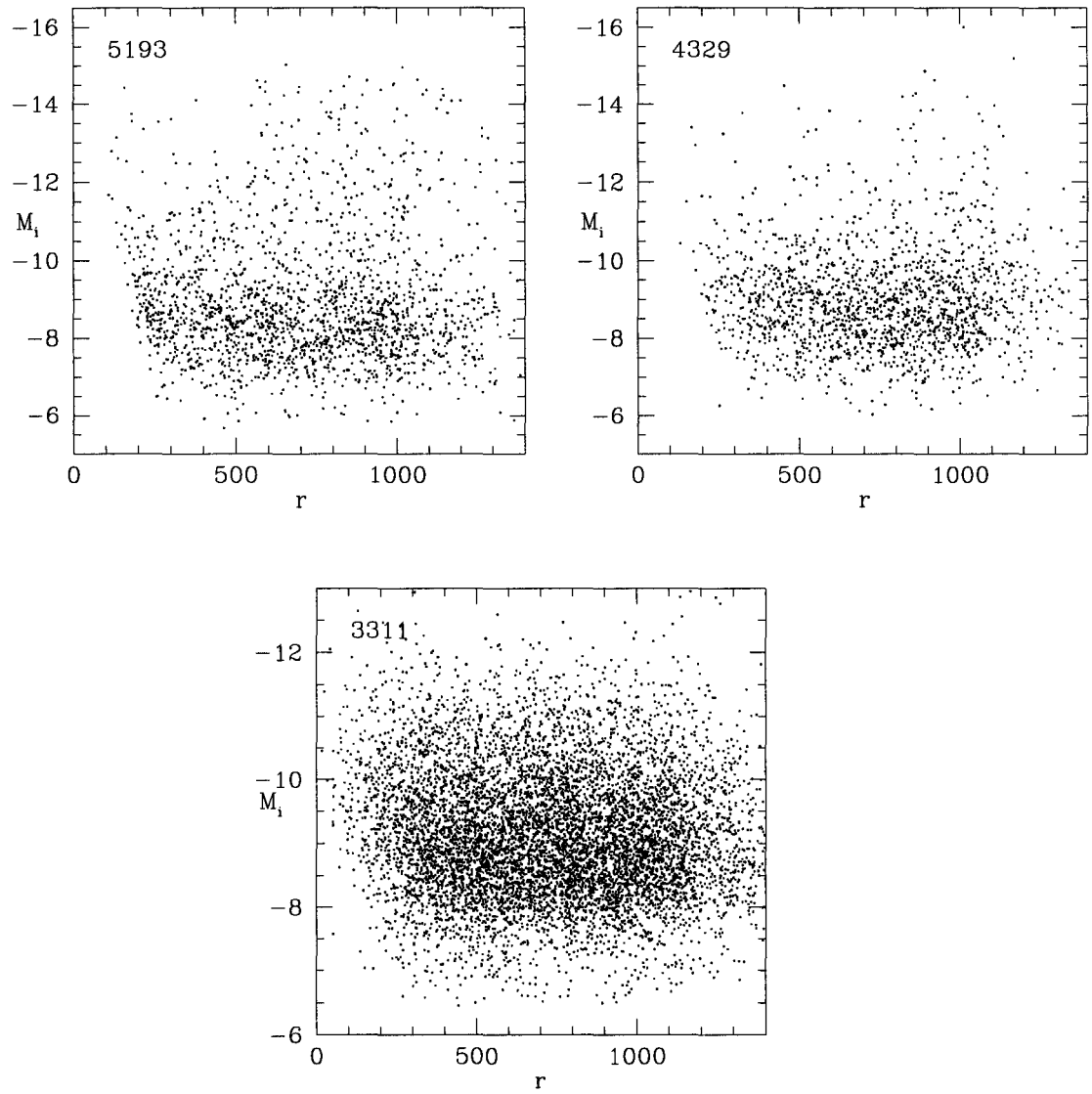

Figure 3.8: Absolute magnitude versus radius from central galaxy for GC candidates. This figure shows the effects of the high background light towards the centre of the galaxy, as there are a lack of fainter objects at small radii (i.e., in the bottom left-hand corner of the diagrams).

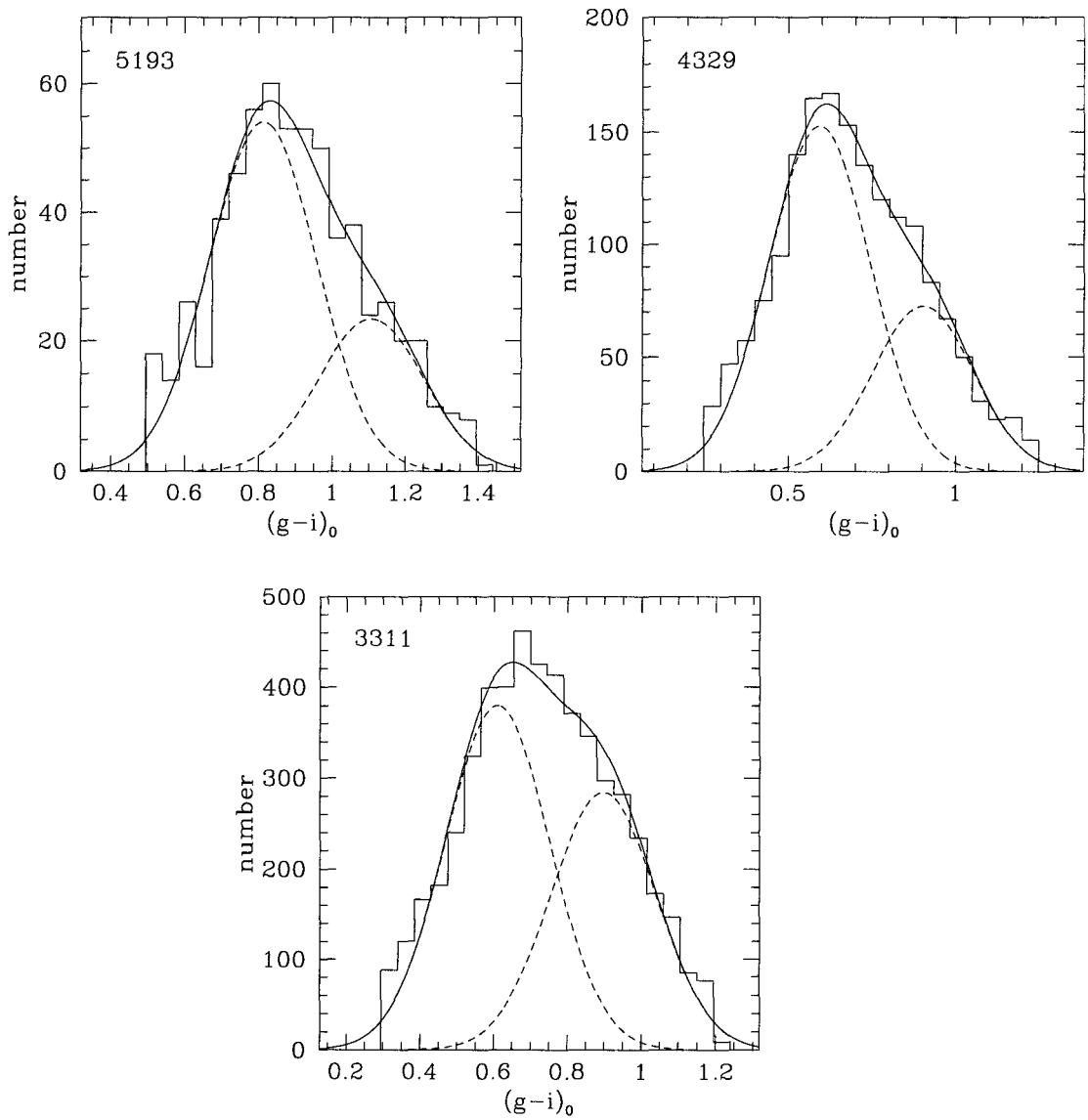

Figure 3.9: Histograms showing the RMIX fits for bimodal distributions.

Table 3.2: RMIX Parameters for NGCs 5193 and 3311, and IC 4329. See section 3.1.2 for further details of column contents.

Target	Pi	Error	Mean	Error	Sigma	Error	DOF	χ^2	Reduced χ^2	pr(>chisq)
(1)	(2)	(3)	(4)	(5)	(6)	(7)	(8)	(9)	(10)	(11)
NGC 5193	0.698	0.046	0.812	0.013	0.1444	0.0073	19	46.08	2.42	$2.2\text{x}10^{-16}$
	0.302	0.046	1.107	0.022	0.1444	NA				
IC 4329	0.678	0.028	0.5923	0.0088	0.1503	0.0048	18	69.82	3.88	4.83^{-4}
	0.322	0.028	0.903	0.013	0.1503	NA				
NGC 3311	0.572	0.016	0.6101	0.0051	0.1416	0.0025	19	220.68	11.61	$4.84\text{x}10^{-8}$
	0.428	0.016	0.8978	0.0061	0.1416	NA				

Table 3.3: RMIX Parameters for NGC 3311 with Varying Bin Size. See section 3.1.2 for further details of column contents.

Bin Size	Pi	Error	Mean	Error	Sigma	Error	DOF	χ^2	Reduced χ^2	pr(>chisq)
(1)	(2)	(3)	(4)	(5)	(6)	(7)	(8)	(9)	(10)	(11)
0.18	0.557	0.024	0.5191	0.0073	0.1536	0.0043	3	18.92	6.31	$2.84\text{x}10^{-4}$
	0.444	0.024	0.7934	0.0094	0.1536	NA				
0.09	0.578	0.018	0.5670	0.0056	0.1461	0.0029	8	77.97	9.75	$1.25\text{x}10^{-13}$
	0.422	0.018	0.8515	0.0068	0.1461	NA				
0.045	0.572	0.016	0.6101	0.0051	0.1416	0.0025	19	220.68	11.61	$4.84\text{x}10^{-8}$
	0.428	0.016	0.8978	0.0061	0.1416	NA				
0.0225	0.574	0.016	0.5983	0.0049	0.1414	0.0025	42	250.68	5.97	$2.2\text{x}10^{-16}$
	0.426	0.016	0.8820	0.0059	0.1414	NA				
0.01125	0.579	0.016	0.6058	0.0049	0.1417	0.0025	88	312.79	3.55	$2.2\text{x}10^{-16}$
	0.421	0.016	0.8943	0.0060	0.1417	NA				
0.005625	0.578	0.016	0.6085	0.0049	0.1418	0.0025	180	485.36	2.70	$2.2\text{x}10^{-16}$
	0.422	0.016	0.8967	0.0060	0.1418	NA				
0.0028125	0.578	0.016	0.6097	0.0049	0.1417	0.0025	364	678.9	1.87	$2.2\text{x}10^{-16}$
	0.422	0.016	0.8980	0.0060	0.1417	NA				

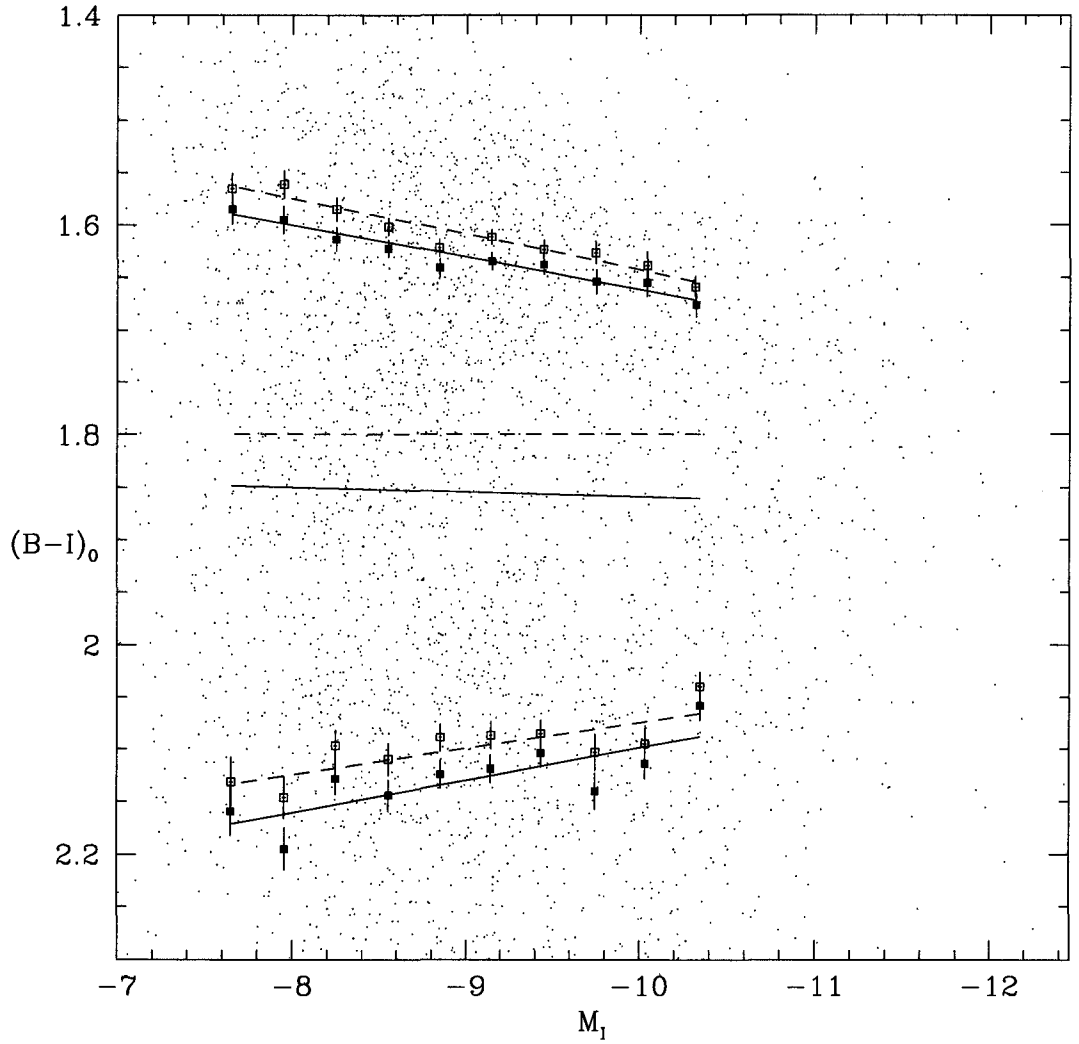

Figure 3.10: A CMD for NGC 4696, with an example of initial constant dividing line with a value of $(B\text{-}I)_0$=1.8 (the middle dashed line) and then a subsequent sloping dividing line (the middle solid line).

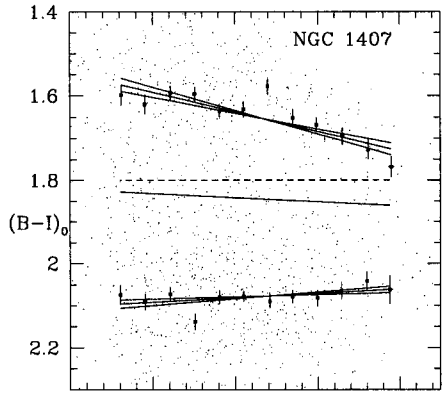
NGC 1407
1.4
1.6
1.8
(B−I)0
2
2.2

(a)

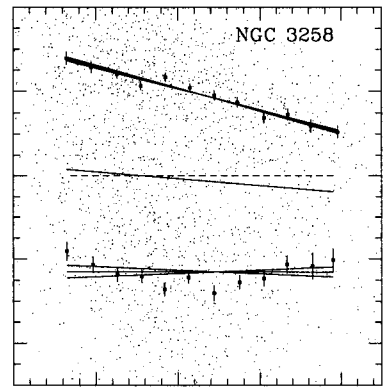
NGC 3258

(b)

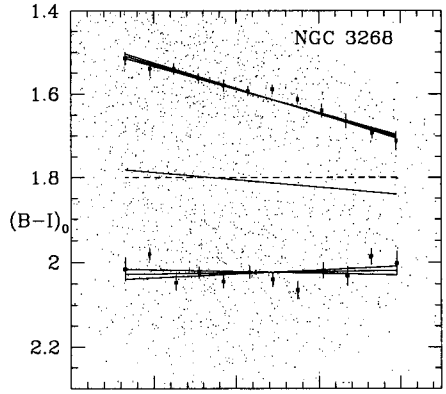
NGC 3268
1.4
1.6
1.8
(B−I)0
2
2.2

(c)

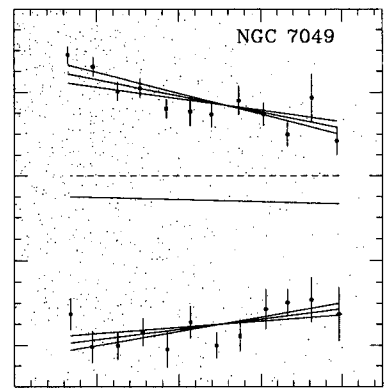
NGC 7049

(d)

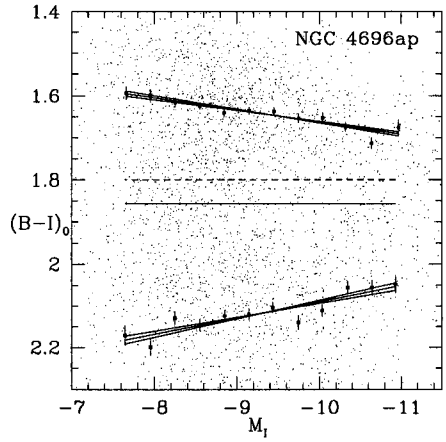
NGC 4696ap
1.4
1.6
1.8
(B−I)0
2
2.2
−7
−8
−9
−10
−11
MI

(e)

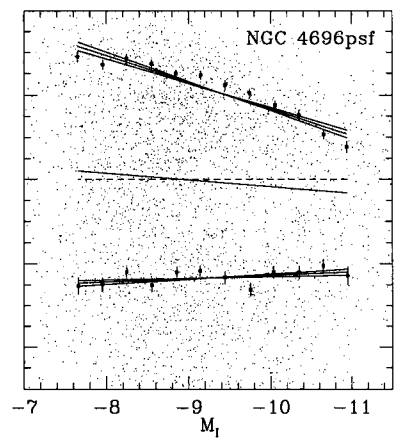
NGC 4696psf
−7
−8
−9
−10
−11
MI

(f)

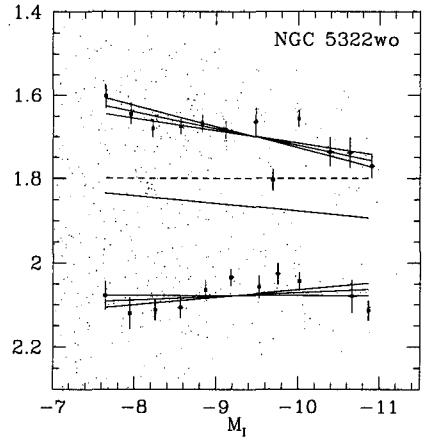
NGC 5322wo
1.4
1.6
1.8
2
2.2
−7
−8
−9
−10
−11
M_I

(g)

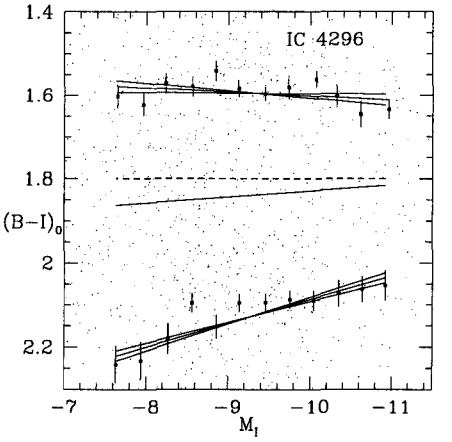
IC 4296
1.4
1.6
1.8
(B−I)_0
2
2.2
−7
−8
−9
−10
−11
M_I

(h)

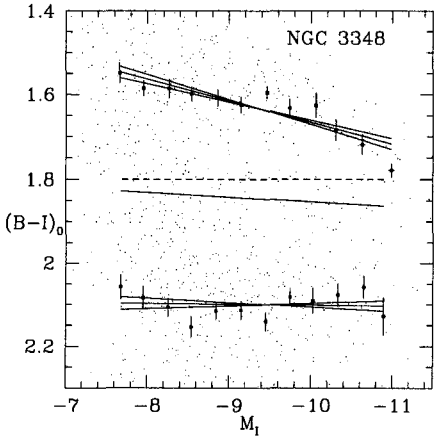
NGC 3348
1.4
1.6
1.8
(B−I)_0
2
2.2
−7
−8
−9
−10
−11
M_I

(i)

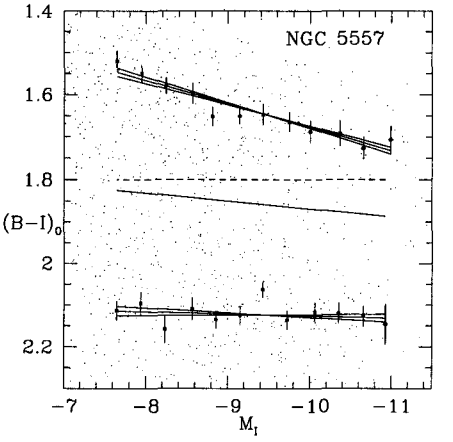
NGC 5557
1.4
1.6
1.8
(B−I)_0
2
2.2
−7
−8
−9
−10
−11
M_I

(j)

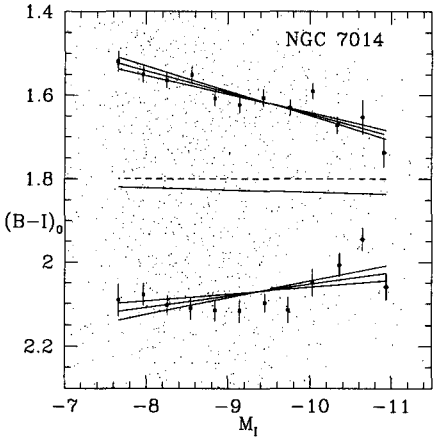
NGC 7014
1.4
1.6
1.8
(B−I)_0
2
2.2
−7
−8
−9
−10
−11
M_I

(k)

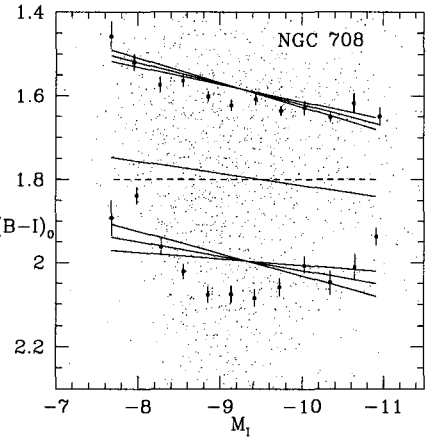
NGC 708
1.4
1.6
1.8
(B−I)_0
2
2.2
−7
−8
−9
−10
−11
M_I

(l)

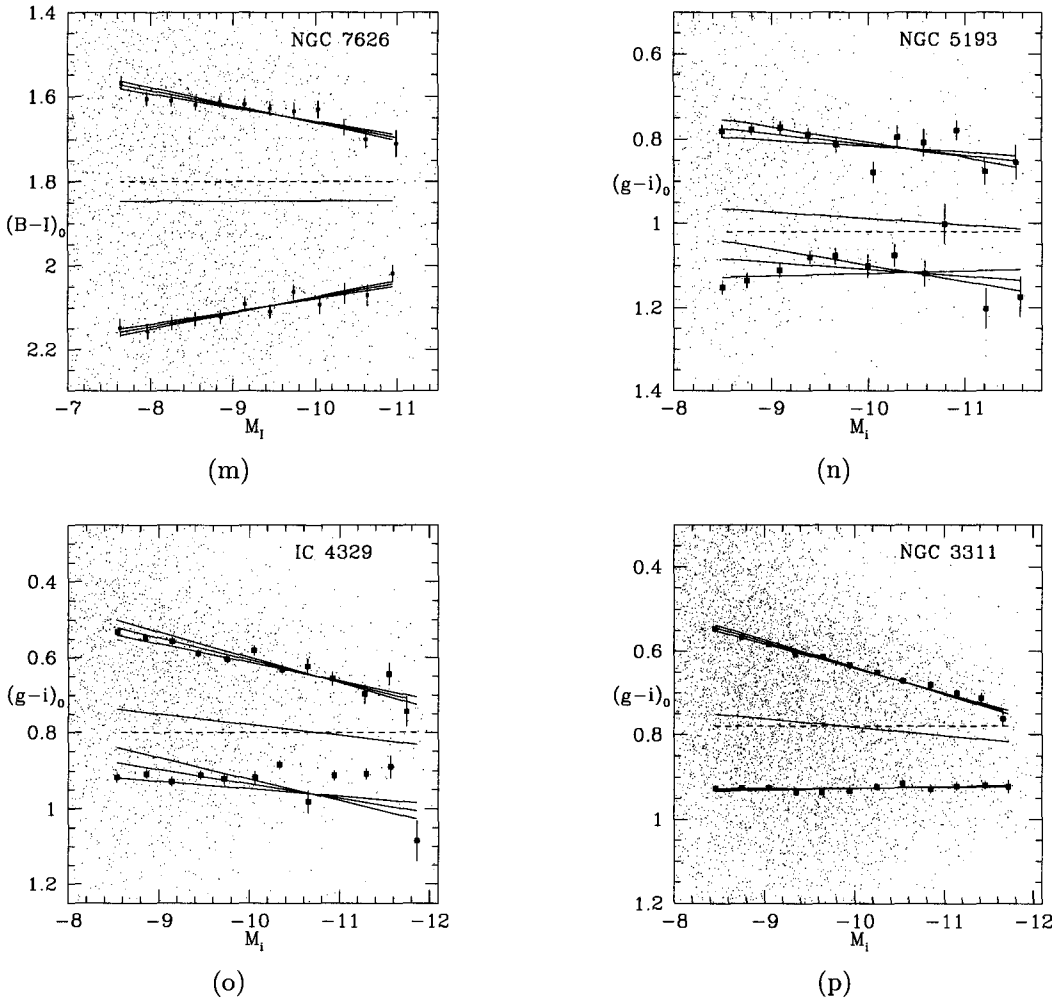

Figure 3.11: Best-fit lines for the blue and red subpopulations for all fifteen GCSs

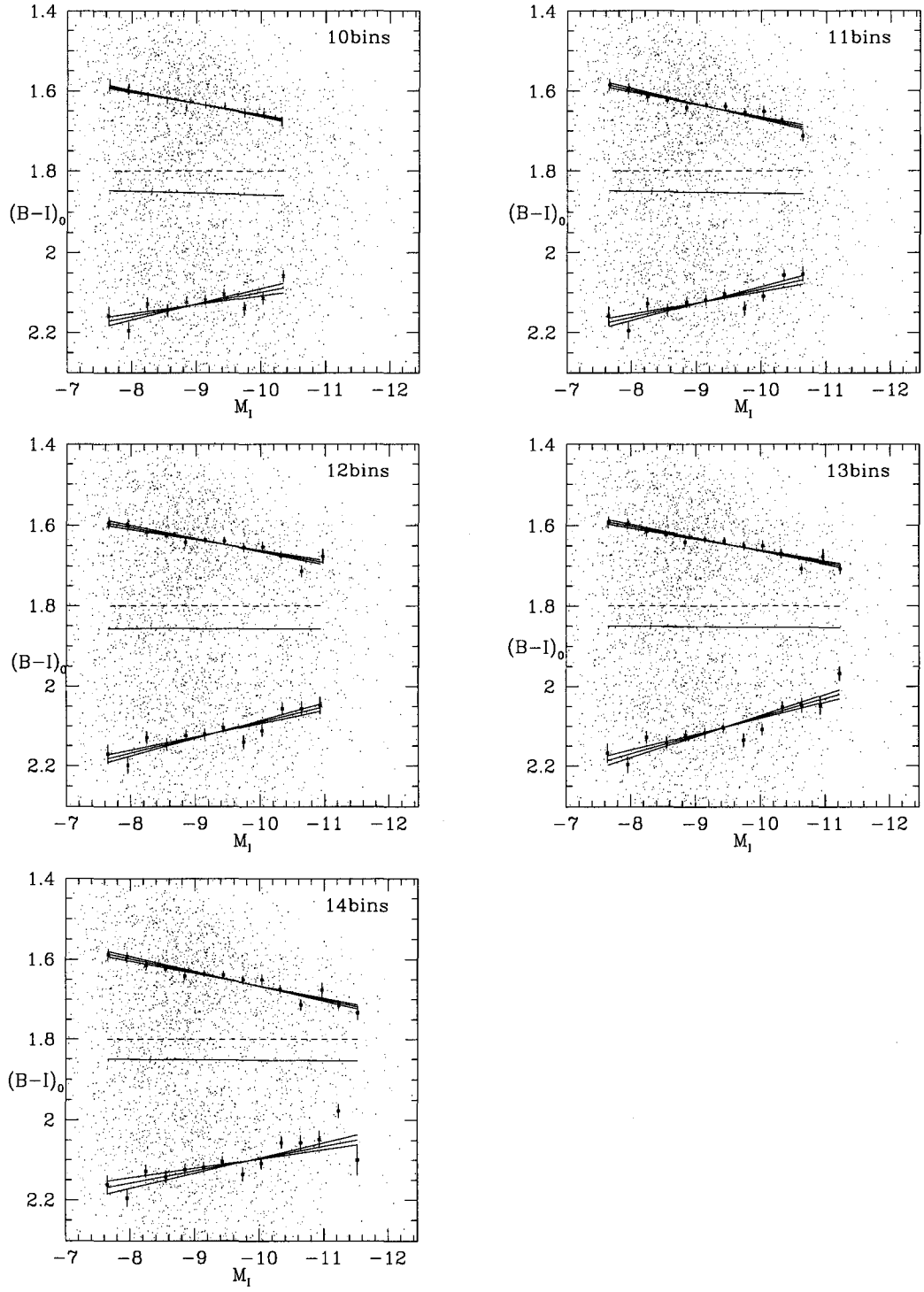

Figure 3.12: Showing different bins for NGC 4696ap

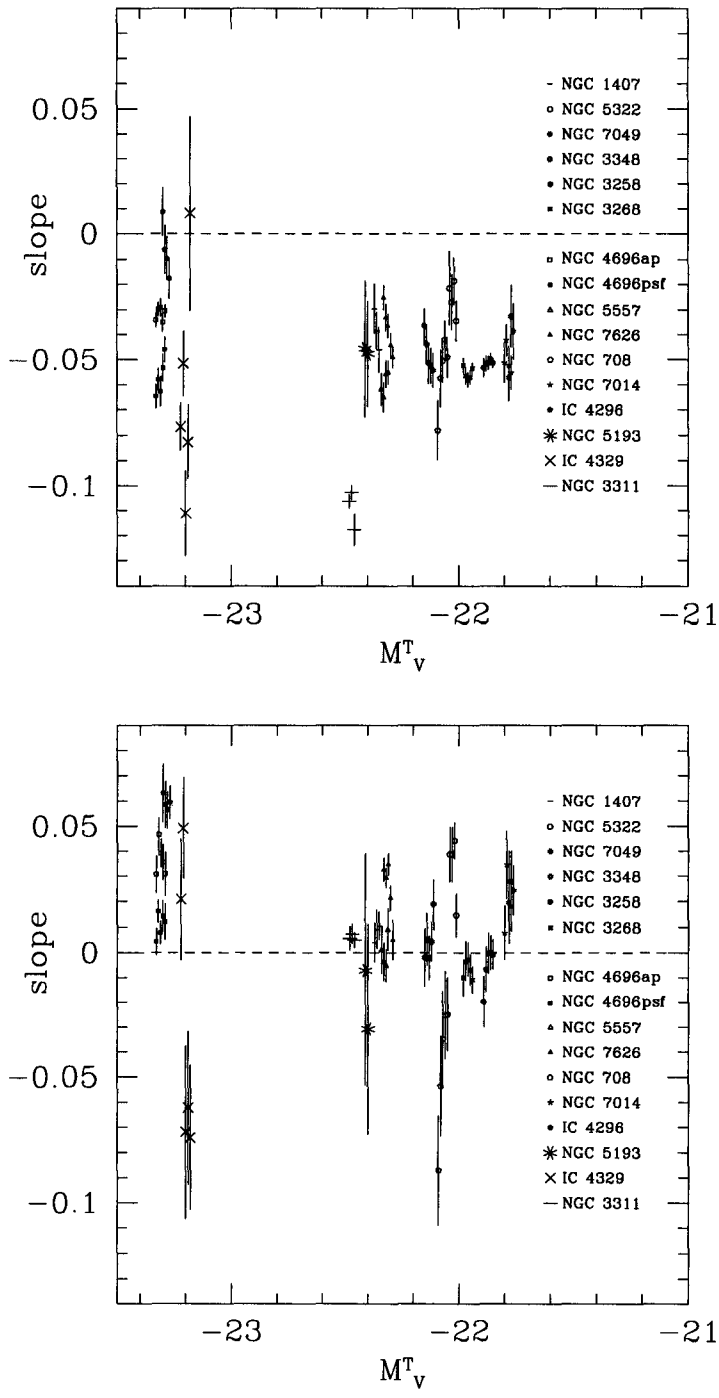

Figure 3.13: Blue (above) and red (below) colour slopes versus host galaxy luminosity with all bins

Table 3.4: Blue and red slopes with corresponding p values for all bins, where p is defined in the relation $Z = M^p$ (see section 5.3).

(a)

NGC or IC (1)	Number of bins (7)	Blue Slope (8)	Blue Slope Error (9)	p (10)	Error on p (11)	Red Slope (12)	Red Slope Error (13)	p (14)	Error on p (15)
(B, I) photometry from ACS/WFC									
NGC 1407	10	-0.0296	0.0099	0.20	0.23	0.0041	0.0076	-0.03	0.14
NGC 1407	11	-0.0384	0.0075	0.26	0.21	0.0093	0.0075	-0.06	0.14
NGC 1407	12	-0.0460	0.0090	0.31	0.25	0.0105	0.0054	-0.07	0.11
NGC 5322	9	-0.021	0.015	0.14	0.29	0.039	0.011	-0.26	0.27
NGC 5322	10	-0.027	0.011	0.18	0.24	0.039	0.011	-0.26	0.27
NGC 5322	11	-0.0186	0.0093	0.12	0.20	0.0441	0.0073	-0.29	0.22
NGC 5322	12	-0.0345	0.0081	0.23	0.21	0.0147	0.0084	-0.10	0.17
NGC 7049	10	-0.0573	0.0092	0.38	0.28	0.020	0.016	-0.13	0.30
NGC 7049	11	-0.033	0.012	0.22	0.28	0.028	0.012	-0.19	0.26
NGC 7049	12	-0.039	0.011	0.26	0.27	0.0244	0.0097	-0.16	0.21
NGC 3348	10	-0.0363	0.0066	0.24	0.19	-0.002	0.011	0.01	0.19
NGC 3348	11	-0.0438	0.0072	0.29	0.21	0.005	0.010	-0.03	0.18
NGC 3348	12	-0.0515	0.0081	0.34	0.25	-0.021	0.0087	0.01	0.15
NGC 3348	13	-0.0526	0.0070	0.35	0.23	0.0043	0.0076	-0.03	0.14
NGC 3348	14	-0.0544	0.0069	0.36	0.23	0.0189	0.0098	-0.13	0.20
NGC 3258	10	-0.0534	0.0037	0.36	0.18	-0.020	0.010	0.13	0.21
NGC 3258	11	-0.0518	0.0030	0.35	0.16	-0.0067	0.0090	0.04	0.16
NGC 3258	12	-0.0515	0.0026	0.34	0.16	-0.0003	0.0081	0.002	0.135
NGC 3258	13	-0.0499	0.0023	0.33	0.15	-0.0001	0.0068	0.001	0.113
NGC 3258	14	-0.0514	0.0019	0.34	0.14	-0.0007	0.0057	0.005	0.097
NGC 3268	10	-0.0523	0.0029	0.35	0.16	-0.0100	0.0073	0.07	0.14
NGC 3268	11	-0.0565	0.0031	0.38	0.18	-0.0034	0.0078	0.02	0.14
NGC 3268	12	-0.0581	0.0029	0.39	0.18	-0.0026	0.0066	0.02	0.12
NGC 3268	13	-0.0571	0.0027	0.38	0.17	-0.0069	0.0061	0.05	0.12
NGC 3268	14	-0.0536	0.0023	0.36	0.16	-0.0108	0.0053	0.07	0.11
NGC 4696ap	10	-0.0305	0.0025	0.20	0.11	0.0309	0.0086	-0.21	0.21
NGC 4696ap	11	-0.0350	0.0037	0.23	0.14	0.0355	0.0071	-0.24	0.20
NGC 4696ap	12	-0.0291	0.0035	0.19	0.12	0.0391	0.0056	-0.26	0.18
NGC 4696ap	13	-0.0298	0.0028	0.20	0.11	0.0467	0.0065	-0.31	0.21
NGC 4696ap	14	-0.0340	0.0030	0.23	0.12	0.0307	0.0074	-0.20	0.19
NGC 4696psf	10	-0.0461	0.0050	0.31	0.18	0.0121	0.0070	-0.08	0.14
NGC 4696psf	11	-0.0534	0.0055	0.36	0.21	0.0142	0.0061	-0.09	0.13
NGC 4696psf	12	-0.0628	0.0059	0.42	0.24	0.0079	0.0044	-0.053	0.090
NGC 4696psf	13	-0.0581	0.0045	0.39	0.20	0.0161	0.0043	-0.11	0.11
NGC 4696psf	14	-0.0647	0.0048	0.43	0.22	0.0044	0.0053	-0.029	0.098
NGC 5557	10	-0.0620	0.0064	0.41	0.24	0.0011	0.0093	-0.01	0.16
NGC 5557	11	-0.0651	0.0059	0.43	0.24	-0.0036	0.0075	0.02	0.13
NGC 5557	12	-0.0558	0.0054	0.37	0.21	-0.0051	0.0063	0.03	0.12
NGC 5557	13	-0.0552	0.0045	0.37	0.20	0.0091	0.0081	-0.06	0.15
NGC 7626	10	-0.0251	0.0047	0.17	0.13	0.0326	0.0047	-0.22	0.15
NGC 7626	11	-0.0331	0.0054	0.22	0.16	0.0294	0.0038	-0.20	0.13
NGC 7626	12	-0.0364	0.0047	0.24	0.16	0.0347	0.0043	-0.23	0.15
NGC 7626	13	-0.0443	0.0048	0.30	0.18	0.0214	0.0049	-0.14	0.13
NGC 7626	14	-0.0490	0.0042	0.33	0.18	0.0051	0.0078	-0.03	0.14

(b)

NGC or IC (1)	Number of bins (7)	Blue Slope (8)	Blue Slope Error (9)	p (10)	Error on p (11)	Red Slope (12)	Red Slope Error (13)	p (14)	Error on p (15)
B photometry from ACS/WFC, I from WFPC2									
NGC 708	10	-0.078	0.012	0.52	0.36	-0.087	0.022	0.58	0.55
NGC 708	11	-0.058	0.011	0.38	0.32	-0.054	0.020	0.36	0.45
NGC 708	12	-0.0506	0.0085	0.34	0.25	-0.035	0.019	0.23	0.40
NGC 708	13	-0.0420	0.0075	0.28	0.22	-0.025	0.018	0.17	0.35
NGC 708	14	-0.0490	0.0080	0.33	0.24	-0.025	0.015	0.17	0.30
NGC 7014	10	-0.0513	0.0078	0.34	0.24	0.008	0.010	-0.05	0.19
NGC 7014	11	-0.0422	0.0063	0.28	0.20	0.035	0.014	-0.23	0.30
NGC 7014	12	-0.0523	0.0076	0.35	0.24	0.028	0.012	-0.19	0.26
NGC 7014	13	-0.0553	0.0065	0.37	0.23	0.0184	0.0098	-0.12	0.20
IC 4296	10	0.0088	0.0096	-0.06	0.18	0.063	0.011	-0.42	0.33
IC 4296	11	-0.0062	0.0095	0.04	0.17	0.0585	0.0092	-0.39	0.28
IC 4296	12	-0.0097	0.0083	0.06	0.16	0.0565	0.0072	-0.38	0.24
IC 4296	13	-0.0176	0.0081	0.12	0.17	0.0595	0.0065	-0.40	0.24

(c)

NGC or IC (1)	Number of bins (7)	Blue Slope[a] (8)	Blue Slope Error[a] (9)	p (10)	Error on p (11)	Red Slope[a] (12)	Red Slope Error[a] (13)	p (14)	Error on p (15)
Gemini GMOS photometry									
NGC 5193	10	-0.046	0.027	0.31	0.56	-0.007	0.046	0.05	0.78
NGC 5193	11	-0.048	0.021	0.32	0.45	-0.031	0.042	0.21	0.77
IC 4329	10	-0.0767	0.0093	0.51	0.32	0.021	0.024	-0.14	0.44
IC 4329	11	-0.052	0.013	0.35	0.33	0.049	0.020	-0.33	0.44
IC 4329	12	-0.111	0.017	0.74	0.53	-0.072	0.034	0.48	0.73
IC 4329	13	-0.083	0.014	0.55	0.42	-0.062	0.030	0.42	0.64
IC 4329	14	0.008	0.039	-0.05	0.63	-0.074	0.029	0.50	0.64
NGC 3311	10	-0.1063	0.0026	0.71	0.28	0.0057	0.0046	-0.038	0.090
NGC 3311	11	-0.1028	0.0027	0.69	0.27	0.0074	0.0038	-0.050	0.080
NGC 3311	12	-0.1178	0.0064	0.79	0.36	0.0049	0.0029	-0.033	0.059

[a] Values converted from $(g\text{-}i)_0$ to $(B\text{-}I)_0$

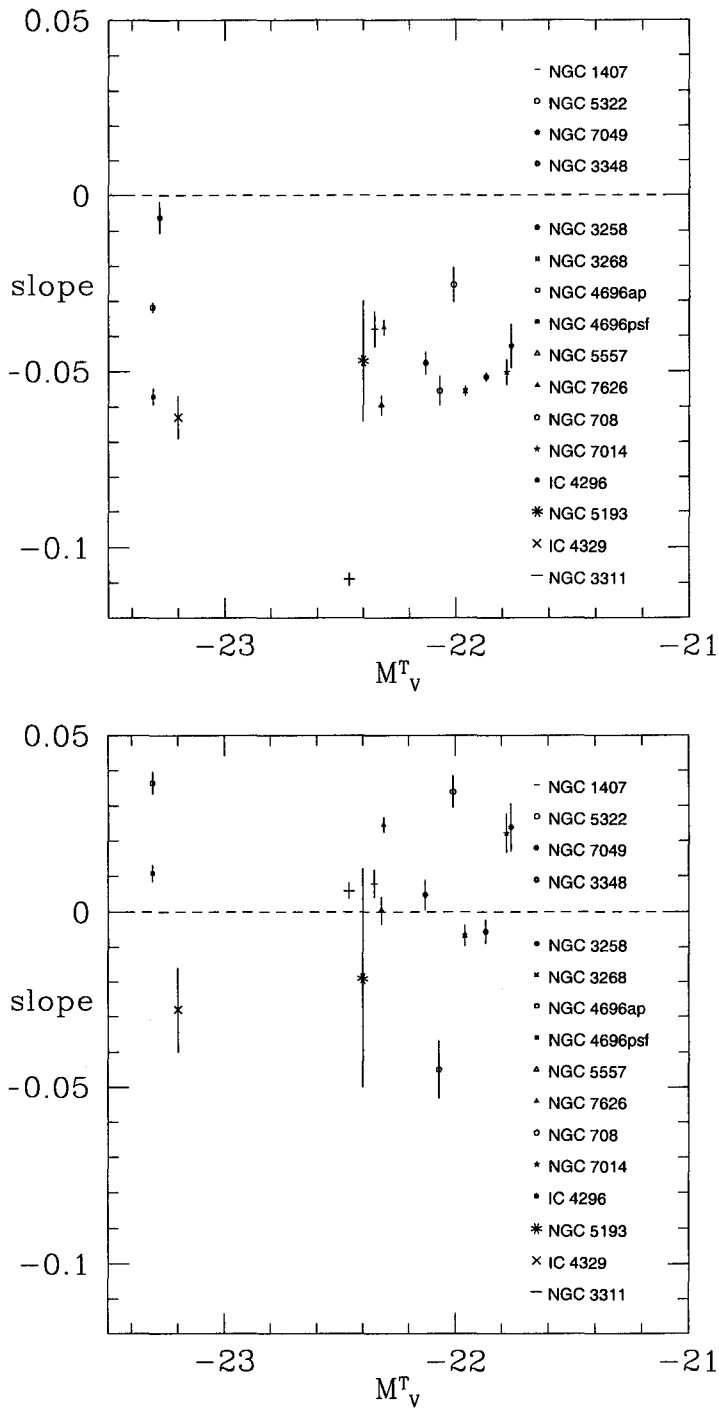

Figure 3.14: Mean of blue (above) and mean of red (below) colour slopes versus host galaxy luminosity

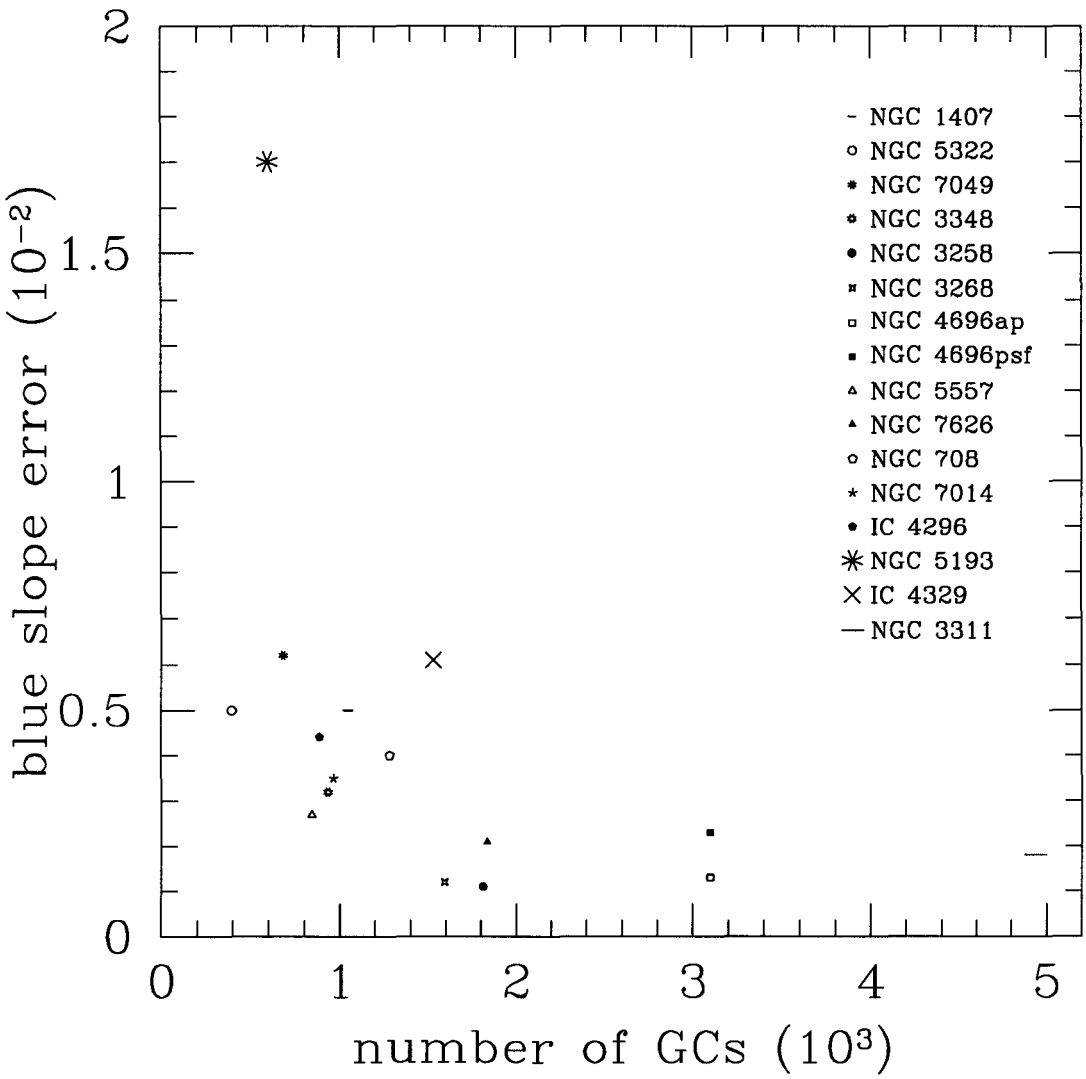

Figure 3.15: Blue slope error versus number of GCs in GCS

Table 3.5: The mean of blue and red slopes with their corresponding p values, where p is defined in the relation $Z = M^p$ (see section 5.3).

NGC or IC (1)	Mean Blue Slope (16)	Error on Mean (17)	Mean p (18)	Error on p (19)	Mean Red Slope (20)	Error on Mean (21)	Mean p (22)	Error on p (23)
(B, I) photometry from ACS/WFC								
NGC 1407	-0.0380	0.0050	0.25	0.13	0.0080	0.0038	-0.053	0.074
NGC 5322	-0.0253	0.0050	0.17	0.11	0.0341	0.0045	-0.23	0.11
NGC 7049	-0.0429	0.0062	0.29	0.16	0.0239	0.0068	-0.16	0.15
NGC 3348	-0.0477	0.0032	0.32	0.10	0.0049	0.0041	-0.034	0.075
NGC 3258	-0.0516	0.0011	0.34	0.07	-0.0055	0.0033	0.037	0.058
NGC 3268	-0.0555	0.0012	0.37	0.07	-0.0067	0.0029	0.045	0.055
NGC 4696ap	-0.0317	0.0013	0.21	0.05	0.0366	0.0031	-0.244	0.088
NGC 4696psf	-0.0570	0.0023	0.38	0.09	0.0109	0.0023	-0.073	0.049
NGC 5557	-0.0595	0.0027	0.40	0.11	0.0004	0.0038	-0.002	0.069
NGC 7626	-0.0376	0.0021	0.250	0.071	0.0246	0.0021	-0.164	0.062
B photometry from ACS/WFC, I from WFPC2								
NGC 708	-0.0554	0.0047	0.37	0.12	-0.0450	0.0081	0.30	0.17
NGC 7014	-0.0503	0.0035	0.34	0.11	0.0222	0.0056	-0.15	0.11
IC 4296	-0.0062	0.0044	0.041	0.085	0.0593	0.0040	-0.40	0.13
Gemini GMOS photometry								
NGC 5193	-0.047	0.017	0.32	0.35	-0.019	0.031	0.13	0.55
IC 4329	-0.0629	0.0061	0.42	0.18	-0.028	0.012	0.19	0.24
NGC 3311	-0.1090	0.0018	0.73	0.17	0.0060	0.0021	-0.040	0.042

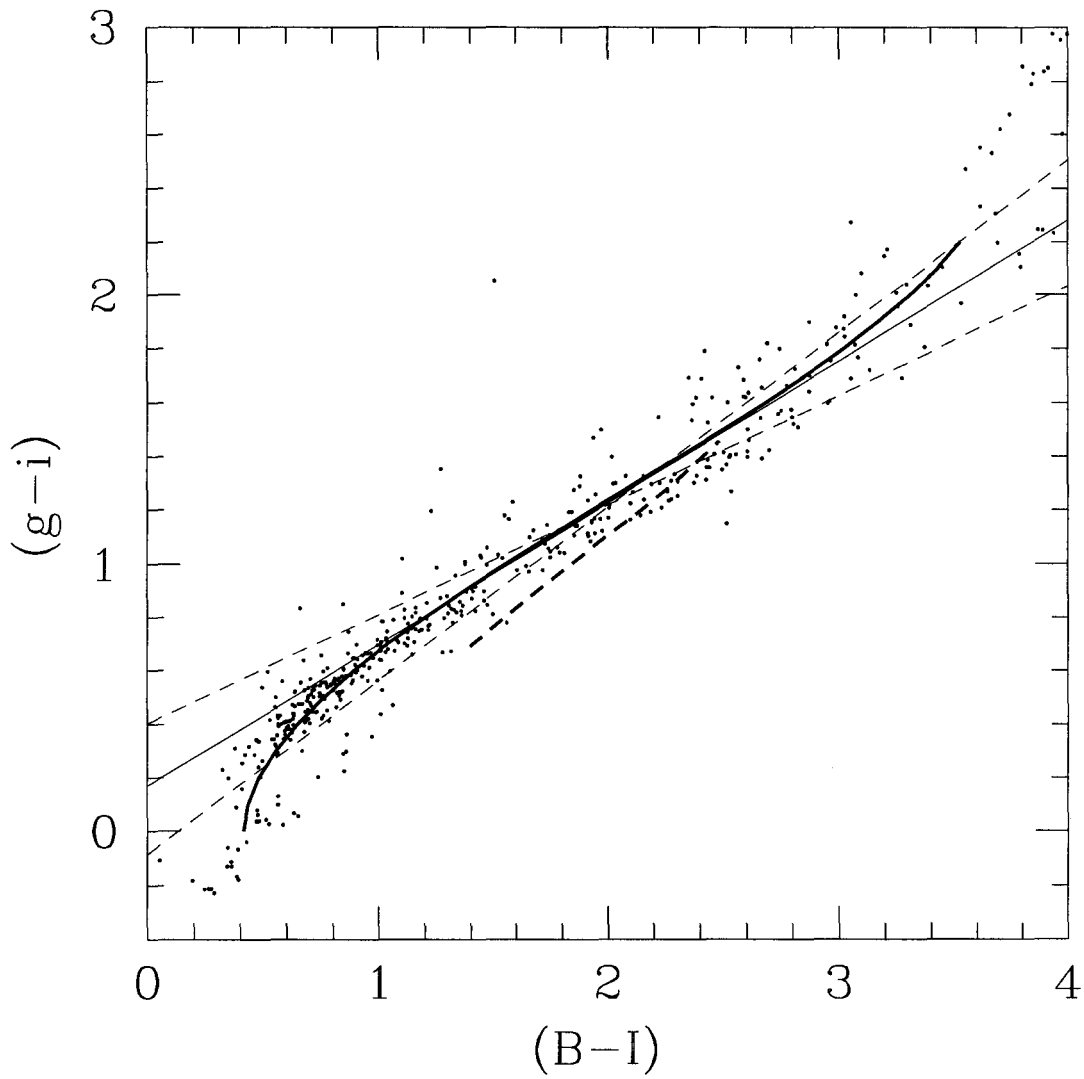

Figure 3.16: The colour conversion between *(g-i)* and *(B-I)*. The observational data points of standard stars are shown with a short dashed line, and a single-star population model from Maraston (2005). See section 3.2.2 for further details.

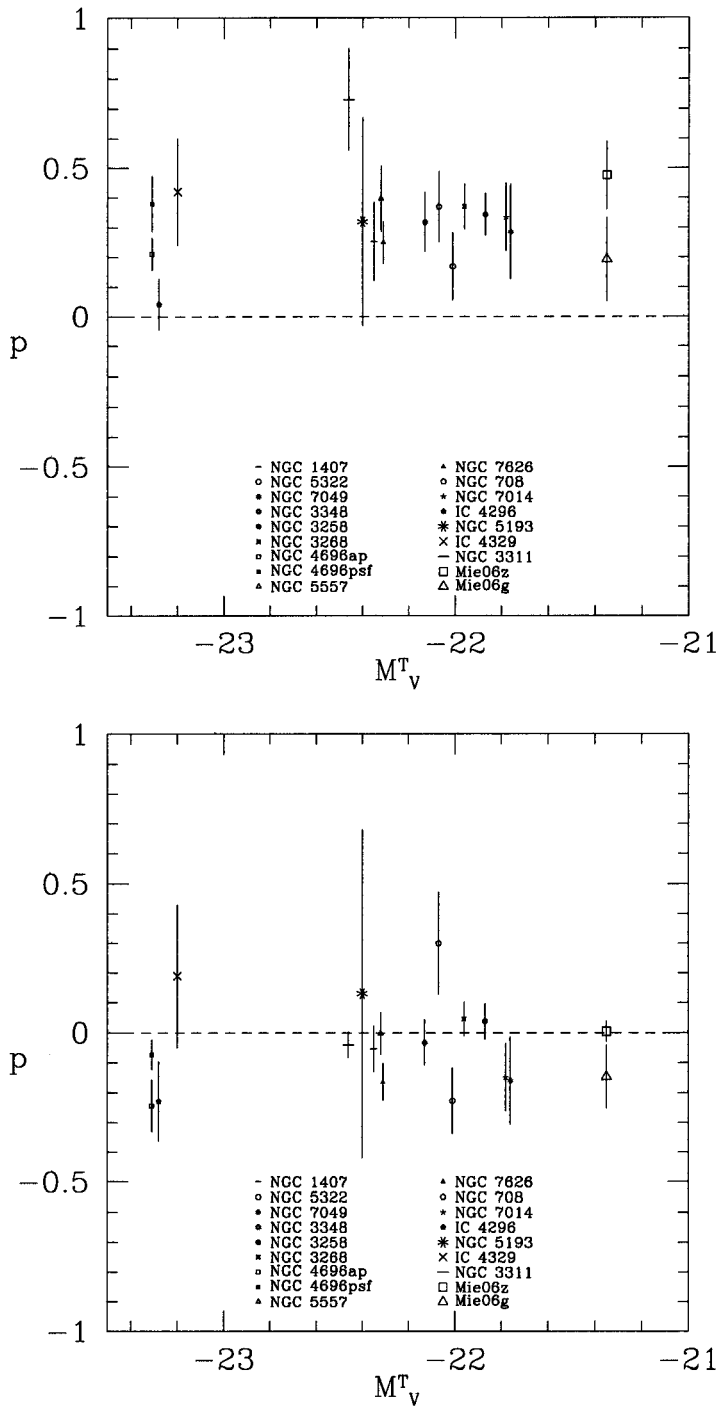

Figure 3.17: Mean of blue (above) and red (below) slopes of metallicity, zoomed in. The data points of Mieske et al. (2006b) are shown here as Mie06z and Mie06g for comparison.

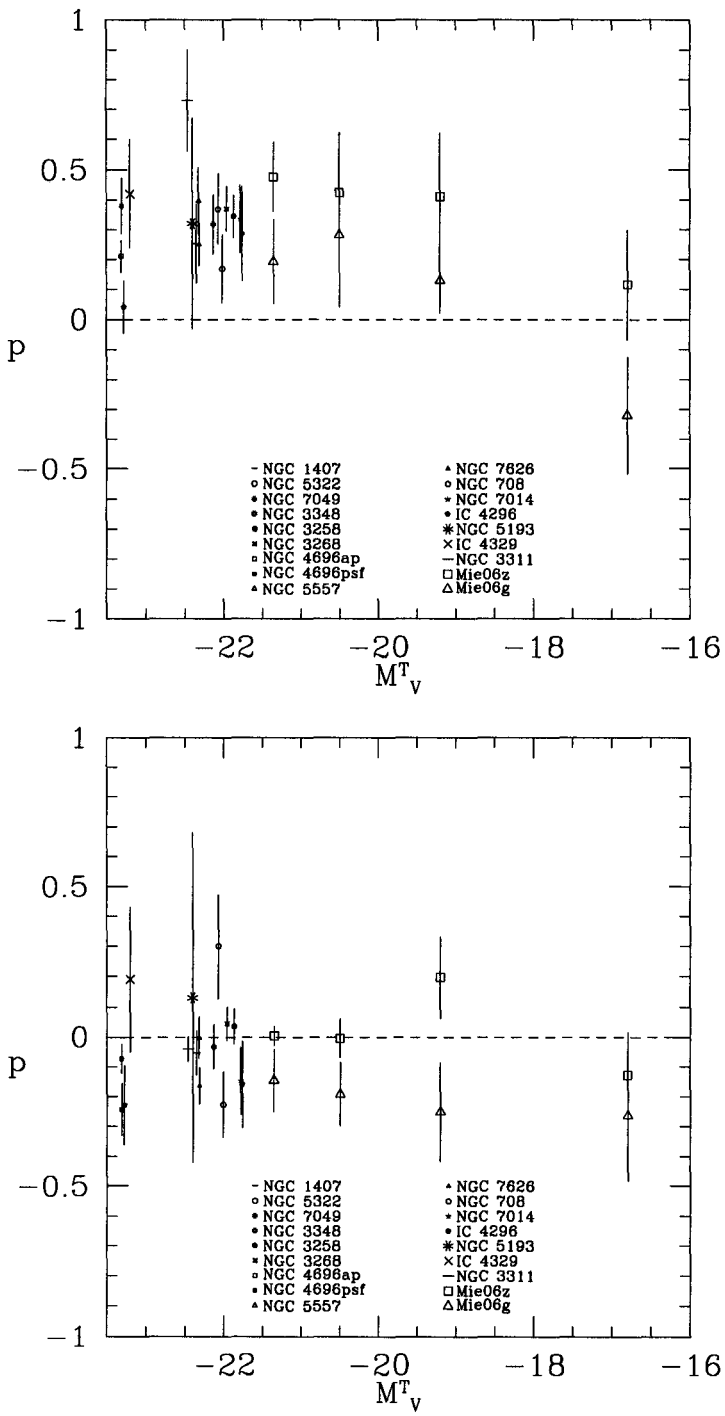

Figure 3.18: Mean of blue (above) and red (below) slopes of metallicity, zoomed out. The data points of Mieske et al. (2006b) are shown here as Mie06z and Mie06g for comparison.

Chapter 4

DISCUSSION

4.1 Summary

In this study we have determined the MMR for the GCSs of fifteen galaxies. HST *(B,I)* photometry was used for twelve of these galaxies: eight with both B and I obtained with ACS/WFC (previously presented in Harris et al. 2006), four with B from the ACS and I from WFPC2. Gemini South *(g,i)* photometry obtained with the GMOS camera was used for the remaining three galaxies. NGC 3311 had been previously analysed in Wehner et al. (2008a). NGC 5193 and IC 4329 were newly analysed GCSs presented here. We find bimodal colour distributions for these two new galaxies.

Colour-magnitude slopes were found for both subpopulations within each of the GCSs by using a "line splitting" method. Field contamination becomes significant at lower luminosities and may affect these slopes. However, in the example of the two newly analysed galaxies it is worth noting that even neglecting data points fainter than $M_i \backsim$ -9 for 5193, and -9.5 for 4329 (the points where field contamination becomes important), there are still slopes for the blue subpopulations.

These colour-magnitudes slopes were converted to mass-metallicity slopes so that comparisons to other data (Mieske et al., 2006b) could be made. We extend the work of Mieske et al. to higher luminosities of the host galaxy. The blue metallicity slope values are clearly offset by $p \backsim 0.35$ whereas the red metallicity slope values are consistent with a line including zero. The blue trend is consistent with the idea that more massive metal-poor GCs form in more massive potential wells; the lack of a red trend is expected if the metal-rich GCs are forming in a deep potential well of the host-galaxy, i.e., where enrichment is independent of the mass of the cluster (Harris et al., 2006). The blue metallicity slope values drop down at fainter luminosities - the faintest bin in Mieske et al. (2006b) - because this is the area of dwarf elliptical galaxies; in these types of galaxies the highest luminosity GCs seen in gEs are not present and these high-luminosity clusters strongly affect the slope.

Harris et al. (2006) see no correlation between GC colour and magnitude at lower GC luminosities. We do not see that here, but argue for a continuous sloping trend from higher to lower magnitudes. This is shown most clearly in figure 3.13, which plots the different WLSQ fits where increasingly more bins at higher magnitudes are added. If there was a trend at higher magnitudes for the slope to become steeper, then we would expect the linear fit that we impose to become steeper - but this does not happen.

There is still some speculation about whether or not a bimodal distribution in colour implies a bimodal distribution in metallicity (Worthey, 1994; Yoon et al., 2006), although there is evidence against this (Puzia et al., 2005; Strader et al., 2005).

Kundu (2008) also refers to a specific problem with HST data. The MMR is observed, Kundu claims, because there is a measurable mass-size relationship in GCs. If the same aperture radius is used for all GCs, then the luminosity of the brightest GCs will be underestimated - and this will have a greater effect on the blue GCs as they are larger, than the red ones (e.g., Spitler et al. 2006). When a *(bluer-redder)* colour is plotted against the redder magnitude, Kundu (2008) confirm previous work (e.g., Mieske et al. 2006b) that a stronger blue MMR is seen than if plotted against the bluer magnitude. However, the size of the aperture is also important. If a relatively smaller aperture size is chosen for the blue band while a larger one is chosen for the red band, this increases the blue MMR.

The GCSs studied by Harris et al. (2006) include more distant galaxies than most of the studies looked at in Kundu (2008), and so individual GCs may not be resolved. However, Harris et al. (2006) claim that the brightest GCs are resolved, and therefore Kundu suggests that even these GCSs may suffer the same observational problems.

The arguments against the high-resolution HST do not apply to the Gemini data presented here, where blue MMRs are still seen, because PSF-based photometry is valid for ground-based observations where individual GCs are not resolved, and - with the exception of NGC 4696 where both PSF and aperture photometry are used - PSF photometry is used for all the HST data.

The results of this paper were not necessarily expected. The work by Mieske et al. (2006b) shows that for dwarf galaxies (mean host-galaxy luminosity of $M_V = 17$), there is only a very weak blue-MMR if there is one at all. We wanted to study the MMR at brighter host-galaxy luminosities to see what

happened to the relationship at this other end of the host-galaxy luminosity spectrum. By finding that BCGs have a similar blue-MMR and similarly lack a red-MMR compared to lower host-galaxy luminosities, it seems likely that the same GC formation process is occurring in both BCGs and typical galaxies (unlike with dwarf galaxies).

4.2 Points of Interest to Note About Individual Galaxies

Sparse cluster systems are those which we define to have $S_N < 1.5$ include NGCs 1407, 5322, 3348, 5557, 7014 and 5193, and IC 4296. Rich cluster systems, with $S_N > 2.5$, include NGCs 3258, 3268, 4696, 7626 and 3311, and IC 4329 (Harris et al., 2006).

It is still unclear whether or not NGC 5193 is the central giant elliptical galaxy in Abell 3565 (Willmer et al., 1999). While we do focus on BCGs within this work, Mieske et al. (2006b) show that MMRs are present in other types of galaxies, so even if NGC 5193 is not a BCG, we continue to include it in our results. However, although the errors are extremely large for this galaxy because of the low numbers of GCs within its GCS, the blue and red MMRs are consistent with it being a BCG.

NGCs 3258 and 3268 are a co-dominant central pair. Bassino et al. (2008) present Very Large Telescope photometry of these two Antlia cluster gE galaxies. They find NGC 3258 has 6000 $\pm$ 150 GCs and NGC 3268 has 4750 $\pm$ 150 GCs (compared to our estimates of 6928 and 6017, respectively), with some intra-cluster GC candidates. They clearly see that the GCSs are bimodal, although the brightest GCs show a unimodal distribution with a peak

intermediate to the fainter bimodal peaks, which is also seen in other gEs (e.g., Harris et al. 2006). However, Bassino et al. (2008) find that the unimodal peak tends towards bluer colours, whereas Harris et al. (2006) find that they tend towards redder colours. Bassino et al. (2008) also find that the red GCs show a steeper radial density profile than the blue GCs, and follow the galaxies' brightness profile.

Wehner et al. (2008a) find that for NGC 3311 it has $\backsim$ 16,000 GCs and a specific frequency value of $S_N = 12.5 \pm 1.5$ (compared to our values of $\backsim$ 7,500 and $S_N = 11.5$). They also find that NGC 3309, which is about 100″ from NGC 3311, has a specific frequency of $S_N = 0.6 \pm 0.4$. Some GCs are intra-cluster GC candidates. Wehner et al. (2008a) conclude that the Hydra Cluster does not have a co-dominant central pair, but rather NGC 3311 is completely dominant.

4.3 Comparing Different Methods

We were concerned with the effect of possibly introducing MMRs to the data ourselves through our line splitting method. If the GCS contains two GC subpopulations that are perfectly vertical, overlap at fainter luminosities and contain exactly the same number of GCs, once a vertical line split is used to divide the subpopulations blue GCs that fall red-ward of the line will be counted in the red subpopulation, and vice versa. In this case where the subpopulations are equal in number, there will be no resulting MMRs (i.e., the MMRs will be consistent with zero). However, if the proportion of numbers is unequal, MMRs will be artificially created. For example, if the blue subpopulation dominates, more blue GCs will fall red-ward of the dividing line

than red GCs that fall blue-ward. A blue MMR will result, with the offset expected similar to the one that is observed, as will a red MMR, seen in the same direction. If the red subpopulation dominates, more red GCs will fall blue-ward of the dividing line, and a negative offset for the red subpopulation would be expected along with a negative offset for the blue subpopulation.

We also note that the measurement scatter increases with fainter magnitudes, so that the amount of overlap between the two subpopulations also increases. This can be seen clearly in Wehner et al. (2008b) with their figure 13 and their table 2. Going from an i-magnitude of 22 to 26, the dispersion increases by an amount of $\sigma_{(g-i)} = 0.104$. We also note that the red peak in Wehner et al. remains fairly constant (i.e., it only varies by an amount of $(g\text{-}i) = 0.022$) whereas the blue peak gets progressively bluer with fainter magnitudes by an amount $(g\text{-}i) = 0.145$.

A *second* line splitting was used to counter this effect, where the second split was line exactly in between the best-fits using the initial split. The galaxies that are dominated by the red subpopulations (NGCs 1407, 5322, 7049, 3348, 4696ap, 5557 and 7626, and IC 4296) have red MMRs that are *all* slightly negative, in the range of $0 < p <$ -0.35. This is consistent with the above argument for a red MMR where the red subpopulation dominates. However, these galaxies all have blue MMRs that are around the mean value of $p \backsim 0.35$. This is not consistent with the expectations of the argument presented above, and therefore provides some support to our line splitting method.

One way to avoid the issue of how the overlapping subpopulations could skew MMRs is to use KMM and RMIX fits. By binning the GCS data in

magnitudes, and noting the peak values of each subpopulation returned in the fits, a colour-magnitude slope can again be obtained and compared with the slopes obtained with our line splitting method.

Data from KMM fits presented in Harris et al. (2006) for six galaxies are used to make the slopes seen in figure 4.1 (NGCs 7049 and 5322 are not included in this part of the analysis as only one point per subpopulation was calculated, and so no slopes could be obtained). For the Gemini galaxies, we binned the data for each galaxy in 0.5 magnitude bins, and applied RMIX to each bin. The top two bins for NGC 5193 and IC 4329 were not used in the fit because of very low sample numbers in the brightest regions, although they are still shown on the plots. The resulting slopes are compared with the line splitting method in figure 4.2. The values of the slopes with their errors are shown in table 4.1, and are compared visually in figure 4.3. Five of the nine blue MMRs and six of the nine red MMRs are consistent within errors between the KMM/RMIX fits slopes and the line splitting slopes. This provides further support for the line splitting method in this work.

4.4 Future Work

We will undertake numerical simulations that will test whether the method of line splitting used in this work will automatically create sloping bins in a more quantitative analysis than the argument above. We will also complete artificial star tests to measure the completeness for the data.

Further data obtained with the Yale 1m-telescope will be analysed to find any remaining zeropoint errors in the calibrations.

Bimodality origin is still unexplained. Why are there only two components, not more, and why is there a separation seen between the two groups and not a continual gradation? GC formation within the full context of galaxy formation and evolution is still relatively poorly understood. In exploring GCSs and analysing the MMRs, we hope to have contributed to this discussion.

Table 4.1: Comparing line split slopes with slopes from peaks of KMM and RMIX fits, also shown in figure 4.3. Discrepant pairs (i.e., pairs whose values are not within each other's errors) are highlighted in bold.

Galaxy (1)	Method (2)	Blue Slope (3)	Error (4)	Red Slope (5)	Error (6)
NGC 1407	Line split bins	-0.0296	0.0099	0.0041	0.0076
	KMM peaks	-0.003	0.026	0.028	0.025
NGC 3348	Line split bins	-0.0363	0.0066	**-0.002**	**0.011**
	KMM peaks	-0.044	0.017	**0.0273**	**0.0083**
NGC 3258	Line split bins	**-0.0534**	**0.0037**	-0.020	0.010
	KMM peaks	**-0.036**	**0.011**	-0.004	0.012
NGC 3268	Line split bins	**-0.0523**	**0.0029**	-0.0100	0.0073
	KMM peaks	**-0.0606**	**0.0053**	-0.0139	0.0125
NGC 4696	Line split bins	-0.0305	0.0025	**0.0309**	**0.0086**
	KMM peaks	-0.037	0.013	**-0.042**	**0.016**
NGC 5557	Line split bins	**-0.0620**	**0.0064**	0.0011	0.0093
	KMM peaks	**-0.0303**	**0.0029**	-0.0146	0.0073
NGC 5193	Line split bins	**-0.024**	**0.014**	-0.008	0.024
	RMIX peaks	**-0.110**	**0.026**	0.025	0.086
IC 4329	Line split bins	-0.0405	0.0049	0.011	0.013
	RMIX peaks	-0.033	0.014	0.0286	0.0093
NGC 3311	Line split bins	-0.0561	0.0014	**0.0030**	**0.0025**
	RMIX peaks	-0.0596	0.0049	**-0.0123**	**0.0074**

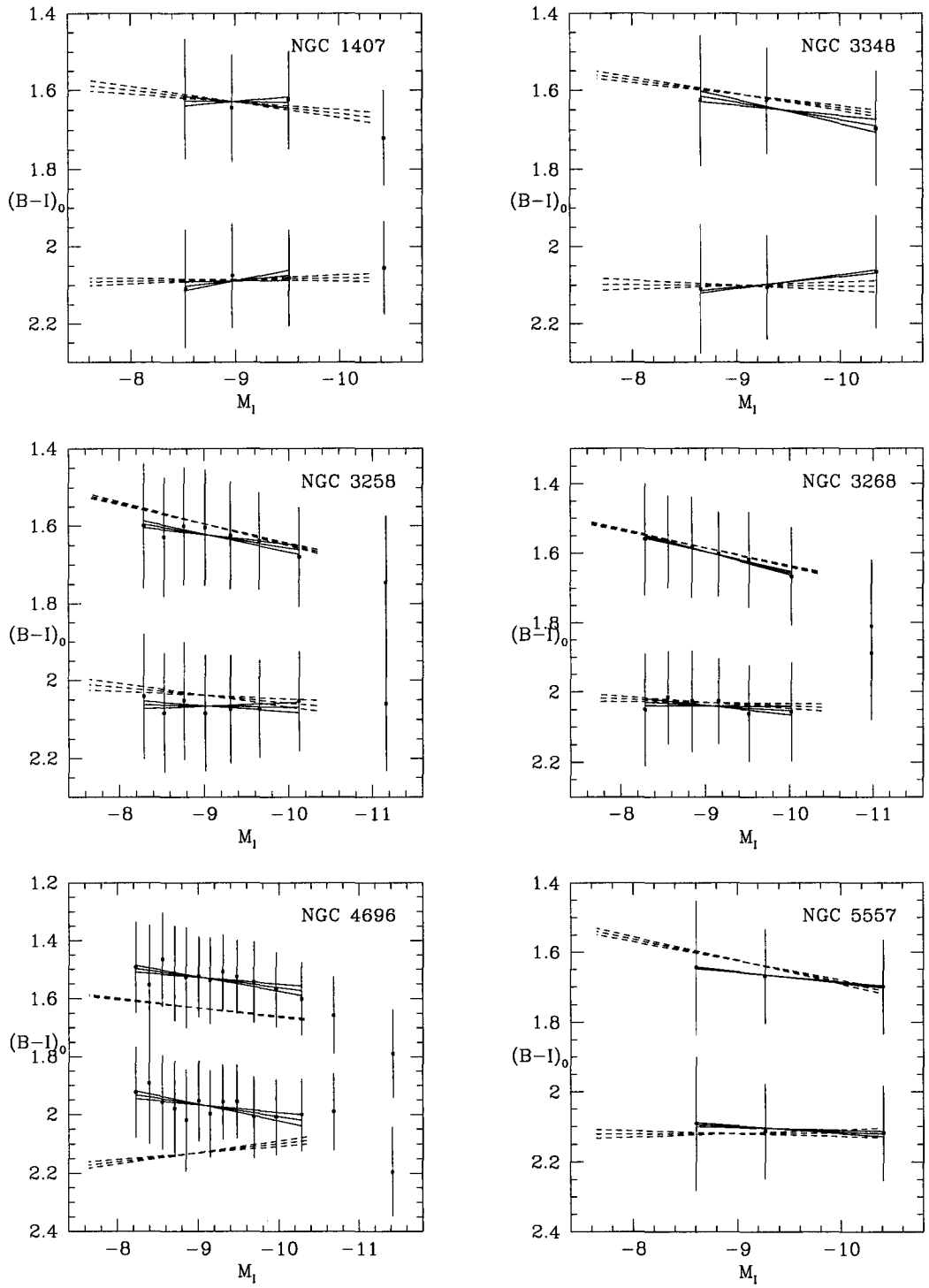

Figure 4.1: Comparing colour slopes obtained in the line splitting method (dashed lines) to those in Harris et al. (2006) (solid lines)

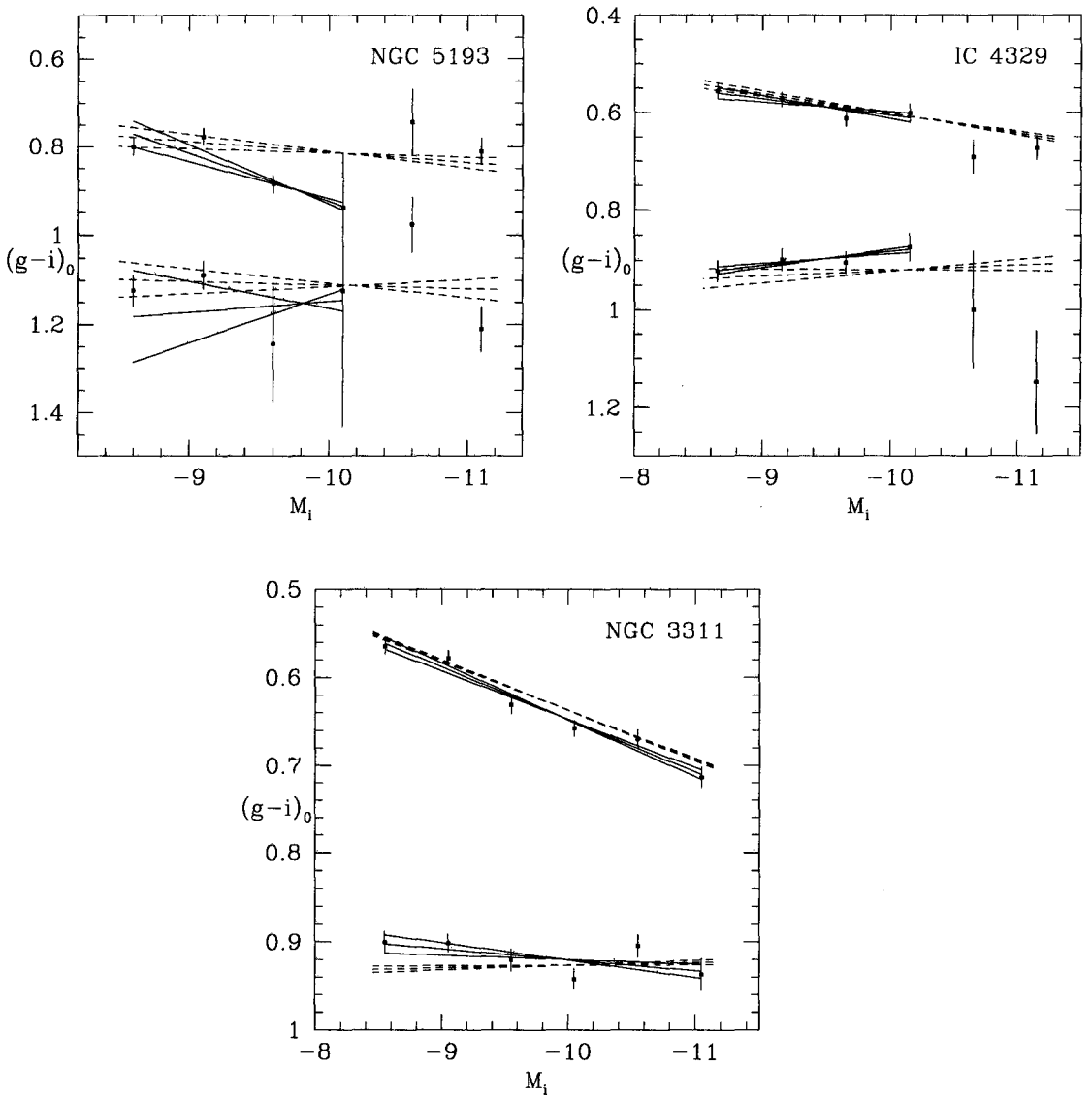

Figure 4.2: RMIX slopes (solid lines) compared with line splitting slopes (dashed lines)

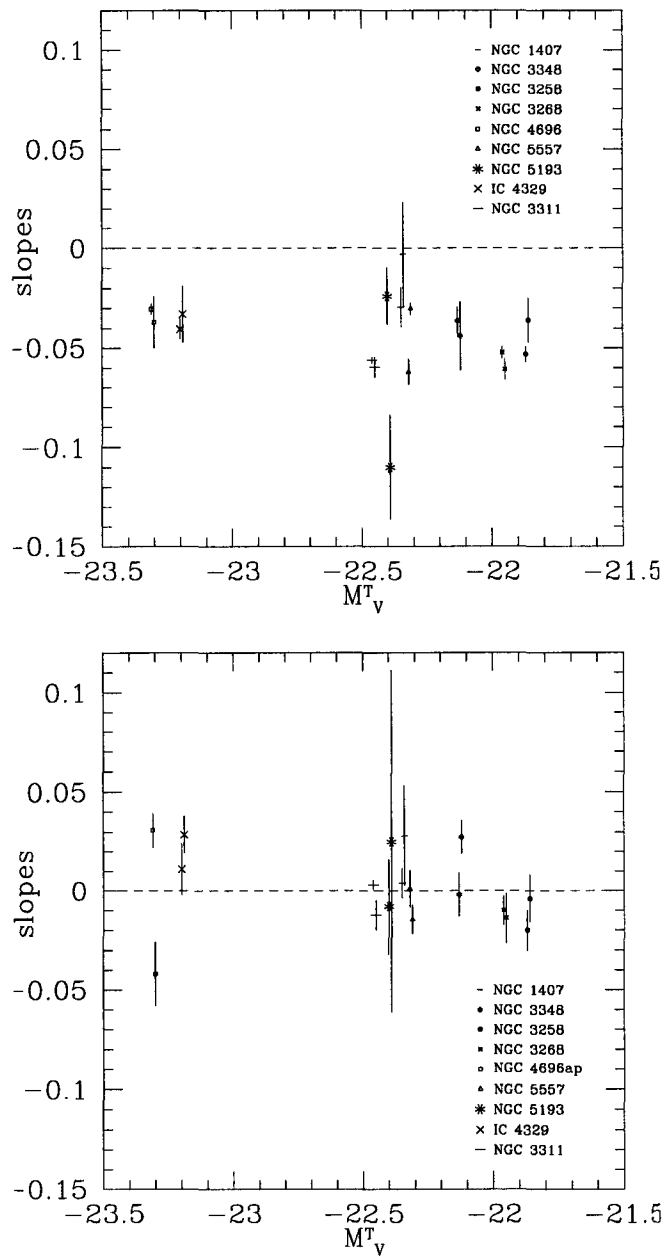

Figure 4.3: Comparing line split colour slopes with colour slopes from peaks of KMM and RMIX fits as in table 4.1. The top and bottom plots are for the blue and red subpopulations, respectively. For each GCS there are two data points shown: line split slopes are on the left, with KMM/RMIX slopes offset from the true host-galaxy magnitude to the right.

Chapter 5

APPENDIX

5.1 Daophot.opt, allstar.opt and photo.opt files

Table 5.1: Daophot.opt, allstar.opt and photo.opt files from Harris (2002), private communication

Abbreviation in file	Meaning	Example from IC 4329 file
daophot.opt		
FWHM	FWHM from the PSF profile[a]	3.0
FIT	PSF-fitting radius, which is a little larger than FWHM	3.3
PSF	PSF box size (approximately four times the FWHM)	12.0
READ	Readnoise (ADU)	1.6791
GAIN	CCD gain (e^- per ADU)	2.1816
TH	Detection threshold (sigma units)	4.0
AN	Analytical PSF model	1.0
LOWBAD	Low-cutoff threshhold for bad pixels (sigma units)	10.0
HIBAD	High-cutoff threshhold for bad pixels (ADU)[c]	100,000.0
WATCH	Level of output to screen	1.0
VAR	PSF fit: 0=constant, 1=linear, 2=quadratic in (x,y)	2.0
allstar.opt		
FIT	As above	3.3
ISKY	Inner-sky radius of annulus	22.0
OSKY	Outer-sky radius of annulus	32.0
WATCH	As above	1.0
REDET	Redetermine centroids?[b]	1.0
PERCENT ERROR	Error allowed between the flatfield and program images	0.0
PROFILE ERROR	Error allowed on the PSF fit	0.0
photo.opt		
A1	Radius of first and smallest aperture (pixels)	14.5
A2	Radius of second and smallest aperture (pixels)	0.0
A3	Radius of third and smallest aperture (pixels), etc	0.0
ISKY	As above	22.0
OSKY	As above	32.0

[a] Obtained using the IRAF command imexamine, typing 'a' and calculating the average
[b] (x,y) coordinates are free parameters (redet=1) or not (redet=0)?
[c] Again, from imexamine, typing 'r'

5.2 Calculating the specific frequency

5.2.1 HST Data

To estimate the total number of GCs in the system for galaxies where we had *(B-I)* data (i.e., the HST data), we first counted the number of GCs within the same colour limits as the initial selection region of section 3.1.1 and brighter than the limiting magnitude of M_I = -7.5 (i.e., the region in which we counted was only enclosed on three sides). This limiting magnitude was then converted to M_V with *UBVRI* standard star data from Landolt (1992). *(V-I)* was plotted against *(B-I)* as shown in the upper panel of figure 5.1, and the following conversion equation was obtained:

$$(V - I) = 0.53(B - I). \tag{5.1}$$

We then assumed that the number of GCs per unit magnitude is described by a Gaussian, with - for a gE - a mean value of M_V = -7.33 and a standard deviation of 1.4 magnitudes (Harris, 2001).

The statistics book and online applet[1] by Lane (1999) were then used to find the fraction of GCs were brighter than the limiting magnitude. By dividing the number of GCs above the limiting magnitude by this fraction, the estimate for the total number of GCs in the system was obtained (i.e., the values in column (8) in table 3.1). The specific frequency, S_N is then calculated from

[1] The online applet is available at http://davidmlane.com/hyperstat/z-table.html

$$S_N = N_{GC} 10^{-0.4(M_V+15)} \tag{5.2}$$

(Harris & van den Bergh, 1981).

5.2.2 Gemini Data

To estimate the total number of GCs in the systems where we had *(g-i)* data (i.e., the Gemini data), we first counted the number of GCs within the same colour limits as the initial selection region of section 3.1.2 and brighter than the limiting magnitudes of M_i=-8.35, -8.4 and -8.3 for NGC 5193, IC 4329 and NGC 5193. These magnitudes were converted to M_V with the *ugriz* standard star catalogue by E. Wehner referenced in section 2.4.3. *(i-V)* was plotted against *(g-i)* as shown in the lower panel of figure 5.1, and the following conversion equation was obtained:

$$(i - V) = -0.69(g - i) + 0.8238 \tag{5.3}$$

The total number of GCs and specific frequency was then found in a similar manner to the above.

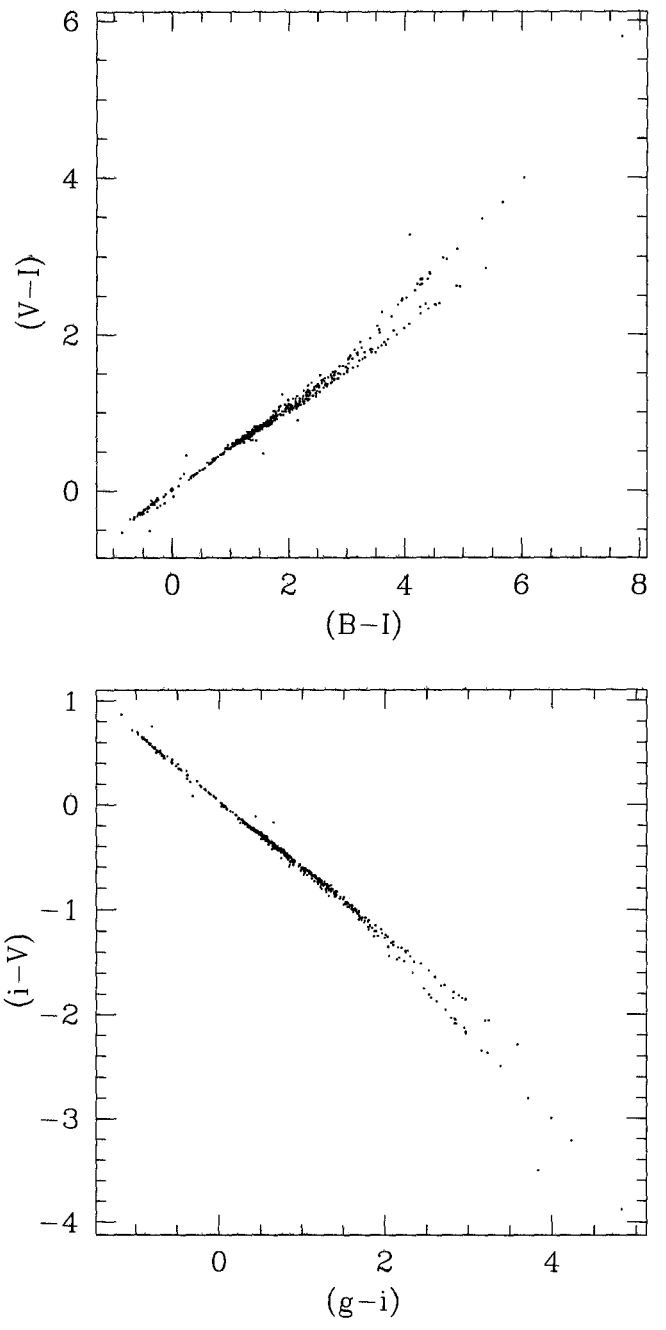

Figure 5.1: Comparing *(V-I)* against *(B-I)* in the upper panel, and *(i-V)* against *(g-i)* in the lower panel, for standard stars with data from Landolt (1992) and the standard star catalogue by E. Wehner referenced in section 2.4.3.

5.3 Deriving the Index for the Mass-Metallicity Relation

Throughout this derivation, I have used the colour-metallicity relation given by 3.8 (and repeated below in 5.4) from Harris et al. (2006) to be able to give a concrete example.

$$\frac{\Delta(B\text{-}I)_0}{\Delta[\mathrm{Fe/H}]} = 0.375 \pm 0.049 \tag{5.4}$$

First, let a be the value of the slope in CMDs, such that

$$a = \frac{\Delta(B\text{-}I)_0}{\Delta M_I}. \tag{5.5}$$

Then, use 5.4 and the magnitude-luminosity relation, so that 5.5 becomes

$$a = \frac{0.375\Delta[\mathrm{Fe/H}]}{-2.5\Delta log_{10}L}. \tag{5.6}$$

Using the definition [Fe/H] = logZ, and assuming a constant mass-to-light (M/L) ratio, 5.6 can be written as

$$a = \frac{0.375\Delta logZ}{-2.5\Delta logM}. \tag{5.7}$$

Rearranging 5.7 gives

$$\Delta logZ = \frac{-2.5a}{0.375}\Delta logM = p\Delta logM, \tag{5.8}$$

where

$$p = \frac{-2.5a}{0.375}(= \frac{\Delta logZ}{\Delta logM}) \tag{5.9}$$

This p can be shown to be the index of the mass-metallicity relation, $Z{=}M^p$ with the following:

$$\frac{dZ}{dM} = pM^{p-1} = p\frac{M^p}{M} = p\frac{Z}{M}. \tag{5.10}$$

Rearranging 5.10 gives

$$p = \frac{M}{dM}\frac{dZ}{Z}. \tag{5.11}$$

If 5.11 is manipulated in the following way

$$p = \frac{\frac{1}{Z}dZ}{\frac{1}{M}dM} = \frac{\Delta logZ}{\Delta logM} \tag{5.12}$$

then it can be seen that the p here in 5.12 is the same as the p in 5.9.

Bibliography

Ashman, K. M., Bird, C. M., & Zepf, S. E. 1994, AJ, 108, 2348

Ashman, K. M., & Zepf, S. E. 1992, ApJ, 384, 50

—. 1998, Globular Cluster Systems, Cambridge Astrophysics Series 30 (Cambridge University Press)

Balcells, M., & Carter, D. 1993, A&A, 279, 376

Bardelli, S., Venturi, T., Zucca, E., De Grandi, S., Ettori, S., & Molendi, S. 2002, A&A, 396, 65

Barmby, P., Huchra, J. P., Brodie, J. P., Forbes, D. A., Schroder, L. L., & Grillmair, C. J. 2000, AJ, 119, 727

Bassino, L. P., Faifer, F. R., Forte, J. C., Dirsch, B., Richtler, T., Geisler, D., & Schuberth, Y. 2006, A&A, 451, 789

Bassino, L. P., Richtler, T., & Dirsch, B. 2008, MNRAS, 421

Baugh, C. M., Croton, D. J., Gaztañaga, E., Norberg, P., Colless, M., Baldry, I. K., Bland-Hawthorn, J., Bridges, T., Cannon, R., Cole, S., Collins, C., Couch, W., Dalton, G., De Propris, R., Driver, S. P., Efstathiou, G., Ellis, R. S., Frenk, C. S., Glazebrook, K., Jackson, C., Lahav, O., Lewis, I., Lumsden, S., Maddox, S., Madgwick, D., Peacock, J. A., Peterson, B. A., Sutherland, W., & Taylor, K. 2004, MNRAS, 351, L44

Beasley, M. A., Baugh, C. M., Forbes, D. A., Sharples, R. M., & Frenk, C. S. 2002, MNRAS, 333, 383

Beasley, M. A., Bridges, T., Peng, E., Harris, W. E., Harris, G. L. H., Forbes, D. A., & Mackie, G. 2008, MNRAS, 502

Beasley, M. A., Strader, J., Brodie, J. P., Cenarro, A. J., & Geha, M. 2006, AJ, 131, 814

Becker, W. 1946, Veroeffentlichungen der Universitaets-Sternwarte zu Goettingen, 5, 159

Bekki, K. 2005, ApJ, 626, L93

Bekki, K., Beasley, M. A., Brodie, J. P., & Forbes, D. A. 2005, MNRAS, 363, 1211

Bekki, K., & Chiba, M. 2005, ApJ, 625, L107

Bekki, K., Couch, W. J., & Drinkwater, M. J. 2001a, ApJ, 552, L105

Bekki, K., Couch, W. J., Drinkwater, M. J., & Gregg, M. D. 2001b, ApJ, 557, L39

Bekki, K., & Freeman, K. C. 2003, MNRAS, 346, L11

Bekki, K., Yahagi, H., & Forbes, D. A. 2006, ApJ, 645, L29

—. 2007, MNRAS, 377, 215

Bekki, K., Yahagi, H., Nagashima, M., & Forbes, D. A. 2008, ArXiv e-prints, 0804:1842

Bernardi, M., Alonso, M. V., da Costa, L. N., Willmer, C. N. A., Wegner, G., Pellegrini, P. S., Rité, C., & Maia, M. A. G. 2002, AJ, 123, 2990

Bica, E., Dottori, H., Rodrigues de Oliveira Filho, I., Ortolani, S., & Barbuy, B. 1997, ApJ, 482, L49+

Bower, R. G., Lucey, J. R., & Ellis, R. S. 1992, MNRAS, 254, 601

Bridges, T. J., Hanes, D. A., & Harris, W. E. 1991, AJ, 101, 469

Brodie, J. P., & Huchra, J. P. 1991, ApJ, 379, 157

Brodie, J. P., & Strader, J. 2006, ARA&A, 44, 193

Bullock, J. S., Dekel, A., Kolatt, T. S., Kravtsov, A. V., Klypin, A. A., Porciani, C., & Primack, J. R. 2001, ApJ, 555, 240

Burgarella, D., Kissler-Patig, M., & Buat, V. 2001, AJ, 121, 2647

Cantiello, Michele, Blakeslee, P., J., Raimondo, & Gabriella. 2007, ArXiv e-prints, 0706:3943

Cantiello, M., & Blakeslee, J. P. 2007, ArXiv e-prints, 0709:1073

Carraro, G., & Lia, C. 2000, A&A, 357, 977

Cerviño, M., Valls-Gabaud, D., Luridiana, V., & Mas-Hesse, J. M. 2002, A&A, 381, 51

Chilingarian, I. V., & Mamon, G. A. 2008, MNRAS, 385, L83

Chincarini, G., & Rood, H. J. 1976, PASP, 88, 388

Cole, S., Percival, W. J., Peacock, J. A., Norberg, P., Baugh, C. M., Frenk, C. S., Baldry, I., Bland-Hawthorn, J., Bridges, T., Cannon, R., Colless, M., Collins, C., Couch, W., Cross, N. J. G., Dalton, G., Eke, V. R., De Propris, R., Driver, S. P., Efstathiou, G., Ellis, R. S., Glazebrook, K., Jackson, C., Jenkins, A., Lahav, O., Lewis, I., Lumsden, S., Maddox, S., Madgwick, D., Peterson, B. A., Sutherland, W., & Taylor, K. 2005, MNRAS, 362, 505

Côté, P., Marzke, R. O., & West, M. J. 1998, ApJ, 501, 554

Côté, P., McLaughlin, D. E., Cohen, J. G., & Blakeslee, J. P. 2003, ApJ, 591, 850

Côté, P., McLaughlin, D. E., Hanes, D. A., Bridges, T. J., Geisler, D., Merritt, D., Hesser, J. E., Harris, G. L. H., & Lee, M. G. 2001, ApJ, 559, 828

Cowie, L. L., Songaila, A., Hu, E. M., & Cohen, J. G. 1996, AJ, 112, 839

Dabringhausen, J., Hilker, M., & Kroupa, P. 2008, MNRAS, 395

De Lucia, G., & Blaizot, J. 2007, MNRAS, 375, 2

De Propris, R., Phillipps, S., Drinkwater, M. J., Gregg, M. D., Jones, J. B., Evstigneeva, E., & Bekki, K. 2005, ApJ, 623, L105

DeGraaff, R. B., Blakeslee, J. P., Meurer, G. R., & Putman, M. E. 2007, ApJ, 671, 1624

Denicoló, G., Terlevich, R., Terlevich, E., Forbes, D. A., Terlevich, A., & Carrasco, L. 2005, MNRAS, 356, 1440

Dirsch, B., Richtler, T., Geisler, D., Forte, J. C., Bassino, L. P., & Gieren, W. P. 2003, AJ, 125, 1908

Drinkwater, M. J., Gregg, M. D., Couch, W. J., Ferguson, H. C., Hilker, M., Jones, J. B., Karick, A., & Phillipps, S. 2004, Publications of the Astronomical Society of Australia, 21, 375

Drinkwater, M. J., Jones, J. B., Gregg, M. D., & Phillipps, S. 2000, Publications of the Astronomical Society of Australia, 17, 227

Efstathiou, G., & Jones, B. J. T. 1979, MNRAS, 186, 133

Eggen, O. J., Lynden-Bell, D., & Sandage, A. R. 1962, ApJ, 136, 748

Eisenstein, D. J., Zehavi, I., Hogg, D. W., Scoccimarro, R., Blanton, M. R., Nichol, R. C., Scranton, R., Seo, H.-J., Tegmark, M., Zheng, Z., Anderson, S. F., Annis, J., Bahcall, N., Brinkmann, J., Burles, S., Castander, F. J., Connolly, A., Csabai, I., Doi, M., Fukugita, M., Frieman, J. A., Glazebrook, K., Gunn, J. E., Hendry, J. S., Hennessy, G., Ivezić, Z., Kent, S., Knapp, G. R., Lin, H., Loh, Y.-S., Lupton, R. H., Margon, B., McKay, T. A., Meiksin, A., Munn, J. A., Pope, A., Richmond, M. W., Schlegel, D., Schneider, D. P., Shimasaku, K., Stoughton, C., Strauss, M. A., SubbaRao, M., Szalay, A. S., Szapudi, I., Tucker, D. L., Yanny, B., & York, D. G. 2005, ApJ, 633, 560

Evstigneeva, E. A., Drinkwater, M. J., Jurek, R., Firth, P., Jones, J. B., Gregg, M. D., & Phillipps, S. 2007a, MNRAS, 378, 1036

Evstigneeva, E. A., Gregg, M. D., Drinkwater, M. J., & Hilker, M. 2007b, AJ, 133, 1722

Fall, S. M., & Rees, M. J. 1988, in IAU Symposium, Vol. 126, The Harlow-Shapley Symposium on Globular Cluster Systems in Galaxies, ed. J. E. Grindlay & A. G. D. Philip, 323–330

Fan, Z., Ma, J., de Grijs, R., Yang, Y., & Zhou, X. 2007, ArXiv e-prints, 0711:4855

Fan, Z., Ma, J., de Grijs, R., & Zhou, X. 2008, MNRAS, 385, 1973

Fellhauer, M., & Kroupa, P. 2002, MNRAS, 330, 642

Fellhauer, M., Kroupa, P., & Evans, N. W. 2006, MNRAS, 372, 338

Forbes, D. A., Brodie, J. P., & Grillmair, C. J. 1997, AJ, 113, 1652

Forbes, D. A., & Forte, J. C. 2001, MNRAS, 322, 257

Fukugita, M., Ichikawa, T., Gunn, J. E., Doi, M., Shimasaku, K., & Schneider, D. P. 1996, AJ, 111, 1748

Geisler, D., & Forte, J. C. 1990, ApJ, 350, L5

Geisler, D., Lee, M. G., & Kim, E. 1996, AJ, 111, 1529

Gilmore, G., Wilkinson, M. I., Wyse, R. F. G., Kleyna, J. T., Koch, A., Evans, N. W., & Grebel, E. K. 2007, ApJ, 663, 948

Gómez, M., & Woodley, K. A. 2007, ApJ, 670, L105

Haşegan, M., Jordán, A., Côté, P., Djorgovski, S. G., McLaughlin, D. E., Blakeslee, J. P., Mei, S., West, M. J., Peng, E. W., Ferrarese, L., Milosavljević, M., Tonry, J. L., & Merritt, D. 2005, ApJ, 627, 203

Harris, G. L. H., Harris, W. E., & Poole, G. B. 1999, AJ, 117, 855

Harris, W. E. 1986, AJ, 91, 822

—. 1991, ARA&A, 29, 543

—. 1997, VizieR Online Data Catalog, 7202, 0

Harris, W. E. 1998, in Astronomical Society of the Pacific Conference Series, Vol. 136, Galactic Halos, ed. D. Zaritsky, 33–+

Harris, W. E. 2001, in Saas-Fee Advanced Course 28: Star Clusters, ed. L. Labhardt & B. Binggeli, 223–+

Harris, W. E. 2003, in Extragalactic Globular Cluster Systems, ed. M. Kissler-Patig, 317–+

Harris, W. E., & Harris, G. L. H. 2001, AJ, 122, 3065

—. 2002, AJ, 123, 3108

Harris, W. E., & Pudritz, R. E. 1994, ApJ, 429, 177

Harris, W. E., & van den Bergh, S. 1981, AJ, 86, 1627

Harris, W. E., Whitmore, B. C., Karakla, D., Okoń, W., Baum, W. A., Hanes, D. A., & Kavelaars, J. J. 2006, ApJ, 636, 90

Heavens, A., & Peacock, J. 1988, MNRAS, 232, 339

Hibbard, J. E., & Sansom, A. E. 2003, AJ, 125, 667

Hilker, M., Infante, L., Vieira, G., Kissler-Patig, M., & Richtler, T. 1999, A&AS, 134, 75

Hilker, M., Mieske, S., Baumgardt, H., & Dabringhausen, J. 2007, ArXiv e-prints, 0710:1691

Hwang, H. S., Lee, M. G., Park, H. S., Kim, S. C., Park, J.-H., Sohn, Y.-J., Lee, S.-G., Rey, S.-C., Lee, Y.-W., & Kim, H.-I. 2008, ApJ, 674, 869

Ibata, R. A., Gilmore, G., & Irwin, M. J. 1994, Nature, 370, 194

Icke, V., & Alcaino, G. 1988, A&A, 204, 115

Ikuta, C., & Arimoto, N. 2000, A&A, 358, 535

Jones, J. B., Drinkwater, M. J., Jurek, R., Phillipps, S., Gregg, M. D., Bekki, K., Couch, W. J., Karick, A., Parker, Q. A., & Smith, R. M. 2006, AJ, 131, 312

Jordán, A., Côté, P., Blakeslee, J. P., Ferrarese, L., McLaughlin, D. E., Mei, S., Peng, E. W., Tonry, J. L., Merritt, D., Milosavljević, M., Sarazin, C. L., Sivakoff, G. R., & West, M. J. 2005, ApJ, 634, 1002

Jordán, A., McLaughlin, D. E., Côté, P., Ferrarese, L., Peng, E. W., Blakeslee, J. P., Mei, S., Villegas, D., Merritt, D., Tonry, J. L., & West, M. J. 2006, ApJ, 651, L25

Jordi, K., Grebel, E. K., & Ammon, K. 2006, A&A, 460, 339

Kim, D.-W., Kim, E., Fabbiano, G., & Trinchieri, G. 2007, ArXiv e-prints, 0706:4254

Kundu, A. 2008, ArXiv e-prints, 0805:0376

Kundu, A., & Zepf, S. E. 2007, ApJ, 660, L109

Landolt, A. U. 1992, AJ, 104, 340

Lane, D. 1999, Hyperstat (Atomic Dog Publishing; 2nd edition (December 1999))

Larsen, S. S. 2004, A&A, 416, 537

Larsen, S. S., & Brodie, J. P. 2003, ApJ, 593, 340

Larsen, S. S., Brodie, J. P., Huchra, J. P., Forbes, D. A., & Grillmair, C. J. 2001, AJ, 121, 2974

Larson, R. B. 1981, MNRAS, 194, 809

Lee, M. G., Hwang, H. S., Kim, S. C., Park, H. S., Geisler, D., Sarajedini, A., & Harris, W. E. 2008a, ApJ, 674, 886

Lee, M. G., Park, H. S., Kim, E., Hwang, H. S., Kim, S. C., & Geisler, D. 2008b, ArXiv e-prints, 0802:1621

Levy, L., Rose, J. A., van Gorkom, J. H., & Chaboyer, B. 2007, AJ, 133, 1104

Lotz, J. M., Miller, B. W., & Ferguson, H. C. 2004, ApJ, 613, 262

Maraston, C. 2005, MNRAS, 362, 799

Mashchenko, S., Couchman, H. M. P., & Sills, A. 2006a, ApJ, 639, 633

Mashchenko, S., & Sills, A. 2004, ApJ, 605, L121

—. 2005a, ApJ, 619, 243

—. 2005b, ApJ, 619, 258

Mashchenko, S., Sills, A., & Couchman, H. M. 2006b, ApJ, 640, 252

Matthews, T. A., Morgan, W. W., & Schmidt, M. 1964, ApJ, 140, 35

Mieske, S., & Baumgardt, H. 2007, ArXiv e-prints, 0709:1328

Mieske, S., Hilker, M., & Infante, L. 2002, A&A, 383, 823

Mieske, S., Hilker, M., Infante, L., & Jordán, A. 2006a, AJ, 131, 2442

Mieske, S., Hilker, M., Jordán, A., Infante, L., & Kissler-Patig, M. 2007, A&A, 472, 111

Mieske, S., Infante, L., Benítez, N., Coe, D., Blakeslee, J. P., Zekser, K., Ford, H. C., Broadhurst, T. J., Illingworth, G. D., Hartig, G. F., Clampin, M., Ardila, D. R., Bartko, F., Bouwens, R. J., Brown, R. A., Burrows, C. J., Cheng, E. S., Cross, N. J. G., Feldman, P. D., Franx, M., Golimowski, D. A., Goto, T., Gronwall, C., Holden, B., Homeier, N., Kimble, R. A., Krist, J. E., Lesser, M. P., Martel, A. R., Menanteau, F., Meurer, G. R., Miley, G. K., Postman, M., Rosati, P., Sirianni, M., Sparks, W. B., Tran, H. D., Tsvetanov, Z. I., White, R. L., & Zheng, W. 2004, AJ, 128, 1529

Mieske, S., Jordán, A., Côté, P., Kissler-Patig, M., Peng, E. W., Ferrarese, L., Blakeslee, J. P., Mei, S., Merritt, D., Tonry, J. L., & West, M. J. 2006b, ApJ, 653, 193

Mieske, S., & Kroupa, P. 2007, ArXiv e-prints, 0712:1821

Moore, B., Diemand, J., Madau, P., Zemp, M., & Stadel, J. 2006, MNRAS, 368, 563

Norris, J. E., Freeman, K. C., Mayor, M., & Seitzer, P. 1997, ApJ, 487, L187+

Ortolani, S., Bica, E., & Barbuy, B. 1997, MNRAS, 284, 692

Ostrov, P., Geisler, D., & Forte, J. C. 1993, AJ, 105, 1762

Ostrov, P. G., Forte, J. C., & Geisler, D. 1998, AJ, 116, 2854

Parmentier, G., & Gilmore, G. 2001, A&A, 378, 97

Parmentier, G., Jehin, E., Magain, P., Neuforge, C., Noels, A., & Thoul, A. A. 1999, A&A, 352, 138

Parmentier, G., Jehin, E., Magain, P., Noels, A., & Thoul, A. A. 2000, A&A, 363, 526

Parratt, L. G. 1961, Probability and Experimental Errors in Science: An Elemental Survey (John Wiley and Sons, Inc., New York and London)

Peebles, P. J. E. 1969, ApJ, 155, 393

—. 1984, ApJ, 277, 470

Peng, E. W., Ford, H. C., & Freeman, K. C. 2004, ApJ, 602, 705

Peng, E. W., Jordán, A., Côté, P., Blakeslee, J. P., Ferrarese, L., Mei, S., West, M. J., Merritt, D., Milosavljević, M., & Tonry, J. L. 2006, ApJ, 639, 95

Peng, E. W., Jordan, A., Côté, P., Takamiya, M., West, M. J., Blakeslee, J. P., Chen, C.-W., Ferrarese, L., Mei, S., Tonry, J. L., & West, A. A. 2008, ArXiv e-prints, 803

Perrett, K. M., Bridges, T. J., Hanes, D. A., Irwin, M. J., Brodie, J. P., Carter, D., Huchra, J. P., & Watson, F. G. 2002, AJ, 123, 2490

Phillipps, S., Davies, J. I., Boyce, P. J., & Evans, R. 1993, Ap&SS, 207, 91

Phillipps, S., Drinkwater, M. J., Gregg, M. D., & Jones, J. B. 2001, ApJ, 560, 201

Puzia, T. H., Kissler-Patig, M., Thomas, D., Maraston, C., Saglia, R. P., Bender, R., Goudfrooij, P., & Hempel, M. 2005, A&A, 439, 997

Puzia, T. H., Kissler-Patig, M., Thomas, D., Maraston, C., Saglia, R. P., Bender, R., Richtler, T., Goudfrooij, P., & Hempel, M. 2004, A&A, 415, 123

Ramella, M., Geller, M. J., Pisani, A., & da Costa, L. N. 2002, AJ, 123, 2976

Rhode, K. L., & Zepf, S. E. 2001, AJ, 121, 210

Rhode, K. L., Zepf, S. E., & Santos, M. R. 2005, ApJ, 630, L21

Romanowsky, A. J. 2006, ArXiv Astrophysics e-prints, 0609:251

Sachs, R. K., & Wolfe, A. M. 1967, ApJ, 147, 73

Sadun, A. C., Aryan, N. S., & Ghosh, K. K. 2007, in American Astronomical Society Meeting Abstracts, Vol. 210, American Astronomical Society Meeting Abstracts, 02.19–+

Saitoh, T. R., Koda, J., Okamoto, T., Wada, K., & Habe, A. 2006, ApJ, 640, 22

Santos, M. R. 2003, in Extragalactic Globular Cluster Systems, ed. M. Kissler-Patig, 348–+

Scheepmaker, R. A., Haas, M. R., Gieles, M., Bastian, N., Larsen, S. S., & Lamers, H. J. G. L. M. 2007, A&A, 469, 925

Schuberth, Y., Richtler, T., Bassino, L., & Hilker, M. 2008, A&A, 477, L9

Searle, L., & Zinn, R. 1978, ApJ, 225, 357

Sikkema, G., Peletier, R. F., Carter, D., Valentijn, E. A., & Balcells, M. 2006, A&A, 458, 53

Smith, R. J., Lucey, J. R., Schlegel, D. J., Hudson, M. J., Baggley, G., & Davies, R. L. 2001, MNRAS, 327, 249

Solomon, P. M., Rivolo, A. R., Barrett, J., & Yahil, A. 1987, ApJ, 319, 730

Spitler, L. R., Larsen, S. S., Strader, J., Brodie, J. P., Forbes, D. A., & Beasley, M. A. 2006, AJ, 132, 1593

Stanford, S. A., Eisenhardt, P. R., & Dickinson, M. 1998, ApJ, 492, 461

Strader, J., Beasley, M. A., & Brodie, J. P. 2007, AJ, 133, 2015

Strader, J., Brodie, J. P., Cenarro, A. J., Beasley, M. A., & Forbes, D. A. 2005, AJ, 130, 1315

Strader, J., Brodie, J. P., & Forbes, D. A. 2004, AJ, 127, 3431

Strader, J., Brodie, J. P., Spitler, L., & Beasley, M. A. 2006, AJ, 132, 2333

Toomre, A., & Toomre, J. 1972, ApJ, 178, 623

Trager, S. C., Faber, S. M., Worthey, G., & González, J. J. 2000, AJ, 120, 165

Tsuchiya, T., Korchagin, V. I., & Dinescu, D. I. 2004, MNRAS, 350, 1141

Tsujimoto, T., & Shigeyama, T. 2003, ApJ, 590, 803

van den Bergh, S. 1975, ARA&A, 13, 217

Vettolani, G., Chincarini, G., Scaramella, R., & Zamorani, G. 1990, AJ, 99, 1709

Waters, C. Z., Zepf, S. E., Lauer, T. R., Baltz, E. A., & Silk, J. 2006, ApJ, 650, 885

Wegner, G., Colless, M., Saglia, R. P., McMahan, R. K., Davies, R. L., Burstein, D., & Baggley, G. 1999, MNRAS, 305, 259

Wehner, E., Harris, B., Whitmore, B., Rothberg, B., & Woodley, K. 2008a, ArXiv e-prints, 802

Wehner, E., & Harris, W. 2007, ArXiv e-prints, 0708:1514

Wehner, E. H., & Harris, W. E. 2006, ApJ, 644, L17

Wehner, E. M. H., Harris, W. E., Whitmore, B. C., Rothberg, B., & Woodley, K. A. 2008b, ApJ, 681, 1233

Willmer, C. N. A., Maia, M. A. G., Mendes, S. O., Alonso, M. V., Rios, L. A., Chaves, O. L., & de Mello, D. F. 1999, AJ, 118, 1131

Woodley, K. A., Harris, W. E., Beasley, M. A., Peng, E. W., Bridges, T. J., Forbes, D. A., & Harris, G. L. H. 2007, AJ, 134, 494

Worthey, G. 1994, ApJS, 95, 107

Yoon, S.-J., Yi, S. K., & Lee, Y.-W. 2006, Science, 311, 1129

Zepf, S. E. 2008, ArXiv e-prints, 0802:2113

Zepf, S. E., & Ashman, K. M. 1993, MNRAS, 264, 611

Zepf, S. E., Ashman, K. M., English, J., Freeman, K. C., & Sharples, R. M. 1999, AJ, 118, 752

Zinn, R. 1985, ApJ, 293, 424

Zinnecker, H., Keable, C. J., Dunlop, J. S., Cannon, R. D., & Griffiths, W. K. 1988, in IAU Symposium, Vol. 126, The Harlow-Shapley Symposium on Globular Cluster Systems in Galaxies, ed. J. E. Grindlay & A. G. D. Philip, 603–+